

## EXPANDING THE HORIZON OF MOLECULAR ELECTRONICS

#### VIA

#### NANOPARTICLE ASSEMBLIES

A thesis submitted in accordance with the requirement of the University of Basel for the degree of

#### DOCTOR OF PHILOSOPHY

in the Faculty of Philosophy and Natural Science by

#### Laetitia Bernard

from Montreux (Vaud), Switzerland



EXPANDING THE HORIZON OF MOLECULAR ELECTRONICS VIA NANOPARTICLE ASSEMBLIES Laetitia Bernard

Supervisor:

Prof. Dr. Christian Schönenberger

Referees:

Prof. Dr. Marcel Mayor Prof. Dr. Bernard Doudin

Dean:

Prof. Dr. Jacob Wirz

Basel, September 2006

If you look for Nature's secrets in only one direction, you are likely to miss the most important secrets, those you did not have enough imagination to predict.

FREEMAN DYSON

#### Table of Contents

1.	A C	$Clever\ Combination: Molecules\ \&\ Nanoparticles$	1
2.	A S	Short Guide to Organic Molecules & Nanoparticles .	5
	2.1	Insights on Molecular Physics	5
	2.2	Insights in Cluster Physics	18
	2.3	The Link between Electrical and Optical Material Properties	24
Pa	$nt\ I$	One Dimensional Systems	27
<i>3</i> .	Elec	ctrostatic Trapping of Nanoparticles	31
	3.1	Nanometre-spaced Electrodes : The Real Challenge ?	31
	3.2	Taking Advantage of Dielectrophoresis	32
	3.3	Concluding Remarks	37
4.	Elec	ctrical Transport in 1D Nanoparticle Assemblies	39
	4.1	On Course to Control the Final Device Resistance	39
	4.2	Low Temperature Characteristics of Nanoparticle Chains	47
	4.3	Concluding Remarks	50
Pa	art I	I Two Dimensional Systems	53
<b>5.</b>	Cor	$nbining \ Self-assembly \ \& \ Molecular \ Exchange $	57
	5.1	2D Self-Assembly of Metallic Nanoparticles	57
	5.2	Micro-Contact Printing	61
	5.3	The Ultimate Step : The Molecular Exchange	63
	5.4	Concluding Remarks	69
<b>6.</b>	Elec	ctrical Transport in 2D Nanoparticle Assemblies	71
	6.1	Electrical Transport through 2D Arrays	71

ii Table of Contents

	6.2 6.3 6.4	On understanding the Nanoparticle-Molecule Assembly . How about Another Molecular Wire?	75 78 82
7.	Ont	ical Characterisation of 2D Nanoparticle Assemblie	<b>s</b> 83
••	7.1	Surface Plasmon Resonance	83
	7.2	Molecular Detection by Infrared Spectroscopy	91
	7.3	X-ray Photoelectron Spectroscopy	97
	7.4	Concluding Remarks	100
8.	Cor	aclusions	103
	8.1	En Route to Molecule/Nanoparticle Hybrid-Systems	103
	8.2	The Vast Possibilities offered by Hybrid-Systems	104
$A_I$	open	dix	107
$oldsymbol{A}$ .	Tec	hnical Data on Investigated Molecules	109
	A.1	Alkanethiol Chains: $C_8$ , $C_{12}$ , $C_{16}$	109
	A.2	Oligo(phenylene ethynylene)	112
	A.3	Oligo(phenylene vinylene)	114
<b>B</b> .	<b>F</b> ab	$rication\ Parameters$	115
	B.1	Colloidal Solutions	115
	B.2	Electrodes' Preparation for 1-Dimensional Systems	119
	B.3	2-Dimensional Systems	121
<i>C</i> .	Med	asurement Setups	129
	C.1	· ·	129
	C.2	2-Dimensional Systems	132
D.	Cor	nplementary Experiments	135
	D.1		135
	D.2	Electromigration on 1D Nanoparticle Chain	136
	D.3	Effect of THF Bath on As-prepared Arrays	138
	D.4	Effect of Molecular exchange on the Nanoparticles	139
	D.5	Visible Absorption of Colloidal Solutions	139
	D.6	Estimation of the solvent/substrate influence on the SPR	140
	D.7	Visible Absorption on Small Selected Areas of Array	141
	D.8	IR Absorption of Alkane Chains	143
	D.9	Energy shift correction in XPS Analysis	144

Table of Contents	iii
-------------------	-----

<b>E</b> .	Cat	$alogue\ of\ Samples$											145
	E.1	1-Dimensional Systems											145
	E.2	2-Dimensional Systems									•		147
Bi	bliog	raphy									•		173

#### Table of Abbreviations

ac	Alternating Current
$C_{12}$	Dodecanethiol $(C_{12}H_{25}SH)$
$C_{16}$	Hexadecanethiol $(C_{16}H_{33}SH)$
$C_8$	Octanethiol $(C_8H_{17}SH)$
dc	Direct Current
DEP	Dielectrophoresis
DFT	Density Functional Theory
EBL	Electron-Beam Lithography
FFT	Fast Fourier Transform
FTIR	Fourier Transform Infrared
FWHM	Full Width at Half Maximum
HF	Hartree-Fock calculation
HOMO	Highest Occupied Molecular Orbital
ip	In Plane
ĪR	Infrared
I-V	Current-voltage characteristic
$\operatorname{LT}$	Low Temperature (4.2 K)
LUMO	Lowest Unoccupied Molecular Orbital
MCBJ	Mechanically Controllable Break Junction
MPC	Monolayered Protected Cluster
oop	Out Of Plane
OPE	Oligo(Phenylene Ethynylene)
OPV	Oligo(Phenylene Vinylene)
PDMS	Polydimethylsiloxane
PMMA	Poly(Methyl Methacrylate)
RMS	Root-Mean-Square
RT	Room Temperature (20-25°C)
SAM	Self Assembled Monolayer
SEM	Scanning Electron Microscopy
SPR	Surface Plasmon Resonance
STM	Scanning Tunnelling Microscopy
TEM	Transmission Electron Microscopy
THF	Tetrahydrofuran $(C_4H_8O)$
TLC	Thin Layer Chromatography
US	Ultrasonic
UV	Ultraviolet
UVL	Ultraviolet Lithography
XPS	X-ray Photoelectron Spectroscopy
ZBA	Zero Bias Anomaly
	·

#### A FEW COMMON SYMBOLS

$\beta$	tunnelling Decay Coefficient	$Å^{-1}$
c	speed of light	$3.10^{8}  \text{m/s}$
C	capacitance	F
d	inter-particle distance	nm
$\Delta$	tunnelling distance	m
$\delta$	deformation vibration resonance	$\mathrm{cm}^{-1}$
e	electronic charge	$-1.6 \cdot 10^{-19} \mathrm{C}$
E	energy	J, eV
$ec{E}$	electric field	V/m
$\epsilon$	energy level	J, eV
$\varepsilon$	permittivity	dimensionless
$E_a$	activation energy	$\mathrm{eV}$
$E_c$	charging energy	$\mathrm{eV}$
$E_F$	Fermi energy	$\mathrm{eV}$
f(E)	Fermi-Dirac function	dimensionless
f	frequency	$\mathrm{Hz}$
f	filling factor	dimensionless
$F_{DEP}$	dielectrophoresis force	N
$\phi$	tunnelling barrier energy	$\mathrm{eV}$
G	=1/R conductance	$\Omega^{-1}$
$G_0$	quantum of conductance	$\Omega^{-1}$
$\gamma$	damping constant	$s^{-1}$
Γ	energy broadening	$\mathrm{eV}$
h	Planck's constant	$6.63 \cdot 10^{-34}  \mathrm{Js}$
$\hbar$	$=h/2\pi$	
I	current	A
J	current density	$A/m^2$
k	$=1/\lambda$ wave number	$\mathrm{cm}^{-1}$
$k_B$	Boltzmann constant	$0.087\mathrm{meV/K}$
l	molecular length	nm
$\lambda$	wavelength	nm

viii Table of Contents

$\lambda_F$	electron mean free path	nm
m	free electron mass	$9.1 \cdot 10^{-31}  \mathrm{kg}$
$\nu$	stretching vibration resonance	$\mathrm{cm}^{-1}$
$\omega$	frequency	$s^{-1}$
$\omega_p$	plasmon frequency	$s^{-1}$
$ec{p}$	dipole moment	$C \cdot m$
p(t)	percolation probability	dimensionless
P	power	W
R	resistance	$\Omega$
$\sigma_{abs}$	absorption cross section	$\mathrm{m}^{-2}$
t	time	S
T	temperature	K
$\overline{T}$	transmission function	dimensionless
au	percolation time	min
V	bias voltage	V
Z	impedance	$\Omega$

# A CLEVER COMBINATION: ORGANIC MOLECULES & NANOPARTICLES

In view of current and future technological developments, Si-based microelectronics faces a constant need for miniaturisation. However, its evolution towards nanoelectronics presents severe physical and economic limitations. Several potential alternatives to supplement or to replace the current technology have been investigated, like silicon MOSFETs<sup>1,2,3</sup>, or techniques based on novel materials such as carbon nanotubes<sup>4,5</sup>. Another alternative is based on the use of single organic molecules, acting as electronic switches and storage elements<sup>6</sup>. Indeed, molecules exhibit inherent advantages over the current devices, making them appear as the ideal object for designing future high-density electronic devices. They are several orders of magnitude smaller than present feature sizes. They may be produced in large amounts absolutely identically and in a cheap way by chemical synthesis. Their physical properties are tunable by their structures. In addition, they have the potential to self-organise into regular 2D or 3D patterns. Therefore, complete systems for information processing may be built from basic functional units consisting of molecules acting as logic devices.

The use of molecules to perform electronic functions was first proposed in 1971 by  $Kuhn^7$ , followed by  $Aviram\ and\ Ratner^8$  in 1974, who, based on theoretical assumptions, envisioned the use of a donor-acceptor molecule to produce a molecular rectifier. At this time, any realisation of a molecular device was technologically absolutely unfeasible. Nowadays, the development of this visionary concept and its extension into the experimental domain has become the broad research area called  $Molecular\ Electronics^9$ , as demonstrated by the increasing number of citations of this early paper (Figure 1.1). The real beauty of this concept is the perspective that specific electronic functions of a device may be adjusted by the design of the chemical structure of the molecules  $^{10,11}$ . Moreover, additional tunability by other stimuli, like voltage, light or magnetic field

can be envisioned.

In this research area, two very different approaches are under extensive investigation: the bulk molecular systems and the single molecular systems. The first one is defined by characteristic dimensions which are much larger than the sizes of the molecules. Consequently, most of the molecules are in contact with other molecules, making them not individually addressable. The properties of this ensemble must be considered as a whole. In contrast, single molecular systems aim for individual contact to single molecules or small arrays of perfectly ordered molecules. This second approach strongly differs from the first one, as it tries to utilise the physical properties of single molecules for nanosized electronic devices.

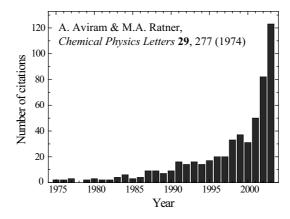


**Figure 1.1:** Time evolution of the number of citations of Aviram and Ratner's paper from 1974, precursor of the new field *Molecular Electronics*.

A basic requirement for *Molecular Electronics* is the connection of the molecules to the outside world. In the case of *bulk molecular systems*, this is achievable thanks to conventional UV or electron-beam lithography, which enables the fabrication of micrometre-scale contact patterns (down to 20 nm). For *single molecular systems*, an electrode pair with nanometre-sized spacing to contact a single molecule is needed. Although the development of such a device is challenging, the technological advance would provide the possibility to address one or few molecules. Several techniques were investigated, such as STM <sup>12,13,14</sup>, mechanically controllable break junctions (MCBJ) <sup>15,16</sup>, cross-bar arrays <sup>17,18,19</sup>, electromigration <sup>20,21</sup> or mercury droplet <sup>22</sup>. Quantum phenomena such as Coulomb blockade <sup>20</sup>, Kondo effect <sup>21</sup> and negative differential conductance <sup>10</sup> have already been observed. However, reproducibility and stability of such re-

sults still remain uncertain<sup>23</sup>. Indeed, the mobility of electrodes' atoms makes the metal-molecule junction unstable, strongly affecting the properties of the device, meaning that large ensembles of molecules would therefore be more suitable for technological applications. Devices developed using this second approach are already present on the market, such as for example liquid crystal displays or organic light emitting diodes.

Although tremendous progress was achieved on both approaches over the past few decades <sup>24,25,26</sup>, the understanding of current transport through molecules remains uncomplete. Both experimental and theoretical evidence show that the electronic properties of molecular junctions are not only dictated by the molecules contacted, but also depend on the anchoring groups and on the electrodes forming the junction <sup>23,27</sup>. Thus, along with the properties of the molecule itself, those of the block "contactmolecule-contact" also have to be considered. Introducing such building blocks into functional electronic circuits remains a demanding task, requiring innovative approaches in fabrication philosophy and circuit structure 17,28. Nanometre-size metallic nanoparticles as intermediate electrodes can be used as an elegant solution to build molecular junctions with well-defined geometry and electronic properties. Indeed, combining metallic nanoparticles with molecules to form such building blocks would overcome the size mismatch between nanometre-scale molecules and micrometre-scale electrodes  $^{29,30,31,32,33,34,35}$ 

We propose in this PhD Thesis a multidisciplinary study, interlinking chemistry (synthesis of nano-objects constituting building blocks), engineering (design of circuits based on the assembly of such building blocks) and physics (understanding of the ensemble properties). Concretely, two projects based on the assembly of nanoparticles were performed, on one hand, one-dimensional assembly, and on the other hand, two-dimensional assembly. The first one combines nanolithography and electrostatic trapping of colloids to achieve the fabrication of conducting nanoparticle chains. The second project consists of the self-assembly and the micro-contact printing of ligand-protected nanoparticles, followed by in-situ ligand exchange reactions. This fabrication method enables the preparation of stable two-dimensional networks of molecular junctions. Remarkably, this approach, combining the single molecular approach and the bulk molecular approach introduced above, takes the advantages of addressability of the first one and stability of the second one.

#### OUTLINE

This dissertation is organised as follows: a concise introduction to molecular electronics and to nanoparticle physics is given in Chapter 2. The 1D approach is presented in the Part 1. Whereas the concept of fabrication, based on the ac trapping technique, is described in Chapter 3, the electrical characterisation and the technical limitations are discussed in Chapter 4. The Part 2 presents the 2D approach. The fabrication philosophythe self-assembly, as well as the circuit design - the micro-contact printing followed by shadow evaporation, are introduced in Chapter 5. Electrical and optical characterisations follow in Chapter 6 and Chapter 7, respectively. Discussion on the advantages and limitations of such devices end the chapter. The dissertation is closed by Chapter 8 with general remarks and prospective ideas for this project. For detailed pieces of information, technical data on the different fabrications and measurements and complementary experiments, we report the reader to the Appendices.

# 2

### A SHORT GUIDE TO ORGANIC MOLECULES & NANOPARTICLES

#### 2.1 Insights on Molecular Physics

#### 2.1.1 What is the Resistance of a Molecule?

The first question one comes to when considering the field of *Molecular Electronics*, is: "What is the resistance of a molecule?". The term of resistance was used to define, in bulk material, a macroscopic property related to a scattering process of the electrons flowing through the material, namely a kind of friction effect. Following the top-down approach, scientific interest has moved to smaller and smaller objects, nonetheless keeping the same concepts established for the bulk material. At a certain point, this gave rise to an interesting phenomenon, called ballistic transport, where electron transport was free of scattering. Thus, this appears confusing, since the so-called resistance is not clearly defined in such a situation. Once the existence of a finite number of discreet channels of conduction in small objects demonstrated  $^{36,37}$ , Landauer  $^{38}$  has been the one to find a way out of this. He quantum mechanically showed that the conductance could be described in term of the sum of the transmission functions  $T_i$  for all the channels i:

$$G = \frac{2e^2}{h} \sum_{i=1}^{N} \overline{T}_i \tag{2.1}$$

with  $G_0 = \frac{2e^2}{h}$  the quantum conductance, namely the highest possible conductance for one electron transport channel\*.

This formalism is nowadays widely used in the field of *Molecular Electronics*, as gives evidence the increasing number of review articles reporting it  $^{39,40}$ . In the case of a molecule coupled to metal electrodes, two

<sup>\*</sup> Note that the factor 2 in this expression accounts for the two spins.

aspects appear to be crucial for the transmission. The first aspect concerns the molecule itself. It was suggested in the introduction that one can choose the electrical properties of a molecular junction by synthesising a specific molecule, having the desired properties. There is a wide range of possibilities for molecules: they can be more insulating, more conducting, or have some functionality. The second aspect is the nature of the contact between the molecule and the electrodes. The metal-molecule-metal coupling is at least of equal importance as the molecular structure itself. The control of this coupling is a major issue. Indeed, it has to be strong enough to allow the current flow, but weak enough the preserve the intrinsic electronic characteristics of the molecule. These two aspects, the processes involved and the limit of their understanding are briefly described in this section.

#### 2.1.2 The Organic Molecule

The simplest molecules from the electronic point of view are molecular wires: a molecular scale extension of macroscopic metal wire. In any organic molecule, however, electron transport is expected to take place through the frontier orbitals of the molecule, being the closest to the Fermi levels of the electrodes. The molecule size, as well as the presence of  $\pi$ -systems, decrease the energy between the frontier orbitals, hence making the molecule a better conductor. Therefore, non-conjugated molecules (neither  $\pi$ -system nor  $\sigma$ -system) like alkanes are good insulators and conjugated molecules containing for example large delocalised  $\pi$ -systems like polyenes allow the transport of electric charges (see Figure 2.1).

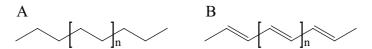


**Figure 2.1:** Schematics of two molecular wires. A. Alkane (not conjugated molecule); B. Polyene (conjugated molecule). Although their structure is very similar, the first one is insulating, while the transport of electrons is possible through the second one.

Both the insulating and conducting properties are of importance, and are used in different applications. However, those are not the only properties which can be optimised. The rigidity of the structure is of similar importance, for example to prevent short circuiting of separated units through space. Rigid non-conjugated molecules are rather seldom.

Alkanes, known for their insulating properties, lack the required rigidity. Cyclic  $\pi$ -systems meet the rigidity conditions but are good conductors. However, the delocalisation of the  $\pi$ -systems depends strongly on the torsion angles between the subunits (aromatic rings for example) <sup>41</sup>. Two neighbouring subunits with perpendicular  $\pi$ -systems reduce their electronic communication (see Figure 2.2) by reducing the overlap of the electronic orbitals. Hence, the conduction of electrons through such a molecule is reduced and the molecule appears less conductive.

**Figure 2.2:** Aromatic rings perpendicular to each other decrease significantly the overlap of their  $\pi$ -systems, hence, the overall conductance of the molecular unit.

Furthermore, the electron conduction through an aromatic ring also depends on the relative position of the linkage (see Figure 2.3)<sup>42</sup>. While ortho- and para- connections are conjugated linkers, hence allowing a good conduction, the meta-position is not, as two consecutive single bonds disable the overlapping of the  $\pi$ -orbitals. Therefore, the conduction is in this configuration decreased.

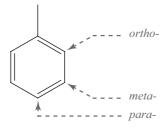


**Figure 2.3:** On an aromatic ring, three relative positions of the linkage are possible. They are known as *ortho-*, *meta-* and *para-* positions.

#### 2.1.3 Molecular Electronics: The Contacts

To study and understand the electronic properties of a molecule, one first has to be able to electrically address it, hence to contact it (Figure 2.4). This is where the second aspect, the nature of the contacts, plays a crucial role. The usual way to electrically contact a molecule or an ensemble of molecules is to bind it to metallic electrodes. To ensure a mechanically

strong bond between the electrodes and the molecule, binding groups acting as "alligator-clips" (generally sulfur atoms) are attached at both ends of the molecule, providing a covalent bond. However, let us note that although they are good mechanical bonds, they are not electrically transparent  $^{43,44}$ . The electrodes constitute the two leads, with Fermi energy  $E_F$ , to and from which the electrons may flow.

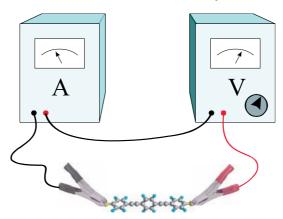


**Figure 2.4:** How to contact and measure the electronic properties of an organic molecule?

To describe the electron transfer mechanism through the molecule, one has to consider the energy levels diagram of the metal-molecule-metal system, as presented in Figure 2.5A. Whereas the metal leads present a continuum of energy levels, the molecule has discreet levels, also called molecular orbitals. In particular, one can distinguish a set of filled levels (under  $E_F$ ) and a set of empty levels (above  $E_F$ ). The electrons can flow if one level is nearby the Fermi level. This is in general not the case, since the lowest unoccupied molecular orbital (LUMO) is separated from the highest occupied molecular orbital (HOMO) by a gap of typically a few eV. A possibility to get electron transfer is to change the energy levels of the leads with respect to the molecular levels, by applying a bias voltage V in between them, as shown in Figure 2.5B. Hence, by moving apart from the Fermi level, the leads' levels open an energy window of  $e \cdot V$ , where the transfer of electrons is possible. Whereas the left contact tends to fill up all available states below  $E_F + e^{V/2}$ , the right contact keeps emptying all states above  $E_F - eV/2$ , hence yielding in an electron flow through the molecule, from left to right. As long as levels are in the energy window, they and only them, allow the transfer of electrons. This flow might be more or less large, depending on the quality of the contacts.

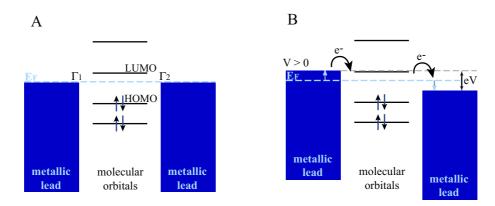


Figure 2.5: Energy diagram of a molecule in between two metallic leads with Fermi energy  $E_F$ . A. No voltage is applied at the edges of the junction. No electron can flow as no level lies nearby the Fermi energy. B. By applying a voltage V, the leads' energies shift with respect to the Fermi energy while the molecule orbitals remain at the same position. An energy window of width eV opens. As soon as the first molecular orbital is included in this window, electrons are transferred from the left lead to the molecule and from the molecule to the right lead (electrons flow).

To quantitatively characterise the current one has to consider the typical time needed for the electrons to flow from one lead to the molecule, and from the molecule to the second lead. This would be the objective quantification of the quality of the contacts. Hence, one may introduce the escape rates, or tunnelling rates,  $\Gamma_1/\hbar$  and  $\Gamma_2/\hbar$ , corresponding to those characteristic times and representative of the coupling between the leads and the molecule, for the left and the right contacts respectively. Physically,  $\Gamma_i/\hbar$  is the number of times per second that an electron succeeds in flowing through the barrier i = 1, 2. The tunnelling rates induce also a broadening of the molecular orbitals. Indeed, in the case of strong coupling, the molecular orbitals and the leads' electronic states do overlap. This yields a hybridisation of the electronic states, and thus a common delocalised electronic wave function extending over the whole junction. This provokes a broadening of the energy levels of  $\Gamma = \Gamma_1 + \Gamma_2$ , as shown in Figure 2.6, as well as a shift of the molecular orbitals. Hence, one has to consider rather the molecular density of states:

$$D_{\epsilon}(E) = \frac{1}{2\pi} \frac{\Gamma}{(E - \epsilon)^2 + (\Gamma/2)^2}$$
 (2.2)

instead of the discreet molecular levels, with  $\epsilon$  the levels' energy. The expression of the current flowing across the junction is then the integral over the whole energy range, and is expressed in the case of symmetric barriers by :

$$I(V) = \frac{e}{\hbar} \cdot \int_{-\infty}^{\infty} D_{\epsilon}(E) \cdot \frac{\Gamma_1 \Gamma_2}{\Gamma} \cdot \left\{ f(E + \frac{eV}{2}) - f(E - \frac{eV}{2}) \right\} dE \qquad (2.3)$$

with f(E) the Fermi-Dirac function. Note that because of the broadening, the molecule might exhibit a higher conductance than what one could expect by considering non-degenerated levels, as one can see in Equation (2.3). Identifying  $D_{\epsilon}(E) \cdot \frac{\Gamma_1 \Gamma_2}{\Gamma} = \frac{1}{\pi} \overline{T}(E)$ , (2.3) is equivalent to the energy dependent Landauer formula, which reads:

$$I(V) = \frac{2e}{h} \cdot \int_{-\infty}^{\infty} \overline{T}(E) \cdot \left\{ f(E + \frac{eV}{2}) - f(E - \frac{eV}{2}) \right\} dE$$
 (2.4)

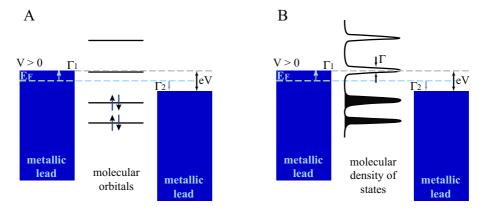


Figure 2.6: Transport through a metal-molecule-metal junction. A. The molecule is decoupled from the leads and the levels are sharp. B. The coupling to the leads is good, hence, a broadening of the levels occurs, as well as a shift of the level, with respect to  $E_F$ . The coupling to the leads is represented by  $\Gamma_1$  and  $\Gamma_2$  for the left and right leads respectively.

Let us remark that the current is limited to a maximum value. Indeed, this maximum is reached when the transmission function is maximum  $\overline{T}(E) = 1$ . Hence, the integral (2.4) resumes, at T = 0 K, to:

$$I_{max}(V) = \frac{2e}{h} \cdot \int_{-\frac{1}{2}eV}^{\frac{1}{2}eV} 1dE = \frac{2e^2}{h}V$$
 (2.5)

defining thus the quantum of conductance presented in Equation (2.1) for one channel, possibly expressed in term of resistance:

$$R_0 = \frac{1}{G_0} = \frac{h}{2e^2} \approx 12.9 \, k\Omega \tag{2.6}$$

This resistance is a characteristic constant in the field of *Molecular Electronics*\*.

Finally, note that in the case of a non-conducting molecule, i.e. whose HOMO-LUMO gap is so large that no states can be found in the energy window, one expect to have either no conduction at all, or tunnelling, directly from one lead to the other. The tunnelling current decays exponentially with the distance d, and is described by the relation (2.7) at low-bias,  $\Phi$  being the energy barrier and m the electron mass.

$$I \propto \frac{1}{d} e^{-\frac{2}{\hbar}\sqrt{2m\Phi} \cdot d} \tag{2.7}$$

For convenience, one may introduce the tunnelling decay coefficient  $\beta = \frac{2}{\hbar}\sqrt{2m\Phi}$ . As a matter of fact, it was shown that even though a molecule is in principle non-conducting, the tunnelling across it is different than the tunnelling through vacuum. Hence, the molecule, just by the presence of its electronic density, influences the transfer of electrons. This contribution appears in the current expression (2.7) through the energy barrier  $\Phi$ , depending on the molecule and its levels' position with respect to the leads  $E_F^{40}$ . This effect is known in the chemistry and physics communities as the mediated tunnelling, or super-exchange.

Commonly and in the case of this thesis, gold is chosen for the leads, because of its noble metal properties (stable, non-reactive). However, other noble metals can be used, like palladium or platinum <sup>45,46</sup>, and might present some advantages, such as lower mobility or enhanced wetting properties. Sulfur is widely used as binding chemical group, since it provides a strong covalent bond with gold, ensuring the mechanical stability of the contact, and a fast charge transfer <sup>47</sup>. However, different binding groups are currently under investigation, like the dithiocarba-

<sup>\*</sup> Note that the resistance of one single atom-atom junction is typically of order  $R_0$ .

mate  $(-NCS_2)^{44}$ , the cyanide  $(-CN)^{48,49}$ , or the selenium  $(-Se)^{43}$ , which was recently shown to allow a better coupling of the molecule with the electrodes. Some theoretical analysis of metal-molecule contacts make comparisons of different metals and different binding groups  $^{50,51}$ . This type of analysis discuss in particular the advantages and disadvantages of different "metal/binding group" pairs.

As a conclusion, both the electrical properties of the molecule and the nature of the molecular contacts are of major importance in the transport properties of the whole junction  $^{52}$ . In particular, the resistance might vary strongly, if the molecule-metal bond is arranged differently  $^{53}$ . Consequently, the resistance, defined as the bias voltage V divided by the current I, concerns the full metal-molecule-metal junction, rather than the molecule alone. Further information on the electron transport in molecular wires can be found in various review papers  $^{27,39,54}$ .

#### 2.1.4 Molecular Optics

The interaction of light with organic molecules leads to electronic, vibrational and/or rotational excitations, depending on the incoming photons' energy. Under ultraviolet or even visible light, the energy transferred to the molecules is sufficient to excite their electrons. At lower energies however, typically for light in the infrared region, this is no more the case. Instead, the interatomic bonds can be excited, exhibiting stretching and deformation vibrations. Rotations of the molecules can be observed at even lower energies. Those mechanisms are briefly presented in this section, as well as how their study enables to access properties of the considered molecules.

#### UV-Visible Light Interaction with Molecules

Ultraviolet (200-400 nm) as well as visible light (400-800 nm) is able, via its absorption, to promote the excitation of molecular electrons between the energy levels corresponding to the molecular orbitals of the systems. In particular, transitions involving  $\pi$ -orbitals,  $\sigma$ -orbitals and lone pairs (n  $\equiv$  non-bonding) are of great importance\*. The lowest possible energy transition is the one between the HOMO and the LUMO in the ground state. The more conjugated the system, the smaller the HOMO-LUMO gap, and therefore, the larger the wavelength. Hence, the study of the

<sup>\*</sup> Note that other transitions are possible, like transitions involving charge-transfer electrons, or involving d and f electrons.

resulting absorption spectra, via UV-Visible spectroscopy, can lead typically to the identification of conjugated systems and the determination of their HOMO-LUMO gap.

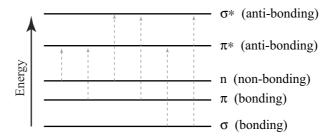


Figure 2.7: Diagram of the molecular orbitals: electronic excitations that can occur in organic molecules in interaction with UV-visible light.

Figure 2.7 presents a diagram of the various kinds of electronic excitation that may occur in organic molecules. Out of the six transitions outlined, only the two lowest energy ones (the n- $\pi$  and  $\pi$ - $\pi$  transitions) can be achieved by the energies available in the 200 to 800 nm spectrum. These transitions need an unsaturated group in the molecule to provide the  $\pi$ -electrons. The  $\sigma$ - $\sigma$  transitions show an absorbance maximum at 125 nm, whereas the n- $\sigma$  transitions can be initiated in the range 150 – 250 nm, but the number of organic functional groups exhibiting the latter transitions is small.

Moreover, absorption of ultraviolet and visible light in organic molecules is restricted to certain functional groups, called *chromophores*, that contain valence electrons of low excitation energy. The spectrum of a molecule containing these chromophores is complex. However, because of the superposition of rotational and vibrational transitions on the electronic transitions (see next section), a combination of overlapping lines makes the absorption appear as a continuous absorption band.

#### Infrared Light Interaction with Molecules

Infrared (IR) electromagnetic waves, whose frequencies are situated between  $10^{10}$  Hz and  $10^{14}$  Hz\*, typically are in the range of energies for exciting the atomic bonds' vibrations of molecules, as well as their rotation. Indeed, the interaction IR light-molecule may induce vibrations and rotations at specific energy levels. The set of the vibrational and

<sup>\*</sup> This corresponds to wavelengths from  $1 \,\mu\mathrm{m}$  to  $1 \,\mathrm{cm}$ .

rotational levels that a molecule can have is very specific firstly to its composition (which atoms do compose the molecule) and secondly to its configuration (how these atoms are linked together). Hence, the position and intensity of absorption bands in the IR of a substance are extremely specific to that substance and constitute its fingerprint. Hence, IR spectroscopy is a powerful tool for molecular identification and can be used for the detection of specific molecules within a heterogeneous substance by spectral comparison <sup>55,56,57</sup>. Another way to identify a specific molecule within a substance is to simulate the position and intensity of the absorption peaks, according to the molecular composition and shape. Electronic structure methods, like ab initio Hartree-Fock method (HF) or density functional theory (DFT), are increasingly used for modelling molecular properties that includes equilibrium structures, vibrational frequencies and intensities. Those methods give thus a good estimation of the infrared absorption of small molecules.

Here, to get a feeling on the IR light-molecule interaction, we present a simple quantum mechanics derivation for a diatomic molecule. It gives already a good indication on the possible levels and transitions for vibrations and rotations of the molecule.

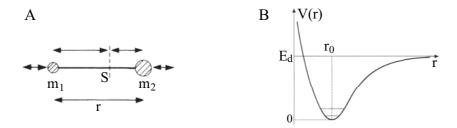


**Figure 2.8:** A. Schematic of a diatomic molecule experiencing stretching vibrations. B. Interaction potential between two bonded atoms.

The potential expressing the interaction between two atoms is presented in Figure 2.8B, with its minimum (equilibrium between attraction and repulsion forces) centred at  $r_0$ . For describing molecular vibrations of a diatomic molecule, one starts out from the simple harmonic oscillator model. The atoms are assumed to be points of mass  $m_1$  and  $m_2$ , kept together by a weightless spring (see Figure 2.8A) of initial length  $r_0$  (without vibration). Let's point out that the harmonic oscillator model supposes the potential to be parabolic and so, is valid only for small oscillations around  $r_0$ . Hence, considering the potential  $V(r) = \frac{1}{2}m\omega(r-r_e)^2$ ,

one may solve the Schrödinger equation with the hamiltonian being the sum of kinetic and potential energy:

$$\[ -\frac{\hbar^2}{2m} \frac{d^2}{dr^2} + V(r) \] \psi_v(r) = E_v \psi(r) \tag{2.8}$$

 $m = \frac{m_1 m_2}{m_1 + m_2}$  is the reduced mass of the system,  $\omega$  the pulsation of the incoming wave,  $\psi_v(r)$  are the eigen states of the system, corresponding the the eigen values  $E_v$ , the energy levels of vibrations. By resolving this equation, one finds the expression for these energy levels of vibrations:

$$E_v = \left(v + \frac{1}{2}\right)\hbar\omega\tag{2.9}$$

with  $v=0,1,2,\ldots$ , the vibrational quantum number. This results shows first that the ground state, given by v=0, is not zero. Second, one sees that the levels for vibration are quantised. Hence, only specific energies of the incoming wave, corresponding to the energy difference between two states  $|\Psi_v\rangle$  and  $|\Psi_{v'}\rangle$ , can make the molecule vibrate. Furthermore, only certain transitions are allowed, according to the selection rule:  $\Delta v = v - v' = \pm 1^{58}$ . As the IR spectrum of a substance is usually plotted as a function of the wave number  $k=1/\lambda$ , it is more convenient to express the vibrational levels in unit of wave vector instead of energy, by introducing a function G(v) given in (2.10).

$$G(v) = \frac{E_v}{hc} = k\left(v + \frac{1}{2}\right) \tag{2.10}$$

Then, because of the selection rule, the only possible transitions are given by  $G(v) - G(v \pm 1) = k$ , as represented in Figure 2.9A.

However, for larger oscillations, as the potential is not parabolic (see Figure 2.8B), one has to consider rather the anharmonic oscillator model to estimate the vibrational levels of the diatomic molecule. It is equivalent to consider the harmonic oscillator added by a third-order perturbation<sup>58</sup>. This leads to two differences: first the energy levels  $E_v$  get a third-order correction (subtracted) which increases with increase v, leading to lesser separation between the levels for larger v. More importantly, the selection rule gets weaker and becomes  $\Delta v = \pm 1, 2, 3, \ldots$ , due to eigen states mixing. It means that transitions between states that are not consecutive may also happen (see Figure 2.9B). However, those transitions, called *overtones*, have a much smaller probability to happen than the fundamental vibration, given by  $\Delta v = \pm 1$ .

For describing molecular rotations of a diatomic molecule, one uses

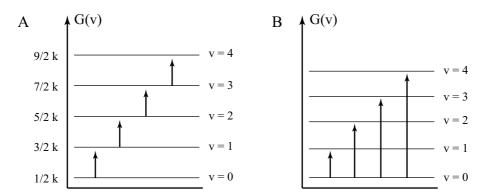


**Figure 2.9:** A. Vibrational energy levels of the diatomic molecule with a harmonic oscillator model. B. Correction of the vibrational energy levels of the diatomic molecule with an anharmonic oscillator model.

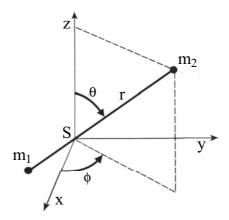


Figure 2.10: Schematic of a diatomic molecule experiencing rotations.

the rigid rotator model. One considers the moment of inertia  $I=mr_e^2$  of the molecule, hypothesising that the two atoms' distance is fixed (see Figure 2.10). The hamiltonian,  $H=-\frac{\hbar^2}{2I}[\frac{\partial^2}{\partial\theta^2}+\frac{1}{tg\theta}\frac{\partial}{\partial\theta}+\frac{1}{sin^2\theta}\frac{\partial^2}{\partial\phi^2}]$ , in this case contains only kinetic energy and the Schrödinger equation has to be solved in spherical coordinates. The rotational energy levels found by solving this equation are :

$$E_j = \frac{j(j+1)\hbar^2}{2I} \tag{2.11}$$

with j=0,1,2,..., the rotational quantum number. This shows that also the rotational levels are quantised. However, the ground state

for rotation, given by j=0, is zero. The rotation also has to obey a selection rule:  $\Delta j=\pm 1^{58}$ . In a similar way as for vibration levels, one can express the rotational levels in unit of wave vector, by introducing a function F(v) given by:

$$F(j) = \frac{E_j}{hc} = Bj(j+1)$$
 (2.12)

with  $B = \frac{\hbar}{4\pi cI}$  defined as the *rotational constant*. Then, because of the selection rule, the only possible transitions are given by  $F(j) - F(j \pm 1) = 2B(j+1)$ , as represented in Figure 2.11A. For rotation thus, the levels get a larger separation for larger j.

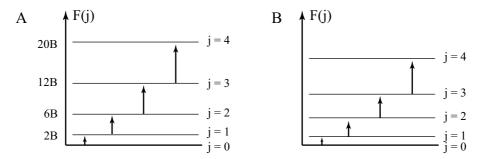


**Figure 2.11:** A. Rotational energy levels of the diatomic molecule with the kinetic moment approach. B. Correction of the rotational energy levels due to the centrifugal force.

In reality, the distance between the two atoms is not constant and increases with increasing rotation energy due to centrifugal force. This leads to a larger I and thus, a reduced  $\Delta F$ . That is the reason why the level spacing does not increase as much as predicted by the rigid rotator model (see Figure 2.11B).

Finally, as the molecule vibrates and rotates simultaneously, the global band diagram (see Figure 2.12) combines both and the transitions from one state  $|\Psi_{v,j}\rangle$  to another  $|\Psi_{v',j'}\rangle$  are given by :

$$\begin{cases} k = \Delta G + \Delta F = G(v') - G(v) + B_{v'}j'(j'+1) - B_vj(j+1) \\ \Delta v = \pm 1, 2, 3, \dots \\ \Delta j = \pm 1 \end{cases}$$
 (2.13)

Remark that because of the coupling rotation-vibration, B in (2.13) depends on  $v: B_v = B - a(v + 1/2)$ , with a a constant. This expres-

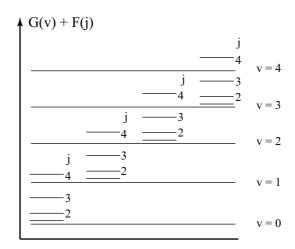


**Figure 2.12:** Superposition of the vibrational (v) and rotational (j) energy levels of a diatomic molecule.

sion plus the two selection rules give the positions (wave number) of the allowed transitions, thus the positions of the absorption peaks in the IR spectra.

#### 2.2 Insights in Cluster Physics

Clusters constitute an intermediate state of matter, composed by a few atoms up to millions of atoms, between the single atom on the one hand and the bulk matter on the other. Their diameter ranges typically from 1 nm to several tens of nanometres, and their packing can be different from the bulk matter. In this intermediate case, the range of interactions is in general larger than the size of the particles. Furthermore, they are characterised by a large surface/volume ratio. Those effects strongly influence their atomic and electronic structure, and this influence is often dependent on the size of the cluster. Two different kinds of cluster-size effects can be distinguished: the *intrinsic effects*, due to specific changes in volume and surface material, and the *extrinsic effects*, which are collective size-dependent response to external environment, such as the collective electronic and lattice excitations. For large clusters (typically  $\emptyset \geq 10 \, nm$ ), the extrinsic effects play a dominant role, whereas for small clusters, the intrinsic effects become important.

Hence, the electrical and optical properties of clusters may strongly differ from the bulk properties but also from the single atom properties. Their description cannot be made by pure solid state physics nor pure quantum physics. Specific theories and models have to be considered for such systems, taking into account the classical thermodynamics and electrodynamics and including the size and environmental effects.

As the clusters used in the present experiments are considered as "large" clusters ( $\geq 10\,nm$ ), and to keep this chapter concise, we focus on this particular case throughout this basic introduction. It is important however to keep in mind that electrical and optical properties change drastically when considering so called "small" clusters. For similar reasons, we restrict our description to metallic spherical clusters.

#### 2.2.1 Cluster Electronics

Like for molecules, the electronic properties of small clusters (typically  $\leq 3\,\mathrm{nm}$ ) are described by discreet quantum energy levels (Figure 2.13C). This type of structures is described by the *jellium model*, where the ion cores are seen as a static positively charged skeleton and the conduction electrons as a homogeneous negative cloud. For larger cluster sizes, these bands tend to group in bunches of energy levels. The electronic properties are then given by a new type of band structure, each band consisting of a bunch of single levels (see Figure 2.13B). For even larger clusters, like those considered in this thesis, the energy spectrum becomes similar to those of bulk gold\* (Figure 2.13A).

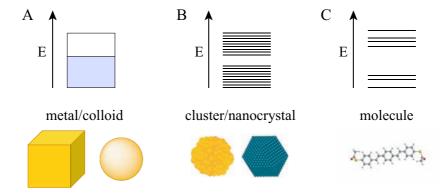


**Figure 2.13:** Energy diagrams for bulk, intermediate and molecular systems: continuous, bunches of single levels and discreet levels, respectively.

<sup>\*</sup> A rough estimation gives in our case, namely with clusters of  $\emptyset$  10 - 20 nm, levels spacing of  $\sim 10^{-4}\,\mathrm{eV}$ .

However, such large clusters cannot be fully considered as bulk material  $^{59}$ . Besides the question of the energy spectrum, there are also some important size effects. For example, when the cluster size is of the order of the electron mean free path (typically  $\lambda_{Au} \approx 3 \,\mathrm{nm}$  at room temperature  $^{60}$ ), scattering of electrons on the boundaries become an important contribution. Another effect is the inefficiency of electron screening, due to a low number of atoms, as compared to bulk material. This results in an increase of the ionisation potential, which is dependent on the size. Number of reviews report on the relationship between particle size and electronic behaviours  $^{61}$ .

#### 2.2.2 Cluster Optics

The interaction of photons with clusters leads to electronic and/or vibrational excitations. The dominant optical features of metal clusters are those associated with the largest oscillator strengths, issuing from the collective electron excitations in the clusters. Those collective oscillations, also called *surface plasmons*, are at the origin of the dipole modes in the clusters, related to the dipole resonances in atoms. Although all electrons are oscillating with respect to the positive ion background, the main effect is the oscillating surface polarisation of the clusters. The optical features resulting from this effect consist of an absorption band centred around the surface plasmon resonance  $\omega_{sp}$ , positioned in the visible range wavelengths. The resonant width and peak intensity depend, on the electron relaxation rates, modified from bulk values by scattering off the cluster surface, on the internal structure (grain boundaries in polycrystalline particles), and on interface effects. The surface plasmon resonance frequency  $\omega_{sp}$  is closely related to the bulk plasma resonance frequency  $\omega_p = (\frac{ne^2}{\varepsilon_0 m_e})^{-1/2}$ , and the exact expression depends on the sample geometry. For spherical clusters in vacuum<sup>62</sup>,  $\omega_{sp} = \omega_p/\sqrt{3}$ . However in general, this expression and more globally the interaction of light with clusters is of high complexity, since it strongly depends on the material, the surrounding medium, the size and shape of the clusters. The first electrodynamics general solution was calculated by Gustav Mie in 1908<sup>63</sup>. This scattering theory (also called *Mie Theory*) is still extensively used nowadays to model cluster-light interaction (c.f. Section 7.1).

#### Mie Theory

The solution proposed by Mie divides the problem into two parts : an electromagnetic part, treating the general interaction between light and a metallic cluster, and a material part, circumvented by introducing a phenomenological dielectric function  $\varepsilon(\omega,r)$  describing the "nature" of the cluster.

For the derivation of the general solution of the light diffraction of a single metallic sphere, Mie applied Maxwell's equations with appropriate boundary conditions in spherical coordinates using multipole expansions of the incoming electric and magnetic fields. The solution was based upon the determination of scalar electromagnetic potentials  $\Pi$ , solving the wave equation  $\Delta\Pi + |\vec{k}|^2\Pi = 0$ , and whose solution in spherical coordinates can be expressed as  $\Pi(r,\theta,\phi) = R(r)\Theta(\theta)\Phi(\phi)$ . These three functions were found to be a Bessel function, a Legendre polynomial function and a sinusoidal function for the r,  $\theta$ , and  $\phi$  dependencies respectively. These potentials constitute a basis of vector harmonics, allowing the expansion of an electromagnetic plane wave in such a spherical basis  $\vec{E} = \sum_{m=0}^{\infty} \sum_{n=m}^{\infty} A_{mn} \Pi_{mn}$ . Here, n represents the order of the expansion

sion (pole) and m is the relative refractive index given by  $m = \frac{N_c}{N_m}$ ,  $N_c$  and  $N_m$  being the index of refraction of the cluster and the medium respectively. The so called scattering coefficients  $A_{mn}$  are determined by applying the boundary conditions, solved by considering the internal and scattered fields. The full derivation can be found elsewhere <sup>64</sup>. The two sets of scattering coefficients, corresponding to the electric modes  $(a_n)$  and the magnetic modes  $(b_n)$ , are given by the Bessel functions of first and second kind  $j_n$  and  $h_n = j_n \pm iy_n$  constituting the R(r) function:

$$\begin{cases}
 a_n = \frac{m^2 j_n(mx)[xj_n(x)]' - j_n(x)[mxj_n(mx)]'}{m^2 j_n(mx)[xh_n^{(1)}(x)]' - h_n^{(1)}(x)[mxj_n(mx)]'} \\
 b_n = \frac{j_n(mx)[xj_n(x)]' - j_n(x)[mxj_n(mx)]'}{j_n(mx)[xh_n^{(1)}(x)]' - h_n^{(1)}(x)[mxj_n(mx)]'}
\end{cases} (2.14)$$

 $x=N_m \frac{2\pi r}{\lambda}$ , known as the size parameter is of crucial importance since it distinguishes the cluster  $(x\ll 1)$  from the bulk material  $(x\gg 1)$ . Thanks to the coefficients  $a_n$  and  $b_n$ , it is possible to determine all the measurable quantities associated with scattering and absorption, such as cross sections. Those cross sections for extinction  $\sigma_{ext}$  and scattering  $\sigma_{scat}$  (see Equation (2.15)) are derived by calculating the net rate at which electromagnetic energy crosses the surface of an imaginary sphere centred on the cluster. The absorption cross section  $\sigma_{abs}$  can be deduced.

$$\begin{cases}
\sigma_{ext} = \frac{2\pi}{k^2} \sum_{n=1}^{\infty} (2n+1) \Re\{a_n + b_n\} \\
\sigma_{sca} = \frac{2\pi}{k^2} \sum_{n=1}^{\infty} (2n+1) (|a_n|^2 + |b_n|^2) \\
\sigma_{abs} = \sigma_{ext} - \sigma_{sca}
\end{cases}$$
(2.15)

In the limit where  $x \leq 0.01$ , meaning that the cluster size is much smaller than the interacting wavelength, the fields inside the cluster are seen as constant. One can make in such a case the *quasi-static approximation* consisting of taking only the dipolar electric mode  $(a_1)$  into account. The Mie expression of the extinction cross section is simplified considerably, as shown in Equation  $(2.16)^*$ .

$$\sigma_{ext}(\omega) = 12\pi \frac{\omega}{c} \varepsilon_m^{3/2} r^3 \frac{\varepsilon_2(\omega)}{[\varepsilon_1(\omega) + 2\varepsilon_m]^2 + \varepsilon_2(\omega)^2}$$
 (2.16)

where  $\varepsilon_m$  and  $\varepsilon = \varepsilon_1 + i\varepsilon_2$  are the dielectric functions of the surrounding medium (real) and the cluster (complex), respectively. In the present work, the fitting of the absorption data has been done using this approximation, since we consider Ø 10 nm clusters. It is important to note that the expression (2.16) neglects scattering effects, which are likely to be small in the case of clusters as small as 10 nm. Indeed, the scattering becomes a dominant effect when the cluster size is much larger than the electron mean free path (from a diameter of typically 30 nm for  $Ag^{66}$ ).

To make use of this theory, the second part (material) has to come into play. In particular, one has to include in it the size and the dielectric functions of the cluster  $\varepsilon(\omega, r)$  and the surrounding medium  $\varepsilon_m$ .

#### The Dielectric Function

The dielectric function  $\varepsilon(\omega) = \varepsilon_1(\omega) + i\varepsilon_2(\omega)$ , also called the *permittivity* or *optical material function*, is a complex function describing the intrinsic properties of the material. It determines the position and the shape of the surface plasmon absorption peak. The dielectric function is related to the complex index of refraction N = n + ik by:

$$\begin{cases} \varepsilon_1(\omega) = n^2 - k^2 \\ \varepsilon_2(\omega) = 2nk \end{cases}$$
 (2.17)

 $<sup>^{\</sup>ast}$  A simple analytical derivation of Equation (2.16) was performed later on by Genzel and Martin  $^{65}.$ 

The derivation of the dielectric function of bulk metal is carried out using a Drude-Lorentz-Sommerfeld model. It considers first the influence of external fields on one single conduction electron, and then multiplies by the total number of conduction electrons. With such a method, the coupling between electrons is assumed to be maximum, since it does not introduce any dephasing between the considered electrons. This derivation leads to the expression:

$$\varepsilon(\omega) = 1 - \frac{\omega_p^2}{\omega^2 + i\gamma\omega} = \underbrace{1 - \frac{\omega_p^2}{\omega^2 + \gamma^2}}_{\varepsilon_1(\omega)} + i \cdot \underbrace{\frac{\omega_p^2 \gamma}{\omega(\omega^2 + \gamma^2)}}_{\varepsilon_2(\omega)}$$
(2.18)

where  $\gamma = \frac{v_F}{l_{\infty}}$  is a phenomenological damping constant,  $v_F$  is the Fermi velocity,  $l_{\infty}$  the bulk mean free path and  $\omega_P$  is the plasmon frequency. This equation gives the expression of  $\varepsilon_1(\omega)$  and  $\varepsilon_2(\omega)$ , the real part and imaginary part of the dielectric function, respectively.

At this point, only the conduction electrons are taken into account. However, it is clear that in a realistic situation, all other electrons from the core levels also contribute to the dielectric function. Thus, the core electron contributions (real and imaginary parts) have to be implemented. In the present work, this core electrons contribution was extracted from reference experimental optical constants of bulk gold <sup>67</sup>, from where the free electrons component derived in Equation (2.18) was subtracted. The real and imaginary parts of this reference bulk permittivity are plotted in Figure 2.14.

The dielectric function derived up to now is valid for bulk material. However, for small objects like clusters, the damping constant  $\gamma$ , related to the mean free path of electrons, is strongly affected by the size of the object. Indeed, if a cluster has a diameter 2R smaller than the bulk mean free path of conduction electrons  $(2R \leq \lambda_{\infty})$ , then  $\lambda_{\infty}$  becomes dependent on R ( $\lambda_R \propto R$ ), since the collisions with the cluster boundaries become dominant. Hence, an additional contribution proportional to 1/R has to be appended to the bulk damping constant:

$$\gamma(R) = \gamma + A \frac{v_F}{R}.\tag{2.19}$$

This dependency in 1/R reflects the ratio of the surface scattering probability ( $\propto 4\pi R^2$ ) with the number of electrons ( $\propto 4\pi/3R^3$ ). A is a proportionality factor and is commonly taken as 1, but can vary from one

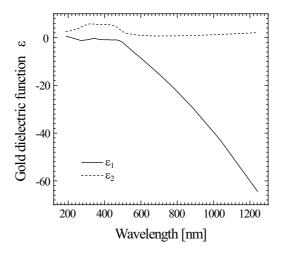


Figure 2.14: Experimental reference of the gold bulk dielectric function <sup>67</sup>, taking into account conduction and core electrons.

system to another <sup>68</sup>. The complex dielectric function for clusters is thus described by :

$$\begin{cases} \varepsilon_1(\omega, R) = 1 - \frac{\omega_p^2}{\omega^2 + \gamma(R)^2} + \varepsilon_{1,core} \\ \varepsilon_2(\omega, R) = \frac{\omega_p^2 \gamma(R)}{\omega(\omega^2 + \gamma(R)^2)} + \varepsilon_{2,core}. \end{cases}$$
 (2.20)

The dielectric function given by the relations (2.20), with  $\gamma(R)$  given by Equation (2.19), inserted in the  $1^{st}$  order Mie absorption expression (2.16) gives a good description of the extinction of light in a large metallic cluster (typically  $\emptyset \sim 10 \,\mathrm{nm}$ ). In diluted liquid environments, this model still holds as long as there is no interaction between the clusters. The total extinction is in this case the sum of each cluster's contribution.

## 2.3 The Link between Electrical and Optical Material Properties

The electrical properties of a material are usually associated with its conductivity  $\sigma$ . On the other hand, the optical properties are generally described by its dielectric function  $\varepsilon$ . Clearly, these two quantities are tightly associated with each other, since they are both related to the material electrons' behaviour. By considering an electromagnetic wave of angular frequency  $\omega$  propagating through a material of conductivity  $\sigma(\omega)$ 

and relative permittivity  $\varepsilon_r(\omega)$ , one knows that the electric displacement  $\vec{D}$  and current density  $\vec{j}$  are related to the electric field  $\vec{E}$  by the following relations\*:

$$\begin{cases} \vec{j}(z,\omega) = \sigma(\omega)\vec{E}(z,\omega) \\ \vec{D}(z,\omega) = \varepsilon_0 \varepsilon_r(\omega)\vec{E}(z,\omega) \end{cases}$$
 (2.21)

The relative permittivity  $\varepsilon_r(\omega)$  and the conductivity  $\sigma(\omega)$  constitute the core of these relations. They enter into the determination of the optical properties of a material, expressed by the *dielectric function* of the material<sup>60</sup>:

$$\varepsilon(\omega) = \varepsilon_0 \varepsilon_r(\omega) - \frac{i\sigma(\omega)}{\omega} \tag{2.22}$$

In the case of dc fields,  $\sigma$  and  $\varepsilon_r$  express two distinguishable physical processes.  $\sigma$  describes the free charges, moving freely over arbitrary distances in response to the dc field. Whereas  $\varepsilon_r$  describes the bound charges, i.e. those that are bound to equilibrium positions and stretch to new positions due to the dc field. In the case of ac fields however, this distinction blurs. The free charges do not move arbitrarily far, but oscillate back and forth with the frequency of the field, whereas the bound charges no longer come to rest at new equilibrium positions, but also oscillate at the field frequency. If  $\omega$  is sufficiently low<sup>†</sup> ( $\omega \ll 1/\tau$ , with  $\tau = \frac{l}{v_F}$ ), the distinction can still be preserved. Indeed, the free charge velocities respond in phase with the field and the bound charge velocities respond out of phase with the field. However, at higher frequencies, this distinction fully disappear, as the free charges can have a substantial outof-phase response and the bound charges can have a considerable in-phase response. Hence, at high frequencies, the distinction between free charges and bound charges, represented by  $\sigma(\omega)$  and  $\varepsilon_r(\omega)$  respectively, is only a convention. The response of all electrons (core and conduction) is lumped into the single dielectric constant  $\varepsilon(\omega)$  given by Equation (2.22). Hence,  $\varepsilon(\omega)$  includes the contributions of both partially filled and filled bands to the current. This convention enables to use the same theory notations for metals and insulators, where all charges are considered bound.

<sup>\*</sup> Note that they are local, thus they are only valid if the spacial variation of the fields is small compared to the electron mean free path in the material.

<sup>&</sup>lt;sup>†</sup> This is the case in our experiments, as we used visible light ( $\omega \sim 10^9 \, \text{1/s}$ ) and  $\sim 10 \, nm$  gold nanoparticles :  $\tau_{Au} \sim 10^{-14} \, \text{s} \; (v_{F(Au)} = 1.4 \cdot 10^8 \, \text{cms}^{-1})$ .

### Part I One Dimensional Systems

Nanoparticle assemblies can be classified into three categories: onedimensional (1D), two-dimensional (2D) and three-dimensional (3D) systems<sup>69</sup>. 1D assemblies of nanoparticles are seldom reported, due to the difficulties arising with their preparation. However, their unique properties, such as inter-particle electronics <sup>32,70</sup>, photonics <sup>71,72</sup>, magnetism <sup>73</sup> or energy transfer<sup>74</sup>, make them essential, not only for the production of novel devices, but also for the understanding of fundamental phenomena at the nanometre-scale. So far, different methods have been elaborated to prepare such structures<sup>75</sup> taking advantage of the diverse mechanical, physical and chemical phenomena, such as insertion inside nanopores<sup>71</sup>, electrostatic interactions<sup>76,77</sup>, magnetic influence<sup>73</sup>, dielectrophoresis <sup>32,78</sup>, adsorption on linear biomolecules <sup>79,80</sup>, or surface confinement effects<sup>81</sup>. Although considerable research has been devoted to the fabrication of 1D nanoparticle assemblies, rather less attention has been paid to the development of a reliable and reproducible method for such a fabrication. Indeed, reproducibly assembling nanoparticles in a 1D fashion remains a challenging task.

In this part, we focus on a method allowing the preparation of stable 1D assemblies of nanoparticles, for electronic investigation<sup>82</sup>. A controllable technique to position nanoparticles is reported, which combines nanolithography and electrostatic trapping of colloids. The latter consists of aligning and contacting colloids by means of dielectrophoresis (ac trapping)<sup>83,84,85</sup>, a technique previously used to manipulate a variety of micrometre- and nanometre-size objects, including bio-polymers <sup>86,87</sup>, cells<sup>88</sup> and metallic colloids<sup>31,45,78,89,90,91</sup>. Our approach addresses the lack of a systematic method, in particular concerning the assembly of metallic particles in sub-micrometre gap sizes. In this study, we concentrate on an ac trapping process of 10 nm to 100 nm nanoparticles, inside gaps with sizes ranging between 10nm and 500 nm. The crucial role of relevant trapping parameters is emphasised throughout an analysis performed on more than 100 experiments. In addition, we demonstrate that this technique allows the reproducible preparation of nanoparticle chains between metallic electrodes. Remarkably, this technique also enables the formation of continuous nanowires of tunable diameter between distant micrometre-scale electrodes, by fusing the trapped colloids. Ultimately, we show that this process, along with the final shape and conductance of the as-prepared junctions, can be controlled via the fine tuning of the relevant trapping parameters.

# 3

## ELECTROSTATIC TRAPPING OF NANOPARTICLES

The electrostatic trapping of nanoparticles involves three fabrication steps. Metallic micro-electrodes with nanometre-scale separation-gap are fabricated on a flat substrate. The colloidal solution is prepared in parallel. Then, the colloidal solution is poured on the top of the electrodes and the trapping process can be initiated. In the following, we elaborate on the first and third steps, whereas the colloids' synthesis is described in Appendix B.1.

## 3.1 Nanometre-spaced Electrodes : The Real Challenge ?

Great efforts have been spent in the past few years to reduce electrodes' separation, with a view to *Molecular Electronics*. A large range of different techniques have been investigated, such as e-beam lithography <sup>92</sup>, electromigration <sup>93,94,95</sup> (see also Appendix D.2), chemical electrodeposition <sup>46</sup> or nanowire lithgraphy <sup>96,97</sup>, with the only goal to produce few nanometre-spaced electrodes. But is this the key issue? How can one introduce a molecule in between electrodes and know whether and if so, how the molecule is contacted remains a challenging question. Using nanoparticles as linkers resolves some of these issues, in particular the one related to the inter-electrode gap size.

Planar micrometre-scale gold electrodes were patterned on a  $Si/SiO_2$  substrate using conventional UV and electron-beam lithographies. Before each step of fabrication, the substrate was cleaned in an acetone bath, followed by an isopropanol bath and finally it was exposed to an ozone treatment for 5 minutes. After resist spinning, exposure and development, a Ti adhesion layer was deposited prior to evaporation of a Au layer. As demonstrated in Figure 3.1, we can vary the electrodes shape and the gap

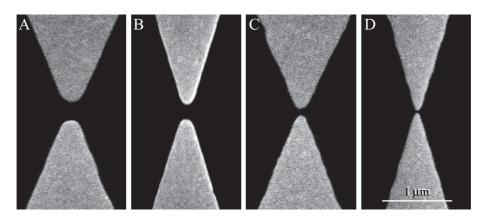


**Figure 3.1:** SEM images of Au electrode pairs fabricated by e-beam lithography, exhibiting different gap size : A.  $d=240\,\mathrm{nm}$  B.  $d=190\,\mathrm{nm}$  C.  $d=75\,\mathrm{nm}$  D.  $d=25\,\mathrm{nm}$ .

size, typically ranging from 20 to 200 nm. As described in Section 3.2, these two aspects are of crucial importance to the electric field applied between the electrodes (see Figure 3.4). Using an angle evaporation technique, the gap size between the electrodes could be reduced to less than 20 nm (see Appendix D.1), despite a relatively small yield ( $\sim$ 5%). We also could reduce the gap size by evaporating platinum instead of gold as electrode material, taking thus the advantage of the lower mobility of Pt atoms at room temperature. However, since Au electrodes are the most commonly used in  $Molecular\ Electronics$ , we focused on this material. Further details on the fabrication of the micro-sized electrodes are available in Appendix B.2.

#### 3.2 Taking Advantage of Dielectrophoresis

The trapping of gold nanoparticles was performed via dielectrophoresis (DEP) by applying an ac electrical field between two micro-fabricated electrodes\*. Under the influence of the electrical field, both particles and suspending medium are influenced by electrostatic forces. In contrast to electrophoresis, which occurs when a charged particle is plunged in a dc electric field, DEP only occurs when the particle exhibits induced charges on one hand, and stands in a non-uniform electric field on the other hand,

 $<sup>^*</sup>$  The trapping of Pd nanoparticles has also been considered to improve the quality of the contact. However, their trapping was found to be very similar, without any noticeable advantage.

as schematically shown in Figure 3.2. As a matter of fact, a metallic neutral particle within an electric field is polarised, via charge separation, thus inducing a layer of counter charges from the surrounding medium at the surface of the particle. In the case of a greater interfacial polarisability of the particles compare to the medium, more charges accumulate inside the interface rather than outside. This effect induces a dipole in the direction of the field. If, on the contrary, the polarisability of the particles is less than the medium, the induced dipole is oriented in the other direction (Figure 3.2A & B, respectively). In an ac electric field, this dipole oscillates at the same frequency, thus causing no movement of the particle. However, if the field is non-uniform, the density of field lines is greater on one side of the particle than the other. This leads to an imbalance of forces on the induced dipole, resulting in particle movement (Figure 3.2C & D). Hence, in the case of larger particle polarisability, the particle experiences a force  $\vec{F}_{DEP}$  towards the strong field region (Figure 3.2C). On the contrary, if the particle has a lower polarisability than the medium, the force experienced by the particle is oriented reversed to the strong field region (Figure 3.2D). Moreover, the DEP also strongly depends on the frequency of the field. Indeed, at low frequencies, the movement of free charges can follow the direction changes of the field, bringing the respective conductivities as dominant parameters. Whereas at high frequencies, the free charges do not have sufficient time to respond and the dominant mechanism for charging the interface is the polarisation of the bound charges, namely the respective permittivities. Hence, the direction of the induced dipole may change going from one frequency to another.

The dielectrophoretic force  $(\vec{F}_{DEP})$  acting on a homogeneous, isotropic particle of radius r is thus proportional to the dipole moment  $\vec{p}$  (the polarisation times the volume) and the gradient of the electrical field  $\vec{E}$ :

$$\vec{F}_{DEP} = (\vec{p} \cdot \vec{\nabla}) \vec{E}. \tag{3.1}$$

The dipole moment can be expressed in term of the permittivities ( $\tilde{\varepsilon}_p$  for the particle and  $\varepsilon_m$  for the medium)<sup>85</sup>:

$$\vec{p} = 4\pi\varepsilon_m r^3 \left[ \frac{(\tilde{\varepsilon}_p - \varepsilon_m)}{\tilde{\varepsilon}_p + 2\varepsilon_m} \right] \vec{E}.$$
 (3.2)

The time-averaged force on the particle is thus given by  $^{84,85}$ :

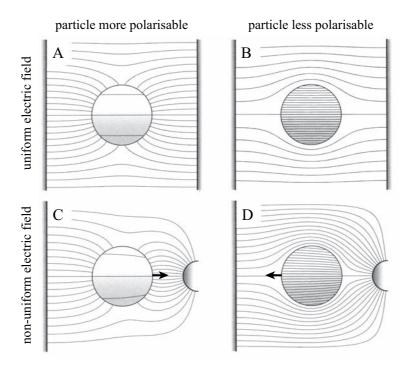


**Figure 3.2:** Electric field lines in four different cases: particle more polarisable (A & C) or less polarisable (B & D) than the medium, in an uniform (A & B) or non-uniform (C & D) field. In the latter case, a force  $\vec{F}_{DEP}$  drives the most polarisable element (particle or medium) in the high field region <sup>85</sup>.

$$\langle \vec{F}_{DEP} \rangle = \pi \varepsilon_m r^3 \Re \left[ \frac{(\tilde{\varepsilon}_p - \varepsilon_m)}{\tilde{\varepsilon}_p + 2\varepsilon_m} \right] \cdot \vec{\nabla} |\vec{E}|^2.$$
 (3.3)

Note that though the permittivity of the medium  $\varepsilon_m$  is assumed to be real, the particle permittivity  $\tilde{\varepsilon}_p$  is in general complex and given by  $\tilde{\varepsilon}_p = \varepsilon_0 \varepsilon_r - i \frac{\sigma_p}{\omega}$ , as described in Section 2.3. The force given by Equation (3.3) typically ranges between 0.1 pN to 1 pN for a 200 nm particle <sup>85</sup>.

Considering the above, dielectrophoresis can be used, for instance, as a tool to trap nanoparticles in between electrodes. Interestingly, the interaction between nanoparticles due to the induced dipoles, as in our situation, favours the formation of particle chains. Indeed, ruled by their induced dipole, similar nanoparticles attract each other when aligned parallel to the applied field, as shown in Figure 3.3, and repel each other when in perpendicular alignment <sup>84</sup>. Moreover, in the first case, it was

shown that the effective dipole moment of a particle chain  $\vec{p'}$  is larger than the simple addition of all particles moment  $\vec{p}$ . More concretely, whereas the moment of a single particle is  $\vec{p} = 4\pi\varepsilon_m R^3 \vec{E_0}$ , the moment of a 2-particles chain is  $\vec{p'} = 19.2\pi\varepsilon_m R^3 \vec{E_0}$ , the one of 3-particles chain is  $\vec{p'} = 48.5\pi\varepsilon_m R^3 \vec{E_0}$ , etc, leading to a normalised moment per particle of 1, 2.4, 4, etc, respectively. This means that the longer the chain, the more stable and the more it attracts new particles. As a matter of fact, in our systems, the particles are driven by dielectrophoresis forces and pre-align along the field lines at the smallest distance between the electrodes, in spite of their electrostatic repulsion (short range in an electrolyte). Then, because they are aligned parallel to the external field, they attract each other to ultimately form particle chains, as shown in Figure 3.4A\*.

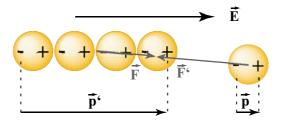


**Figure 3.3:** Particle chain formation due to dipolar attraction between aligned particles in an electric field, with  $\vec{p}$  and  $\vec{p'}$  the effective dipole moments of a particle and a chain respectively, and  $\vec{F}$  and  $\vec{F'}$  the corresponding forces.

Moreover, as the field is the strongest at the extremities of the electrodes, the nanoparticle chains are fairly likely to form in the middle of the junction, where the gap is the smallest, as demonstrated in Figure 3.4A & 3.4B. Indeed, a simulation<sup>†</sup> of the field as a function of the position nearby the electrodes showed that the field reduces dramatically over a few tens of nanometres  $(|\vec{E}(r)| \propto \frac{1}{r^2})$ . Along the equipotential 1 V, the field value was found to be about 10 MV/m in the central region, 6 MV/m at the first arrow loop and 2.5 MV/m at the second set of arrows. Hence, the dielectrophoresis effect only acts on nanoparticles in a small region of about  $0.16 \,\mu\text{m}^2$  centred on the gap<sup>‡</sup>. However, note that the size and

 $<sup>^*</sup>$  It has been suggested as well that electrohydrodynamic flows also contribute to the alignment of nanoparticles  $^{89,98}$ .

 $<sup>^\</sup>dagger$  The simulation was performed with a finite element calculation, via the software FemLab  $^{\odot}$  .

<sup>&</sup>lt;sup>‡</sup> The experiments revealed no trapping for an electric field below  $2 \,\text{MV/m}$  in the central region, suggesting that in case of higher field, only the area with  $\vec{E} > 2 \,\text{MV/m}$ 

shape of the gap, as exposed in Figure 3.1, strongly influences the shape and strength of the electric field, leading to large variations in the trapping behaviour. Since the structure cannot be accurately controlled, a quantitative study is hardly achievable.

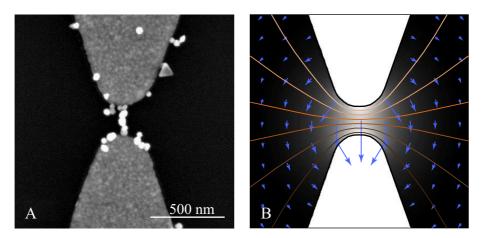


Figure 3.4: A. SEM image of a junction with a 200 nm-gap to which a voltage of 2 V was applied in the presence of nanoparticles. A nanoparticle chain was formed in the middle of the gap, along the highest field line. B. Simulation of this junction: electric field (arrows and gray scale plot where black is 0 and white 10 MV/m) and equipotentials (from 0 (dark) to 2 V (bright)).

The frequency of the electrical field used throughout our experiments was 1 MHz, allowing the manipulation of nanoparticles with diameter ranging between 10 nm and 100 nm. Note that at such a frequency, the circuit cables and components have non-negligible capacitance, inducing dephasing. To minimise such disturbances, a broadband electronic box was built\*. The basic components to perform the dielectrophoretic trapping, visible in Figure 3.5, are the following: A series capacitor  $C_s$  was mounted after the input to filter out any possible dc component and avoid electrochemical processes or electromigration <sup>99</sup>. It also prevents further effects due for instance to the electrophoretic mobility of the ionic solution, which can influence the motion of the suspended nanoparticles. In order to measure the current flow through the sample, a variable series resistor  $R_s$  was placed within the circuit. In addition, the value of  $R_s$  was carefully chosen to limit the current flowing through the junction.

exhibits nanoparticle migration.

<sup>\*</sup> See the details in Appendix C.1.

Both a lock-in amplifier and a standard digital oscilloscope were used in parallel to record the voltage drop over the series resistor. The lock-in provided information over the whole trapping process, from the moment the ac voltage was applied to the moment the colloids were anchored within the gap between the electrodes. This measurement provided information on the time needed for a particle bridge to form and on the impedance change of the device upon trapping. The oscilloscope was adjusted to trigger exactly at the trapping event, when a significant increase of the current flowing in the circuit could be observed due to the lowering of the junction resistance. After the trapping event, the process was self-terminating. Indeed, as soon as a particle chain bridges the two electrodes, the resistance of the device drops and consequently the potential difference across the gap decreases rapidly, so that the electrical field  $\vec{E}$ vanishes. As soon as no more field is applied, the dielectric force becomes zero as well, and no other nanoparticles are attracted specifically in that region. Finally, as fast as possible after the contacting, the solution was removed, to avoid accidental deposition of nanoparticles moved there by Brownian motion.

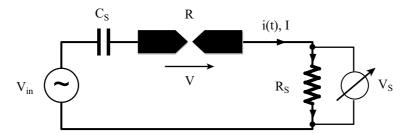


Figure 3.5: Schematics of the trapping circuit. Both an oscilloscope and a lock-in amplifier record the voltage drop  $V_s$  over the series resistor  $R_s$ . A series capacitor  $C_s = 1.5 \,\mathrm{nF}$  is used to filter out dc current to avoid electrochemical and electromigration effects. Together,  $R_s$  and  $C_s$  form the total series impedance  $Z_s$ , which limits the current through the device. For the detailed circuit, see Appendix C.1.

#### 3.3 Concluding Remarks

Summarising this chapter, we described here both the conceptual ideas standing behind the dielectrophoretic trapping of metallic nanoparticles, and the technical method to enable the monitoring of this process. When properly understood and controlled, it appears to be a promising method to control the formation of metallic nanoparticle chains. Note that by adjusting the gap size between the electrodes and the diameter of the particles, it is possible to fabricate chains of different length and diameter, respectively. Moreover, as presented in the next chapter, by fine tuning the trapping parameters, it is possible to choose the "quality" of the contact in between the nanoparticles, thus forming nanoparticle chains or homogeneous metallic wires.

# 4

## ELECTRICAL TRANSPORT IN 1D NANOPARTICLE ASSEMBLIES

## 4.1 ON COURSE TO CONTROL THE FINAL DEVICE RESISTANCE

As mentioned in the previous section, the trapping of nanoparticles inside the gap may be monitored by tuning the trapping parameters, in particular the applied voltage intensity V and its frequency f (via the respective permittivities). The trapping process is performed within a typical time  $t_1$  (see Figure 4.1A). As demonstrated below, the anchoring process is rather tuned by the series resistance  $R_s$ , which, combined with the impedance of the capacitor ( $|Z_c| \approx i110\,\Omega$  at 1 MHz), determines the total series impedance  $Z_s$ . This series impedance limits the power injected in the junction. The anchoring process takes place within a typical time  $t_2$ . The presence of two distinct processes, governed by two different sets of parameters shows the importance of a systematic study, on each of these sets of parameters separately.

We explored various types of colloids with a main focus on chargestabilised Au colloids with a diameter of  $25 \pm 5$  nm. To investigate the trapping process in detail, the current through 103 junctions was measured during and after the trapping of these specific particles. All samples were prepared following the same procedure, and care was taken to ensure a similar surface treatment prior to performing the trapping experiments. Figure 4.1A shows a typical lock-in measurement of the current I flowing through a junction during trapping. First, a colloidal solution droplet was deposited on the device (t < 0). Next, an ac trapping voltage  $V_{in}$  was applied at t = 0 to attract the nanoparticles to the junction. This gave rise to a detectable leakage current through the solution (arrow 1). After the duration  $t_1$  of typically a few seconds to one minute, a large current increase was suddenly observed (arrow 2). This event signals the trapping of nanoparticles and the formation of a conducting bridge within the gap.

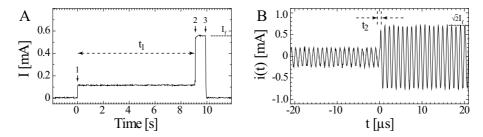


Figure 4.1: A. Typical record of the rms current I through the junction during both trapping and anchoring processes, with  $V_{in} = 1$  V and series impedance  $|Z_s| = 467 \,\Omega$ . Arrows 1, 2 and 3 mark the time when the voltage was applied, the contact was made and the voltage was set to 0, respectively. The characteristic time for trapping,  $t_1$ , is defined as the time between arrows 1 and 2. B. Close-up view of the ac current i(t) measured with an oscilloscope around the contacting event (t = 0).

After this increase, the current remained constant (no further change of the junction resistance) and finally, the input voltage  $V_{in}$  was set to zero (arrow 3). We note that in a few particular cases the current did not increase in a single step, as shown in Figure 4.2A, but rather displayed multiple steps, suggesting the formation of a few conducting bridges in parallel. It is however difficult to associate with certainty these steps to the anchoring of the colloids one after the other. Figure 4.1B shows a typical oscilloscope trace of i(t), set up to trigger exactly at the current increase (arrow 2, Figure 4.1A). We see that the junction changes its resistance typically within  $t_2 \sim 1 \,\mu\text{s}$ . However, we could observe cases where the anchoring took place in more than  $5 \,\mu\text{s}$  (see Figure 4.2B).

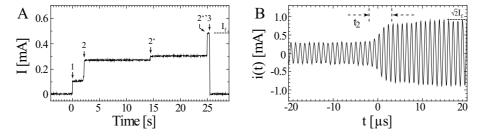
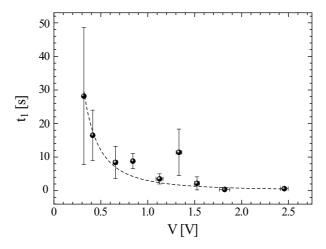


Figure 4.2: A. Particular lock-in record of the current I through the junction, taking place in several steps (with  $V_{in}=1\,\mathrm{V}$  and  $|Z_s|=467\,\Omega$ ). B. Particular oscilloscope record of the current i(t) at the contacting event (t=0), where the anchoring process took place in  $t_2>5\,\mu\mathrm{s}$  (with  $V_{in}=1\,\mathrm{V}$  and  $|Z_s|=341\,\Omega$ ).

Figure 4.3 shows the dependence of the average trapping time  $t_1$  on the voltage over the junction V (for  $t < t_1$ ). The trapping time roughly scales with the inverse of the voltage squared  $1/V^2$ , which agrees with the expectation for a driven particle movement impeded by viscous friction. In that case the velocity scales with the driving force which is, according to the expression for the dielectrophoretic force, proportional to the electric field squared, and hence to the voltage squared.



**Figure 4.3:**  $t_1$  as a function of the voltage drop over the junction V (at  $t < t_1$ ). Each point is an average over several data points; the error bars correspond to the standard error. The dotted line represents a  $1/V^2$  dependence.

After each trapping experiment, scanning-electron microscopy (SEM) inspection of the samples revealed that in 67 cases the junctions showed no sign of breakdown\*. Figure 4.4 reports a set of representative results. First, we focus on Figure 4.4A and B. Here, nanoparticles with a relatively large diameter of  $120 \pm 20 \,\mathrm{nm}$  were trapped into  $\sim 500 \,\mathrm{nm}$  large gaps. The trapping conditions for both cases were identical, except for the applied voltage  $V_{in}$ : 2V in case A and 1V in case B. We clearly observe a larger number of trapped particles in A than in B. This illustrates that one can tune the number of nanoparticles bridging the gap by adjusting the trapping voltage. The electric field required for optimal trapping amounts to about  $E \approx 10^7 \,\mathrm{V/m}$ . In Figure 4.4B, a well-ordered chain of nanoparticles was formed with a junction resistance of only  $50 \,\Omega$ . This is surprising and indicates that after the nanoparticles were trapped,

<sup>\*</sup> See full table in Appendix E.1.

a second, 'anchoring' process took place. During anchoring, the colloids become physically and electrically connected, leading to a low final resistance. Figure 4.4C shows a device in which even smaller particles, i.e.  $25 \pm 5 \,\mathrm{nm}$ , were trapped, with an applied voltage  $V_{in} = 1 \,\mathrm{V}$ . Remarkably, the individual colloids are not distinguishable any longer. Instead of building a chain, as in Figure 4.4B, the particles have fused together forming a wire with a well defined diameter. The final resistance of this wire is comparatively low, i.e.  $160\,\Omega$ . Figure 4.4 shows that the anchoring process can lead to the formation of two distinct structures: chains or wires. Below, we will discuss this phenomenon in more detail. Finally, in Figure 4.4D and E, we show examples of junctions with relatively large final resistances in the  $M\Omega$  range. In Figure 4.4D, a single nanoparticle (25  $\pm$  5 nm) was trapped. In contrast to Figure 4.4A-D where charge-stabilised colloids were used, Figure 4.4E shows a typical result for the trapping of dodecanethiol  $(C_{12}H_{25}S)$ -functionalised nanoparticles of 10 nm diameter within a 30 nm gap. Unlike the former cases, devices made with functionalised particles never displayed fusing and the resistance values were always large ( $> M\Omega$ ).

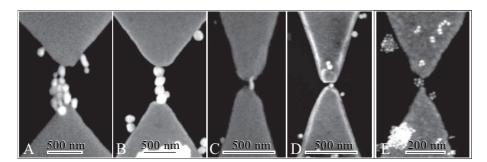


Figure 4.4: Scanning electron micrographs of junctions prepared under various conditions. A. Large gap (500 nm) with large nanoparticles (120 ± 20 nm): parameters  $V_{in} = 2 \, \mathrm{V}$ ,  $|Z_s| = 111 \, \Omega$ ; final resistance  $R_f = 280 \, \Omega$ . B. Large gap (560 nm) with large nanoparticles (120 ± 20 nm):  $V_{in} = 1 \, \mathrm{V}$ ,  $|Z_s| = 111 \, \Omega$ ;  $R_f = 50 \, \Omega$ . C. Small gap (40 nm) with a wire formed by small nanoparticles (25 ± 5 nm):  $V_{in} = 1 \, \mathrm{V}$ ,  $|Z_s| = 148 \, \Omega$ ;  $R_f = 160 \, \Omega$ . D. Small gap (30 nm) with a single small nanoparticle (25 ± 5 nm):  $V_{in} = 1.8 \, \mathrm{V}$ ,  $|Z_s| = 467 \, \Omega$ ;  $R_f = 4.8 \, \mathrm{M}\Omega$ . E. Small gap (20 nm) with small  $C_{12}$ -functionalized nanoparticles (10 ± 1 nm):  $V_{in} = 1 \, \mathrm{V}$ ,  $|Z_s| = 147 \, \Omega$ ;  $R_f = 4 \, \mathrm{M}\Omega$ .

In 11 cases of the 67 successful trapping experiments with 25  $\pm$  5 nm diameter charge-stabilised nanoparticles, the final junction resistance  $R_f$ 

was much larger than  $1 M\Omega$ . This indicates that no metallic contact was established between the nanoparticles and the electrodes. An overview of the rest of the data set (56 experiments) is given in Figure 4.5. Here, we plot the final device resistance  $R_f$  as a function of the current  $I_f$ , both measured at the end of the trapping and anchoring process. There is guite some scatter in the final resistance of the devices. Nevertheless, the data set is confined between a lower and an upper bound given by the voltage  $V_f = I_f R_f$ . More precisely, the voltage over the junction always lies in between 0.2 V and 1.6 V, as indicated by the dotted lines, a typical value being 0.9 V. The lower bound in Figure 4.5 is related to the trapping process: if the electric field is too small, trapping does not take place. In contrast, a voltage that is too large leads to sample destruction after trapping as evidenced by 'burnt' electrodes which are modified on a macroscopic scale. This breakdown process is likely related to a thermal run-away by excessive Joule heating as reported in electromigration experiments on nanojunctions 100. The open and solid data points in Figure 4.5 relate to two different kinds of junctions. The solid dots refer to junctions in which the nanoparticles formed chains during the trapping process (cf. Figure 4.4B), whereas the open dots relate to wire formation (cf. Figure 4.4C). It appears that the two subsets group together in Figure 4.5, despite the clear scatter. Hence, Figure 4.5 forms a good basis to speculate about the possible processes behind anchoring, chain and wire formation, as well as device breakdown.

We first focus on the moment when a set of nanoparticles is being trapped in the junction at  $t = t_1$ . These particles experience a large electric field in the gap region  $\sim 10^7 \, \text{V/m}$ , which induces a dipole in each of them. Consequently, the dipole-dipole interaction between the particles becomes significant, tending to line up the particles in the junction. This explains the preference for the initial chain formation. At that point, the charge-stabilised particles are not yet interconnected, so that the whole voltage drops over the tiny gaps ( $\leq 1 \text{ nm}$ ) between the particles. This has two consequences. First, the electric field is much more localised than before chain formation. Hence, the range of the DEP force is decreased, leading to a much smaller trapping probability for left-over particles in the solution. In this way, DEP is self-limiting. Second, the field over the gaps between the individual colloids tend to become very high,  $\geq 10^8 \, \text{V/m}$ . At such fields, surface diffusion of Au atoms is enhanced in the direction of the gap and can lead to the formation of narrow Au bridges between the nanoparticles <sup>101,102</sup>. If no connections are formed, a device will have a

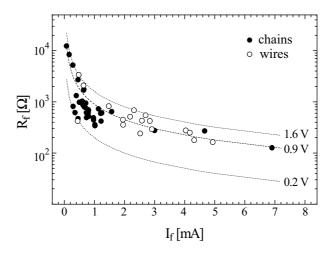


Figure 4.5: Final resistance  $R_f$  versus current  $I_f$  of the junctions showing successful trapping and anchoring (56 devices). The voltage over the junctions  $V_f = I_f R_f$  is bound by 0.2 V from below (no trapping) and 1.6 V from above (breakdown after trapping), as indicated by dotted lines. A typical voltage is 0.9 V (dashed line). Solid dots: chain formation; open dots: wire formation (as extracted from SEM images).

high final resistance ( $\gg 1 \text{ M}\Omega$ ), as observed in 11 of our 71 junctions made with charge-stabilised particles. As mentioned above, junctions prepared with alkanethiol-covered particles always yielded high resistance values, suggesting that the alkanethiol shell protects the colloids against field-driven atomic migration. However, in most devices with chargestabilised particles, the particles were interconnected and the resistance of the devices dropped dramatically. One may wonder what determines the final value  $R_f$  of these junctions. To address this point, we refer to Figure 4.6A, where a histogram of  $log(R_f/|Z_s|)$  is plotted. This graph describes the probability distribution of the ratio of  $R_f$  to the total series impedance  $|Z_s|$ . We find that  $R_f$  is typically of the same order of magnitude as  $|Z_s|$ . The histogram features a clear peak with a maximum around a ratio of  $log(R_f/|Z_s|) = 0.2$ , corresponding to  $R_f = 1.6|Z_s|$ . In the inset of Figure 4.6A, we show a stacked bar plot of the percentage of chains (dark) and wires (light) for three ranges of  $|Z_s|$ . Interestingly, chains are more common for higher  $|Z_s|$ , while wires are mostly found for lower  $|Z_s|$ . Figure 4.6A indicates that we can tune (at least roughly) the device properties via the series impedance.

To understand this, we bring forward a possible model of wire for-

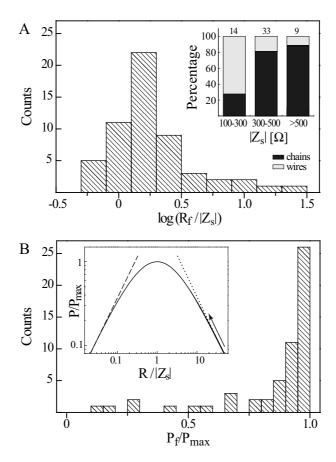


Figure 4.6: A. Histogram of  $log(R_f/|Z_s|)$ , for the data in Figure 4.5. A single peak is seen with a maximum around  $log(R_f/|Z_s|)=0.2$ . The inset shows the percentage of chains (dark) and wires (light) for different values of  $|Z_s|$ . Wires are more favourably formed for lower  $|Z_s|$ . B. Histogram of  $P_f/P_{max}$ , where  $P_f=V_f^2/R_f$ . A clear majority of the devices has  $P_f\approx P_{max}$ . The inset shows a calculation of  $P/P_{max}$  as a function of  $R/|Z_s|$ , which reaches its maximum at  $R=|Z_s|$  (Calculation for  $Z_s=452-134i\Omega$ ). The arrow indicates that the resistance of our junctions decreases during homogenisation. The dashed and dotted lines refer to the limiting cases of current- and voltage biasing, respectively.

mation. We first note that a change in shape from chain to wire leads to a decrease of the total surface energy. Hence, we expect that surface tension is the effective driving force for the fusing process. Also, in order to transform a chain of spherical particles into a rod-like wire, a consid-

erable diffusion of Au atoms is needed. Since diffusion is an activated process, an increase of the junction temperature by Joule heating will clearly facilitate wire formation. Before fusing,  $R \gg |Z_s|$  and the junction is voltage-biased with the power P dissipated over the junction given by  $P = V_{in}^2/R$ . Once atomic diffusion sets in and the gaps start to fill up, the resistance decreases and consequently the dissipation increases. If the applied voltage  $V_{in}$  is too large, this can lead to a thermal run-away and sample breakdown. However, the series impedance  $Z_s$  also has an effect on P. It can self-limit the thermal run-away process for moderate  $V_{in}$ . To see this, we note that the junction would be current-driven in the opposite regime  $R \ll |Z_s|$ . In that case, the local dissipation P is given by  $P \approx RI^2$  and decreases with decreasing R, thus limiting the fusion process. The full dependence of P on  $R/|Z_s|$  is shown in the inset of Figure 4.6B. There is a maximum power  $P_{max} = V_{in}^2/4|Z_s|$  at  $R = |Z_s|$ . The dashed and dotted lines indicate the dissipation in the limiting cases of effectively current-biased and voltage-biased junctions, respectively. Based on this consideration, we expect the process to stop when  $R \approx Z_s$  where the dissipation P reaches its maximum. Hence, the final dissipation  $P_f$ , measured at the end of successful junction formation, should be close to  $P_{max}$ . In Figure 4.6B, we display a histogram of  $P_f/P_{max}$  for all data points in Figure 4.5. For the vast majority of our devices, Figure 4.6B shows that  $P_f \approx P_{max}$ , as anticipated. Because the final resistance  $R_f$  is generally a bit larger than  $|Z_s|$  (Figure 4.6A), we infer that the process tends to stops to the right of the maximum in the inset of Figure 4.6B.

Relating the junction temperature T to the power P is not straightforward, but it can be stated that T is related to the volume power density p. If we assume for simplicity that only the junction cross-section A changes during wire formation, but not its length L, we have p := P/AL. Because  $R \propto 1/A$  one may also write  $p \propto PR$ . Hence, in the beginning, when  $R >> |Z_s|$  and  $P = V_{in}^2/R$ , the power density is constant, even if A increases due to the thermally driven diffusion of Au atoms. This homogenization process can therefore go on at constant temperature until the assumption  $R >> |Z_s|$  is no longer valid. Then, p and hence T will decrease, limiting atomic diffusion. This picture suggests that the homogenisation process can proceed further for small  $|Z_s|$  as compared to large  $|Z_s|$ . It therefore becomes understandable why wire-like devices appear for small  $|Z_s|$ , whereas chain-like ones appear for large  $|Z_s|$ , consistent with the inset of Figure 4.6A.

In the previous discussion, electromigration was ignored, since it does

not occur for the ac current densities we apply <sup>99</sup>. In fact, electromigration at similar dc current densities leads to gap formation <sup>20,100,103</sup>, which is the *opposite* effect compared to the new 'gap-closing' process that we report here. Interestingly, the series impedance and Joule heating play a similar role in electromigration experiments as in the work presented here <sup>100</sup>. We performed electromigration experiments in a fused wire (see Appendix D.2). This did indeed lead to nanometre-sized gap formation, as observed by SEM and confirmed by a finite tunnel resistance. We therefore speculate that repeated gap formation and closing should be possible by using ac and dc voltages, alternately.

#### 4.2 Low Temperature Characteristics of Nanoparticle Chains

We demonstrated in the last two sections a reproducible method to form nanometre-scale wires and chains, via nanoparticle assembly. This type of structures exhibit interesting transport characteristics, depending on the "degree" of fusing of the nanoparticles. As an example of what one can observe, we present the characteristics of two distinct cases: a wire and a high-resistance chain.

In both cases, the differential conductance  $(\frac{dI}{dV})$  was recorded via a 4-point ac measurement, as a function of a ramped bias voltage. Then, an integration of the curve was performed to get the current dependence (I-V) curve. To avoid any damage of the junction, a setup minimising the current flow was used (schematic of the circuit: Appendix C.1.3).

For wires and low-resistance chains, the current-voltage characteristic was found to be linear at room temperature (RT) for a bias voltage from -50 mV to 50 mV. At low temperature (4.2 K), a dip of small amplitude (< 10%) in the differential conductance is observed, as shown in Figure 4.7. A similar behaviour has been observed in electrochemically fabricated atomic scale gold nanojunctions  $^{104}$ , and attributed to Coulomb interactions. However, in our case, we have no evidence in favour of this interpretation. It may also be due to a partial quenching of the gold states by helium atoms  $^{105}$ , as the measurements were led in liquid helium.

In the case of the high-resistance chains, typically  $\sim 100 \, k\Omega$ , important deviations from metallic behaviour are observed. At 4.2 K, the differential conductance exhibits a significant suppression at low bias voltage (see Figure 4.8). By ramping the bias voltage to a maximum value of 5 V, we thus observe a non-linear I-V dependence. This non-linearity,

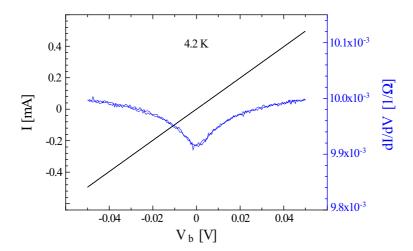


Figure 4.7: Typical low temperature (4.2 K) differential conductance (blue) and I-V characteristic (black) of a nanoparticle wire ( $R\sim 100\,\Omega$ ). The  $V_b$  is ramped up and down between  $\pm\,40\,mV$ . Note that this measurement was done on the junction shown in Figure 4.4C.

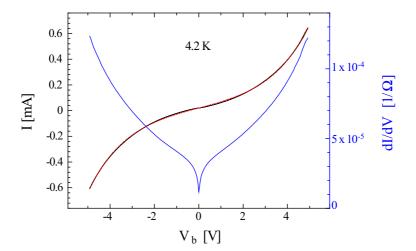


Figure 4.8: Typical low temperature  $(4.2 \,\mathrm{K})$  differential conductance (blue) and I-V characteristic (black) of a high-resistance chain. The  $V_b$  is ramped up and down between  $\pm 5 \, V$ . The dashed red curve is a Simmons' tunnelling fit (see Equation (4.1)).

except for the dip in conductance around zero bias\*, can be nicely fitted

<sup>\*</sup> Although this type of behaviour has already been observed in different Au - Au

by Simmons' expression of the tunnelling current density <sup>106</sup>:

$$J = \frac{e}{2\pi h \Delta^2} \cdot \left\{ \left( \Phi - \frac{eV_b}{2} \right) e^{-\frac{4\pi\sqrt{2m}}{h} \Delta \sqrt{\Phi - \frac{eV_b}{2}}} - \left( \Phi + \frac{eV_b}{2} \right) e^{-\frac{4\pi\sqrt{2m}}{h} \Delta \sqrt{\Phi + \frac{eV_b}{2}}} \right\} \tag{4.1}$$

with  $\Delta$  the barrier width and  $\Phi$  the barrier height. This suggests that those junctions are in the tunnelling regime (see Figure 4.8). This fit allows the estimation of the width of the barrier and the barrier height. For the former, we expected a value no larger than 1 nm, since the gap could not be seen by SEM observation. The fit gives an approximate value of 0.7 nm. This confirms that there is no real contact. The barrier height is expected to be equal to the gold work function in vacuum, known to be  $\Phi_{Au} = 5.1 \,\mathrm{eV}^{107}$ . However, since these measurements were performed in liquid helium (see Appendix C.1.3), we have to take into account the influence of adsorbed helium on the electrodes. Indeed, it was shown that surrounding helium strongly affects the work function of metals, as it polarises metal states away from the Fermi level, thus giving rise to a local decrease in the state density <sup>105</sup>. More concretely, it has the effect of strongly increasing the work function. Hence, one has rather to expect an apparent work function  $\Phi_{Au-He}$  of 9-10 eV. The fit presented here gives an approximate value of the barrier height of  $8.9 \pm 2.5 \,\mathrm{eV}$ , which is in good agreement with the work of Kolesnychenko et al 108. However, note that the value of  $\Phi$  is quite unstable in the fitting procedure, as expressed by the large error.

Furthermore, we observe a strong anomaly around zero bias voltage (ZBA), as shown in Figure 4.9\*. In this figure, the differential resistance, shifted and normalised to 1 for a bias of 2 V, is plotted as a function of the bias voltage for the two temperatures, 4.2 K and RT $^{\dagger}$ . As indicated by Figure 4.9, this anomaly depends on the temperature, as it decreases by more than 90% from 4.2 K to RT, but even at RT, a hint of the peak remains. The corresponding typical energy scale is estimated at  $\sim 100\,\mathrm{meV}$ .

Similar energy scales for nanoparticle systems have already been observed <sup>109,110</sup>, and attributed to a Coulomb blockade behaviour. In our case, it is quite likely that within the nanoparticle chain, one particle

MCBJ at low temperature, it has not been reported yet.

<sup>\*</sup> The data shown in Figure 4.8 and Figure 4.9 are issued from the same sample.

<sup>&</sup>lt;sup>†</sup> Note that the resistance at  $V_b=2\,\mathrm{V}$  is  $R(2\,V)_{LT}=19\,\mathrm{k}\Omega$  and  $R(2\,V)_{RT}=34\,\mathrm{k}\Omega$  at the respective temperatures.

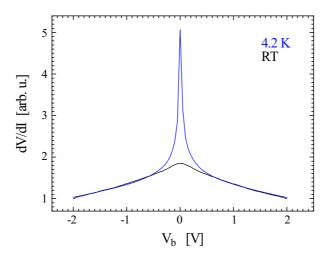


**Figure 4.9:** I-V characteristics of a high-ohmic sample (same as in Figure 4.8) at two different temperatures :  $4.2 \,\mathrm{K}$  and  $\mathrm{RT}.V_b$  is ramped between  $\pm 2 \,V$ . The zero-bias anomaly is found to decrease by 90% from LT to RT.

is isolated from the neighbouring ones, acting thus as an island for the current. Hypothesising such a configuration, and by considering the self-capacitance of one nanoparticle  $C_{self} = 4\pi\varepsilon_0\varepsilon_r r$  and the two side tunnel capacitances  $C_{tun} = \varepsilon_0\varepsilon_r A/d$ , where r is the particle radius, A the surface area and d the gap distance, we could roughly estimate the total capacitance of the junction to  $C_{tot} \approx 2 \cdot 10^{-18} \, \text{F}$ , for nanoparticles of  $\emptyset$  25 nm. This leads to a charging energy of  $E_c \sim 100 \, \text{meV}$ , in agreement to what is observed in Figure 4.9. Although this might be a bit fortuitous, it clearly suggests a Coulomb blockade behaviour. Hence, Coulomb blockade might take place at low bias voltages for this type of high-resistance chain, whereas tunneling is the dominant effect at large voltages.

#### 4.3 Concluding Remarks

We demonstrate a simple method to control the formation of metallic nanowires and chains of desired length and diameter  $^{82}$ . It is based on dielectrophoretic trapping of nanoparticles. We point out the relevance of two processes: the trapping and the subsequent anchoring of the particles between the electrodes. To trap a single chain of particles, one should apply a field of  $\sim 10^7 \, \text{V/m}$ . For our lithographically defined gaps, we typically need an ac voltage of  $\sim 1 \, \text{V}$ . Anchoring appears to proceed

in two steps: first, narrow gold connections are made by field-driven atomic surface diffusion; then, (partial) fusing of the colloids takes place. By choosing a proper series impedance, we can tune the final resistance and appearance of a junction. Lower series impedances give lower resistances and wire formation. Higher series impedances result in chains. We postulate that the driving force of the fusing process is the total surface energy. However, the process is strongly facilitated by Joule heating in the junction, resulting in a higher atomic diffusivity. We show that the homogenisation process stops, just before the dissipation in the junction reaches its maximum (determined by the series impedance). Our technique enables the preparation of nano-scale chains and wires with low resistances. Such nano-structures are promising elements in the framework of nanoelectronics. For instance, they can be used to contact nanometresize building blocks, possibly in combination with dc electromigration. Finally, we show a fast way to establish robust devices based on a few molecules, namely by trapping functionalised nanoparticles. Such junctions may have interesting applications in molecular circuit design.

## Part II TWO DIMENSIONAL SYSTEMS

2D assemblies of nanoparticles exhibit, as do 1D assemblies, very specific properties <sup>111,112</sup>, and are widely used in various fields such as electronics <sup>113</sup>, optics <sup>114</sup> and magnetism <sup>115,116</sup>. They can be fabricated by using external fields, such as electric and magnetic fields <sup>117</sup>, gravity, confining walls or shear <sup>118</sup>. This class of structures provides a view on the ensemble properties of the considered blocks or molecules, but keeps particular characteristics inherent of their well defined geometry. Hence, such assemblies lie in between the *single molecule* and the *ensemble of molecules* systems, described in the introductory part of this dissertation.

In Part II, we present an approach allowing the preparation of stable two-dimensional networks of molecular junctions <sup>119</sup>. This procedure combines self-assembly of alkanethiol-capped metallic nanoparticles <sup>120</sup> and micro-contact printing <sup>121</sup> of those monolayer self-assemblies (SAM) on various substrates. The last step consists on an in-situ molecular exchange reaction <sup>33,122</sup>, allowing the substitution of the alkane chains by dithiolated conjugated molecular wires. By such a substitution, the nanoparticle SAM turns into a two-dimensional (2D) network of molecularly linked nanoparticles. Furthermore, such a molecular place-exchange was found to be reversible, able to "switch" the network from unlinked to linked and vice versa. Significant electrical and optical evidence is presented here, confirming a proper interlinking of neighbouring nanoparticles after exchange with dithiolated molecules. Moreover, it is demonstrated here that, on one hand the fabrication of reversible 2D networks allows the characterisation of different types of molecules within the same backbone (the nanoparticle array), and on the other hand, opens new possibilities for the realisation of molecular circuits.

# 5

# COMBINING SELF-ASSEMBLY & MOLECULAR EXCHANGE FOR MOLECULAR CIRCUIT DESIGN

Regular 2D nanoparticle arrays were prepared by a method combining self-assembly and micro-contact printing. Alkanethiol-capped 10 nm gold nanoparticles\* were first self-assembled into a 2D close-packed array at the water/air interface <sup>123,124</sup> as schematically described in Figure 5.1. The assembled monolayer of colloids was then transferred to a solid substrate by micro-contact printing <sup>121,125</sup>, using a polydimethylsiloxane (PDMS) stamp with the desired imprinted structures.

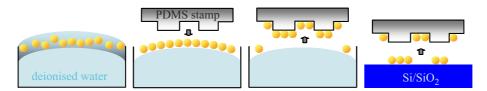


**Figure 5.1:** Schematics of the self-assembly at the water/air interface, followed by the transfer of the nanoparticle array to a substrate.

After evaporation of metallic contacts designed to address different parts of the array, molecular exchanges were performed to insert conjugated dithiolated molecules into the array. The nanoparticles forming the array become thus interlinked, acting as an interconnected molecular network. In this chapter, we elaborate on these three steps.

### 5.1 2D Self-Assembly of Metallic Nanoparticles

It was demonstrated in 1983 that organic sulfur compounds could spontaneously self-assemble on gold surfaces <sup>126</sup>. Hence, the idea arose that

<sup>\*</sup> See Appendix B.1 for their synthesis.

one could stabilise gold nanoparticles by functionalising them with thiolated molecules <sup>127,128</sup> (see Appendix A.1). The thiol packing density on nanoparticles was shown to be about twice (> 50 % ligand per surface atom) that observed on planar surfaces (33 %) <sup>129,130</sup>, as a result of the larger ligand-gold binding ratios on core edges and vertexes <sup>129\*</sup> (see Figure 5.9B). Thiol-stabilised metallic nanoparticles, also called *monolayer protected clusters* (MPCs), were shown since then to present an extraordinary stability both in solution and in the solid state <sup>130</sup>. Such thiol-capping does not only increase stability of the particles, but also allows the formation of spontaneous self-assembly of the ligand-stabilised nanoparticles on planar surfaces <sup>115,131,132,133</sup>. Indeed, the ligand shells of adjacent nanoparticles interdigitate so that the average spacing between the metal cores is less than twice the nominal thickness of the ligand shell, thus yielding a rigid particle array <sup>130,134</sup>.

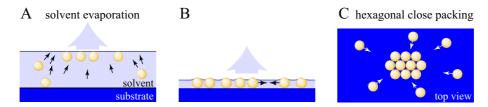


**Figure 5.2:** Schematics of the self-assembly process at the water/air interface induced by the evaporation of the solvent <sup>124</sup>.

The ordered self-assembly of gold nanoparticles is a result of a self-organisation process that occurs on the substrate or water surface <sup>124,135</sup>. Indeed, when a droplet of functionalised nanoparticles suspension is cast onto the surface of the water<sup>†</sup>, its water insolubility causes it to spread into a thin layer. As the solvent evaporates, convective flows of the solvent appear. These flows carry the particles toward the solvent surface, whereby a particle assembly arises, as schematically shown in Figure 5.2A. As the solvent becomes a thin layer with a thickness equal to the particle size, the attractive force between particles induced by the surface tension of the solvent increases significantly and causes the particles to pack together into ordered arrays, as shown in Figure 5.2B & C.

<sup>\*</sup> In our case, we approximate the number of alkanes around our nanoparticles to  $\sim 10^3$  (see Appendix B.1.3).

<sup>&</sup>lt;sup>†</sup> Because the solvent of the nanoparticle solution is water insoluble, and because alkanethiol-capped particles are hydrophobic, the solvent evaporation process on the waters surface is similar to that on a solid substrate.

In our experiment, typically  $400\,\mu{\rm l}$  of  $\sim 10^{13}\,{\rm particles/ml}$  alkanethiol-functionalised gold nanoparticles dissolved in chloroform were cast with a syringe at the water/air interface of a teflon container filled with pure, deionised water. The shape of the water surface was adjusted to be slightly convex, to provide enough pressure at the water surface\*. During the course of the solvent evaporation, initially ruby red due to the particles (Figure 5.3A), a monolayer of nanoparticles assembled, appearing suddenly as a metallic golden mirror (Figure 5.3B). Indeed, as described in the Section 7.1, the optical properties of the nanoparticles show a transition from typical insulator to metal behaviour  $^{136,137}$  while assembling, and this transition can be detected with the naked eye. The as-prepared self-assembly monolayer (SAM) of nanoparticles could then be transferred to a solid substrate by micro-contact printing method, as described in next section.

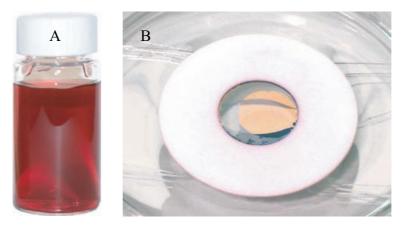
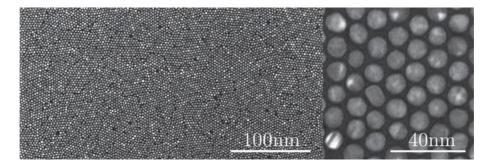


Figure 5.3: Colour transition of gold nanoparticles between: A. in solution (transparent ruby red), and B. closed-packed at the water/air interface (golden mirror).

Figure 5.4 presents transmission electron microscope (TEM) images of such arrays. Their observation reveals, apart from a certain number of defects, that the nanoparticle arrays are composed of domains of close-packed MPCs, which could extend up to about 2500 nm<sup>2</sup>. Indeed, the self-assembly process induced the formation of ordered domains of nanoparticles, subsequently compressed by the water surface pressure. Note that the dispersion of the size and the shape of gold particles also contributes to the observed particle vacancies and dislocations. High magni-

<sup>\*</sup> Note that our setup allowed no other precise control on the pressure.

fication TEM images, such as the one shown in on the right of Figure 5.4, reveal that nanoparticles are well separated from each other by the alkanethiol ligands and demonstrate the high degree of order of the particle arrangement into a hexagonal close-packed structure. Moreover, one can distinguish the faceting of the nanoparticles, suggesting that they are not spheres but rather polyhedral nanocrystals \*. Figure 5.5 also shows high-magnification TEM images of arrays constituted with different alkanethiols and their fast Fourier transformation (FFT). The FFT images reveal six clear spots, which also indicates a locally high-ordered hexagonal packing of the nanoparticles. However, for a long range, as shown in Appendix B.3.2, it can be seen from both TEM images and FFT images that the gold particles form a poly-crystalline structure over large distances, rather than a perfectly single-crystalline array.



**Figure 5.4:** TEM images of a typical nanoparticle array at low and high magnification.

The collective properties of nanoparticle assemblies are influenced to a large extent by the separation between the nanoparticles. Thus, control of the inter-particle separation leads directly to control over the properties of the assembly. In this work, the inter-particle distance was tuned by using alkanethiols chains of different lengths, as shown in Figure 5.5, where nanoparticle arrays prepared with octanethiol  $(C_8)$ , dodecanethiol  $(C_{12})$  and hexadecanethiol  $(C_{16})$  are compared. Although the respective lengths of these alkane chains are approximatively  $l_{C_8} = 1.3 \,\mathrm{nm}, \ l_{C_{12}} = 1.8 \,\mathrm{nm}$  and  $l_{C_{16}} = 2.3 \,\mathrm{nm}$ , the inter-particle distance is smaller than twice the length, due to alkanes interdigitation  $^{130,134}$ . The inter-particle distances have been determined to be  $d_{C_8} = 2.6 \pm 0.02 \,\mathrm{nm}, \ d_{C_{12}} = 2.8 \pm 0.02 \,\mathrm{nm}$ 

<sup>\*</sup> Indeed, TEM technique offers high resolution lattice imaging, as well as electronic structure of nanomaterials. Ultimately, it is used to define the shape of nanocrystals <sup>138</sup>.

and  $d_{C_{16}} = 3.0 \pm 0.02 \,\mathrm{nm}^*$ . Not only has the inter-particle distance increased, but the arrays were also found to be better ordered with longer chains. Indeed, the hexagonal symmetry is in general more accurately pronounced for  $C_{16}$ , as shown by the FFT plots. The interpenetration of the alkane chains of neighbouring particles is likely to be larger for long chains than for short ones, as suggested by the non-linear spacing with respect to the chain proper length. This makes the network more rigid and gives less freedom for particles' positioning.

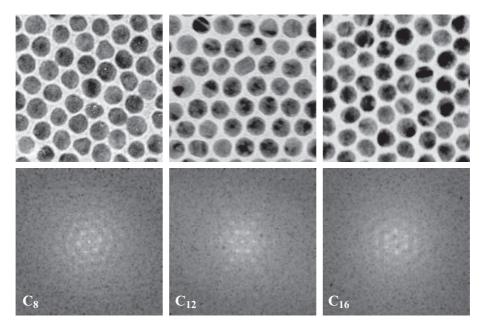


**Figure 5.5:** Comparison of TEM images of  $C_{8^-}$ ,  $C_{12^-}$  and  $C_{16^-}$  arrays (80 × 80 nm<sup>2</sup>) and their respective fast fourier transform (8 × 8 nm<sup>-2</sup>).

More generally, the possibility to make use of different alkane chains gives the remarkable advantage of tunability. This is particularly useful since one ultimately needs a breadboard which can be adapted to the further insertion of active molecules of various size.

#### 5.2 Micro-Contact Printing

SAMs of functionalised nanoparticles can be transferred onto solid substrates via an extension of the micro-contact printing method, using a

<sup>\*</sup> A full study is available in Appendix B.3.2.

smooth polydimethylsiloxane (PDMS) stamp with the desired imprinted structures  $^{121}$ . Indeed, the PDMS stamp can be prepared by using a lithographically-patterned molt, as described in details in Appendix B.3.1. For our studies, we focused on stripes of typically  $w=20-25\,\mu\mathrm{m}$  width and spaced by  $30\,\mu\mathrm{m}$ . This method implies a two-step procedure in which the SAM, playing the role of the ink, is first lifted from the water surface and then brought into conformal contact with the desired substrate\* (see Figure 5.6). Although the nanoparticle array covers the whole stamp (raised and recessed regions) after the first step, only the part situated on the raised regions gets deposited onto the substrate. Note that the substrate does not need any surface functionalisation, and may be hydrophobic or hydrophilic. Nevertheless, a cleaning procedure including Ozone treatment was performed.

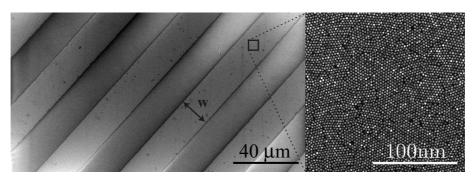


Figure 5.6: SEM images of micro-contact stamped stripes of nanoparticle array, with typical width  $w = 20 - 25 \,\mu\text{m}$  and  $30 \,\mu\text{m}$  spacing.

This method provides a good edge resolution, as demonstrated in Figure 5.7, typically of the order of 30 nm. The stamped nanoparticle arrays remain stable for several weeks in air at room temperature without showing any type of degradation<sup>†</sup>. More importantly, they can resist many common solvents, such as tetrahydrofurane (THF), ethanol, acetone or toluene.

To investigate the electrical transport through the patterned nanoparticle arrays, contact pads (5 nm Ti + 65 nm Au thick) were deposited on the top of the printed monolayer stripes using a TEM grid as a shadow mask (see Appendix B.3.3). Figure 5.8 shows SEM images of a typical sample composed of stripes of nanoparticle arrays partially covered by

<sup>\*</sup> Here, the substrates used were typically  $SiO_2/Si$  for electrical measurements and glass or  $CaF_2$  for optical measurements.

<sup>&</sup>lt;sup>†</sup> See typical degradation in Appendix B.3.5.

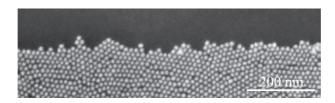


**Figure 5.7:** Edge of a typical micro-contact stamped stripe of assembled nanoparticles.

square Au contact pads. The effective array between two consecutive pads is generally composed of one or two stripes, of length  $l=10\,\mu\mathrm{m}$  and total width  $w=20-40\,\mu\mathrm{m}$ . According to SEM inspection, the arrays are kept intact, with no noticeable change of the structures observed after evaporation of the contact pads.



Figure 5.8: SEM views of the evaporated pads on top of array stripes at different magnifications. From left to right: whole sample view containing  $\approx 400$  pads, a few pads view, and a *single device*, defined as a piece of array in between 2 consecutive pads.

Remarkably, such a stamping technique followed by the pads evaporation permits the simultaneous preparation of hundreds of devices on a single sample, an essential asset for an efficient characterisation of molecular devices and future device integration.

## 5.3 THE ULTIMATE STEP: THE MOLECULAR EXCHANGE

The chemical reactivity of MPCs is determined by the functionalities present in the ligand shell and by the stability of the sulfur-gold bond at the nanoparticle-ligand interface. However, alkanethiols are neither reactive, nor conjugated, thus they exhibit no relevant electrical properties. They are used as *spacer molecules* or *reference molecules*. The introduc-

tion of functionality on particles in solution can be achieved via molecular place-exchange, as developed by Murray et al<sup>122,139</sup>. In the framework of the study presented here, the aim is to substitute alkane molecules inside the array with more attractive molecules from the electrical and optical point of view, as schematically described in Figure 5.9.

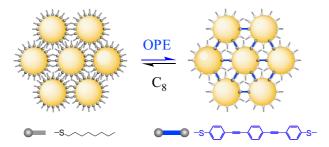


**Figure 5.9:** Schematic of the molecular exchange process between alkanethiols (disconnected array) and dithiolated *OPE*s (interconnected array).

These active molecules should be dithiolated and conjugated, and ultimately have a functionality. This approach is based on the fact that alkanethiols spontaneously exchange with excess thiolated molecules added to the functionalised nanoparticle solution, following the reaction <sup>122</sup>:

$$x(R'SH) + (RS)_m MPC \rightarrow x(RSH) + (R'S)_x(RS)_{m-x} MPC$$
 (5.1)

where x and m are the number of new active dithiolated molecules and original reference alkanethiols, respectively. The rate and equilibrium stoichiometry of this reaction are controlled in particular by the molar ratio of R'SH to RS units and R versus R' length.

Despite the large polemic on the exchange possibilities on planar surface <sup>128</sup> (position 1 in Figure 5.10), it was argued that the exchange was successful at edge and vertex sites <sup>122</sup> (position 2 and 3 in Figure 5.10). Indeed, important differences exist between monolayers on MPCs and flat surfaces: Whereas terrace sites are dominant on a flat gold surface, up to 45% of all surface sites of nanoparticles are edges and vertexes. Additionally, the high radius of curvature of MPC surfaces produces a gradient in ligand packing density, possibly leading to gauche defects <sup>140</sup>, whereas the packing density on SAM terrace is nearly uniform over the whole chain length. Another notable difference is the monolayer ordering: on MPCs, the alkanethiolate ligands are highly disordered (approaching

that of liquid alkane), whereas the methylene chains on flat SAMs are highly ordered <sup>141</sup>. Our system being an array of spherical nanoparticles, it essentially exhibits edge and vertex sites and therefore is believed to be suitable for effective exchange <sup>142</sup>. We stress that the structure of the nanoparticle array remains unchanged during the exchange process. Importantly, these exchange reactions do not depend on the existence of an equilibrium between alkanethiols bound to the particles and the free thiolated molecules, but on an associative mechanism in which the incoming molecules substitute the leaving alkanes <sup>130</sup>. Indeed, the rate of ligand exchange depends on the concentration of both entering and exiting ligands\*. Note, furthermore, that these exchange dynamics are complemented by a high mobility of the ligands on the nanoparticles' surface. This implies that MPCs with two or more types of ligands can adapt to their environment by reorganising their ligand shell <sup>143</sup>. However, note that the exchange percentage and rate not only depend on the concentration of the alkanes and incoming molecules, but also on the temperature, the pH of the solution, or the charges on the nanoparticles <sup>144,145</sup>.

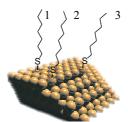


**Figure 5.10:** Schematic of the three possible sites for molecular bonds to form on nanoparticles' surface: 1. terraces, 2. edges, 3. vertices.

The molecular exchange of the alkane chains by dithiolated conjugated molecules as schematically described in Figure 5.9 was performed at room temperature under an argon atmosphere. The whole sample was immersed in a 1 mM molecular solution of oligo(phenylene-ethynylene)  $(OPE, \text{ see Appendix A.2})^{\dagger}$  in THF for 24 hours. This was followed by

<sup>\*</sup> Evidences for the associative character of the place-exchange are presented in Appendices D.3 and D.4.

 $<sup>^{\</sup>dagger}$  Note that OPE was considered as first *active molecule* for setting up the exchange method because of its simple conjugated molecular wire structure. Furthermore, it was extensively studied by several methods in the past few years, providing some bases for comparison  $^{146,147,148,149,150,151}$ .

<sup>&</sup>lt;sup>‡</sup> Note that the OPEs were in the mean time deprotected by  $H_3N$  (see Appendix B.3.4).

a  $10 \,\mathrm{min}$  rinse in THF to remove the excess materials, and finally air-blow dried. During the device immersion in the molecular solution, the *active molecules* with two anchor groups interlinked neighbouring nanoparticles, thereby forming a network of molecular junctions. Exact parameters and details on the array fabrication and molecular exchange are available in Appendix B.3.

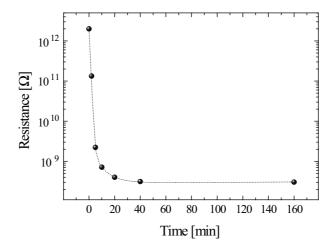


Figure 5.11: Evolution of a  $C_{12}$ -array resistance as a function of the exchange time, for a  $C_{12} \rightarrow OPE$  exchange at 26°C.

To understand and thus better control the process underlying this molecular exchange, a study of the electrical resistance as a function of the immersion time has been performed  $^{152}$ . The resistance of the device was taken as representative for the exchange evolution and recorded as a function of the time during the whole process. The resistance decreased rapidly in the first hour and then saturated, as shown in Figure 5.11. This is consistent with the results of Murray  $et\ al\ ^{122}$ , who determined the rate of place-exchange on monolayer protected clusters, and with the recent observations of Lennox  $^{142}$ . However, though the exchange process seems to be merely finished after a few hours, the alkane chains are not 100% replaced by the  $active\ molecules$ , as was also observed by Murray  $et\ al$ . This is particularly clear on the infrared (IR) spectra, presented in Chapter 7. It strongly suggests that the mechanism involved here is limited by a threshold, upon which the system does not evolve any more, thus exhibiting a saturated behaviour.

To analyse this in more detail, one should relate the conductance to the molecular exchange and bridging. At t = 0, the conductance of a

device is determined by tunneling through the alkanethiols. When the array is immersed in the molecular solution, the place-exchange process starts: alkanethiols are replaced by OPE molecules at random sites in the array. Some of these molecules are able to bridge the gap between two neighbouring nanoparticles. Thus, molecular junctions are formed with a much higher conductance than before immersion. Nevertheless, the conductance of the entire device does not increase much initially, since the alkanethiol junctions still dominate the conductance of the network. After a characteristic time  $\tau_p$ , a continuous path of OPE junctions is formed across the whole array, thereby bridging the two micro-fabricated contacts. Consequently, a dramatic drop of the resistance occurs. In a percolative model<sup>153</sup>, this stage corresponds to the formation of the first percolation path. By considering p(t) as the normalised number of bonds formed as a function of time, one defines the percolation threshold as  $p_c = p(\tau_p)$ . Note that for 2D hexagonal networks, the percolation threshold is  $p_c = 2\sin(\pi/18) = 35\%$ . Then, more and more paths are formed as the exchange process continues and the conductance increases, till it reaches a saturation point, where additional parallel paths do not significantly change any more the conductance.

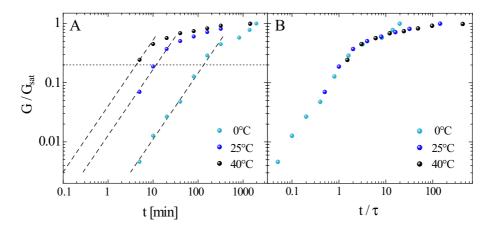
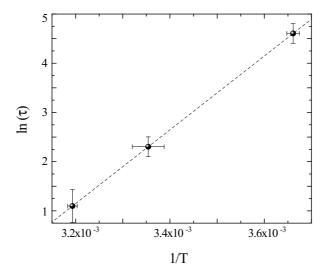


Figure 5.12: A. Evolution of the normalised conductance ( $C_8$ -array) as a function of the OPE-exchange time, at different temperatures : 0°C, 25°C and 40°C. B. Normalised conductance versus normalised time  $t/\tau$ . The three curves superpose, for  $\tau(0^{\circ}C) = 100 \,\mathrm{min}$ ,  $\tau(25^{\circ}C) = 10 \,\mathrm{min}$  and  $\tau(40^{\circ}C) = 3 \,\mathrm{min}$ .

The percolation character of the place-exchange process in the nanoparticle arrays was further investigated by varying the temperature of the exchange and comparing its behaviour as a function of time. Figure 5.12A shows the normalised conductance of arrays  $G/G_{sat}$  as a function of time (from 5 minutes to 1 day) for the exchange process at 0°C, 25°C and 40°C\*. For all devices, the conductance curve increases rapidly at first, until finally flattening off. Upon inspection, we clearly observe a temperature dependence of the conductance: the higher the temperature, the faster the conductance increases. Remarkably, we observe a strong similarity between the three curves<sup>†</sup>. This suggests that the dominant mechanism is the same in all cases. To test this hypothesis, the time was normalised by  $\tau = a \cdot \tau_p$ , with a chosen for the three curves at the arbitrary conductance value  $G/G_{sat} = 0.2$ . Figure 5.12B displays  $G/G_{sat}$  as a function of  $t/\tau$  (log-log scale), with  $\tau(0^{\circ}C) = 100 \, \text{min}$ ,  $\tau(25^{\circ}C) = 10 \, \text{min}$  and  $\tau(40^{\circ}C) = 3 \, \text{min}$ , deduced from Figure 5.12A. One sees that the



**Figure 5.13:** Arrhenius plot of the characteristic times corresponding to the three different temperatures measurements.

three curves overlap onto a 'universal' curve, thus confirming that the dominant mechanism underlying the place-exchange is temperature independent. From this, it follows that the temperature dependence in Figure 5.12A is related to the kinetics of exchange and bridging only.

<sup>\*</sup> Each of these three sets of points is the average of about 10 measurement curves, initially normalised by their saturation values.

 $<sup>^{\</sup>dagger}$  Note that the process is well observable at  $0^{\circ}$ C, as it is slowed down enough to be extensively measured, whereas much less data points could be taken at higher temperature due to the faster reaction.

Figure 5.13 displays an Arrhenius plot of  $\tau$ , based on the assumption of a Boltzmann's type scaling law for the percolation time threshold:

$$\tau_p \propto e^{\frac{E_a}{k_B T}} \tag{5.2}$$

with  $E_a$  the activation energy\*. According to this result, one can suggest that the exchange kinetics is dominated by an activated process with a diffusion barrier of  $E_a = 0.64 \pm 0.06 \,\mathrm{eV}$ . As this barrier appears too high to reflect the diffusion of the molecules in the solution  $(D_{sol} = \frac{k_B T}{6\pi R \eta})$ , it is more likely to reflect their diffusion on the nanoparticles' surface.

We conclude from the above that the evolution of the conductance during exchange is determined by two processes: the kinetics of exchange and bridging, a temperature dependent diffusive process, and the percolation process, which is temperature independent <sup>152</sup>. To elucidate in more details these two processes, additional experiments and modelings are currently in progress.

#### 5.4 Concluding Remarks

The high mechanical and chemical stability of the nanoparticle arrays presented here enable us to use them as "nanoparticle breadboards" to fabricate networks of molecularly linked nanoparticle junctions <sup>119,152</sup>. In contrast to other approaches for the preparation of interlinked particle arrays, such as layer-by-layer assembly <sup>154</sup>, Langumir-Blodgett technique <sup>133</sup>, and multiple deposition on solid substrates <sup>33,155</sup>, the stamping technique yields spatially well positioned arrays, totally free of multilayer regions. This technique, combined with shadow-mask evaporation, enables the direct fabrication of hundreds of junctions on one single chip, a prerequisite for future circuit implementation. The molecular exchange on the assembled nanoparticle, which exhibits activated behaviour, brings the final touch by allowing a molecular interconnection of the particles within the arrays.

<sup>\*</sup> Note that  $ln(\tau) = ln(a\tau_p) = C + \frac{E_a}{k_B T}$ .

# 6

## ELECTRICAL TRANSPORT IN 2D NANOPARTICLE ASSEMBLIES

We discussed in the previous chapter a method to fabricate 2D nanoparticle arrays and how to convert them into molecular networks via a place-exchange process. Here, we make use of this method to investigate the electrical transport through disconnected and connected arrays, to prove the robustness of these systems and carry out investigations on selected molecules.

## 6.1 Electrical Transport through 2D Arrays

The first investigations of electrical transport through nanoparticle arrays were performed with OPE as active molecules, in arrays made of  $C_8$ -functionalised nanoparticles\*. The OPE molecular wire was chosen for its simple conjugated structure. Furthermore, it has been investigated by different techniques in the last few years  $^{146,147,148,149,150,151}$ , allowing easy comparison for our study.  $C_8$  were used as the most appropriate spacer molecules to get an interparticle spacing  $(d_{C_8} = 2.6 \pm 1.4 \,\mathrm{nm}^{\dagger})$  fitting to the OPEs  $(l_{OPE} = 2.02 \,\mathrm{nm})$ .

We know from the molecular exchange study that the exchange is fast at the beginning and then saturates, typically after one hour. For the transport measurements, we performed 24 hours-long exchanges to ensure the completion of the process. We focused then only on the initial resistance of the arrays (disconnected) and on the final resistance (connected), the latter being taken as a characteristic of the *OPE* molecules.

<sup>\*</sup> The measurement setup details are shown in Appendix C.2.

 $<sup>^{\</sup>dagger}$  Note that 1.4 nm is not the error but the standard deviation, meaning that in most of the cases the inter-particles distance stands in between 1.2 – 4 nm. These values were estimated from TEM images (see Figure 5.5). Hence, a large amount of sites is expected to have a spacing of about 2 nm, suitable for the OPE insertion.

Since the arrays size could differ from one to another, we considered the sheet electrical resistance  $R_{\square} = R \cdot \text{w/l}$ , calculated as a spatial normalisation of the measured resistance R. The sheet resistance was thus used in this chapter to compare various arrays. The resistance of the arrays was measured with a needle prober in a simple 2-point measurement, at room temperature. A ramping bias voltage, up to a maximum of 1 V, was applied to the arrays, yielding a maximum voltage drop over one molecular junction, namely between two neighbouring nanoparticles, of  $\sim 1 \,\text{mV}$ , since the array is formed by about one thousand junctions in series. The potential energy is therefore much lower than the thermal energy  $k_B T$ , amounting to 26 meV at room temperature, and ensures a linear response of the arrays. In addition, the single electron charging energy of individual nanoparticles is estimated\* to be smaller than  $k_B T$ .

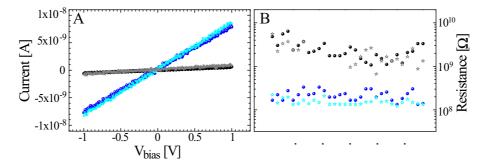


Figure 6.1: A. Electrical I-V characteristic at room temperature of one device, for the four steps of the exchange sequence  $C_8$  (black dots)  $\to OPE$  (blue dots)  $\to C_8$  (gray stars)  $\to OPE$  (light blue stars). B. Resistance of several devices on one chip for the same sequence.

Figure 6.1A shows the typical I-V characteristics of a  $C_8$ -array, firstly as-prepared (black dots) and secondly after OPE-exchange (blue dots). From first to second measurement, a large increase of the current passing through the array is observed, representative of a decrease of the resistance of more than one order of magnitude ( $R_{\square C_8} = 1.9 \cdot 10^9 \,\Omega$  to  $R_{\square OPE} = 1.3 \cdot 10^8 \,\Omega$ ). We attribute this significant resistance decrease to two effects: first, the formation of interlinked molecular junctions by the dithiolated OPE molecules, and second, the conjugation character of OPEs, making them better electron carriers than alkanethiols. The typical values of the array resistance as-prepared and OPE-exchanged

<sup>\*</sup> A rough estimation of the charging energy  $E_C = e^2/2C$  in our hexagonal close-packed geometry gives  $E_C \approx 6 \,\mathrm{meV}$ .

are  $1-100\,\mathrm{G}\Omega$  and  $100\,\mathrm{M}\Omega$  respectively. As shown later on, these values may be compared to the resistance of a single molecule, and can thus lead to the approximation of the number of molecules involved in a single molecular junction.

We also demonstrate in Figure 6.1A that it is possible to make a back-exchange to  $C_8$ , via a second exchange procedure\* (grey stars). The resistance of the array increases to a value of  $R_{\Box C_8} = 1.5 \cdot 10^9 \,\Omega$ , very similar to its initial value, as the I-V curve superposes well with the asprepared one. This indicates that OPE molecules have been successfully replaced by  $C_8$ , suggesting the possibility to use arrays for several subsequent studies on different molecules. In a last step, we re-exchanged with OPEs, and the resistance drops down to  $R_{\Box OPE} = 1.2 \cdot 10^8 \,\Omega$ , very near to the previously observed OPE resistance (light blue stars). This demonstrates the full reversibility of the place-exchange process, by successive exchanges between  $C_8$  and OPE molecules. Note that we checked the non-etching behaviour of the leaving molecules during exchange, which is crucial for reversibility (see Appendix D.4).

Figure 6.1B displays the spread of resistance values of the  $C_8 \rightarrow OPE \rightarrow C_8 \rightarrow OPE$  sequence of exchanges for several arrays of a chip-sample<sup>†</sup>. Although one observes some scattering of the respective  $C_8$  and OPE resistances, these data show the high yield and the very good reproducibility of the reversible formation of molecular junctions. However, we point out that although the reproducibility on one sample is demonstrated, the resistances and the decrease between the two  $C_8$  and OPE resistances vary from sample to sample. More generally, the molecular place-exchange from  $C_8$  to OPE exhibited a decrease in resistance of one to three orders of magnitude<sup>‡</sup>. We attribute the chip-to-chip resistance differences of the as-prepared devices to variations in the average inter-particle distance. Different surface pressures during the arrays self-assembly at the water/air interface can lead to this effect, as also observed by Heath  $et\ al^{156}$ .

To some extent, one would like to extract from such measurements an approximate value of the resistance of one *single junction*, namely the resistance between two neighbouring nanoparticles. We may model the nanoparticle array as a hexagonal network of nodes interconnected by identical classical resistors  $R_J$ , as shown in Figure 6.2. The relation

<sup>\*</sup> The array was immersed for 24 h in a 0.1 M  $C_8$  solution in THF, followed by a 24 h immersion in a pure  $C_8$  solution.

<sup>&</sup>lt;sup>†</sup> See the chip-sample configuration in Figure 5.8

<sup>&</sup>lt;sup>‡</sup> See the full set of measurements in Appendix E.2, Table E.2.

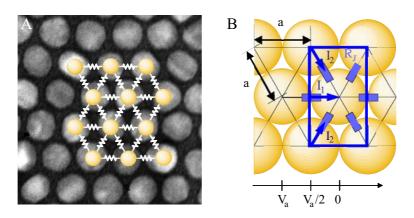


Figure 6.2: A. SEM image of a nanoparticle array modeled with a hexagonal network of nodes interconnected by identical classical resistors  $R_J$ . B. The inter-particle resistance  $R_J$  can be deduced as a function of the sheet resistance  $R_{\square}$  by considering the current flowing through a unit cell.

between the sheet resistance of the network  $R_{\square}$  and the single junction resistance  $R_J$  can be deduced from a simple consideration of the current passing through a unit cell of length l=a and width  $w=\sqrt{3}a$ , when a voltage  $V_a$  is applied between this cell and the previous cell (Figure 6.2B). The incoming total current through the cell is  $I_a=I_1+2I_2=2V_a/R_J$  and thus the sheet resistance  $R_{\square}=\frac{V_a}{I_a}\cdot\frac{w}{l}=\frac{\sqrt{3}}{2}R_J$ . The average resistance of a junction formed by two OPE-interlinked nanoparticles corresponds therefore to an estimate value of  $\sim 100\,\mathrm{M}\Omega$ . Recent STM experiments have provided a value of  $77\,\mathrm{M}\Omega$  for the resistance of a single OPE molecule  $^{151}$ , which is very close to the junction resistance in the present work\*. Let's mention that recent measurements in our lab with a break junction system also revealed a typical single OPE resistance of  $100\,\mathrm{M}\Omega^{157}$ . This finding translates to an average of  $\sim 1\,OPE$  molecule per single junction in our arrays. Therefore, one can conclude that the self-adjustability favours the self-formation of single molecular junctions.

Let's keep in mind however that this study cannot intrinsically lead to an accurate value of the single junction's resistance, but only an order of magnitude. Indeed, such a method gives information averaged over a

<sup>\*</sup> Note that strongly varying values of the OPE resistance have been given in the past  $^{146,147,148,149,150}.$ 

large number of junctions. As some junctions might be well contacted, some others may be badly or even not contacted due, for example, to inappropriate inter-particle distance\*. Indeed, the observed conductance is dominantly the result of the well contacted junctions, but is averaged over the total number of junctions. The real conductance of a single junction is then underestimated. As the proportions between the well contacted junctions and the badly contacted junctions are unknown, one must remain wary of the interpretation of these results. Furthermore, the conductance superposition laws of molecules connected in parallel are not necessarily linear <sup>53,158</sup>.

## 6.2 On Course to understand the Nanoparticle-Molecule Assembly

The OPE exchange was further investigated in  $C_{12}$ - and  $C_{16}$ -functionalised nanoparticle arrays (see Appendix A.1 for  $C_{12}$  and  $C_{16}$ ). Although the length of this molecule (2.02 nm) makes a  $C_8$  array appear to be the most suitable in terms of inter-particle spacing<sup>†</sup>, we were interested to see how the exchange and final resistance would depend on the inter-particle spacing ( $d_{C_{12}} = 2.8 \pm 1.4 \,\mathrm{nm}$  and  $d_{C_{16}} = 3.0 \pm 1.4 \,\mathrm{nm}$ ). In the  $C_{12}$ - and even more so in the  $C_{16}$ -arrays, the spacing is such that the molecules are less likely to bind on both sides (Figure 6.5), and thus form a covalently-bonded network. Higher resistances for both the initial (disconnected) and OPE-exchanged (connected) stages of the arrays are expected, with respect to the resistances observed with the  $C_8$ -arrays. Figure 6.3 shows statistics on the typical resistances exhibited in the three cases<sup>‡</sup>.

Firstly, one might compare the initial resistances for the three types of array:  $C_{8^-}$ ,  $C_{12^-}$  and  $C_{16^-}$  arrays. As the nanoparticles are disconnected and their surroundings are only composed of non-conjugated molecules, we expect a tunnelling behaviour of the electrons in between each neighbouring nanoparticle. Hence, according to Equation (2.7), the resistance should exponentially increase with the inter-particle distance. The data confirms that the resistance increases for increasing nanoparticle spacing, concretely  $R_{\square C_8} \sim 10^{11} \,\Omega$ ,  $R_{\square C_{12}} \sim 10^{12} \,\Omega$  and  $R_{\square C_{16}} \sim 10^{13} \,\Omega$ . These

<sup>\*</sup> See the percolation discussion in Section 5.3.

 $<sup>^{\</sup>dagger}$  Note that concerning the contacting of OPEs in the array, the variation of interparticle spacing is relevant  $(1.4 \,\mathrm{nm})$ , not the error on the mean value  $(0.02 \,\mathrm{nm})$ .

 $<sup>^{\</sup>ddagger}$  Note that because of the high resistances considered, all measurements were performed in this study at a fixed voltage of 25 V.

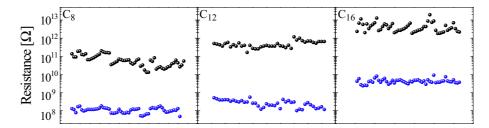


**Figure 6.3:** Resistance of several junctions of  $C_{8^-}$ ,  $C_{12^-}$  and  $C_{16^-}$  arrays as-prepared (black) and after OPE-exchange (blue), measured with a voltage of  $V=25\,\mathrm{V}$ . See also Table E.2.

values follow a trend which is in good agreement with theoretical calculations <sup>159</sup>. Moreover, they indeed follow an exponential behaviour, as shown in Figure 6.4, where the three distance values correspond to the  $C_8$ -,  $C_{12}$ - and  $C_{16}$ -arrays. From such a graph, we can extract transport parameters, such as the tunnelling decay coefficient  $\beta$  of alkanes in our system. Indeed, as  $\beta = \frac{2}{\hbar}\sqrt{2m\Phi}$  (see Equation (2.7)), it is therefore the slope of the linear curve -ln(I) versus d. We find  $\beta = 1.04 \pm 0.05 \,\text{Å}^{-1}$ , in good quantitative agreement with theoretical and experimental data previously reported <sup>134,159,160,161,162</sup>. Note that  $\beta$  is voltage-independent at such a low voltage ( $\sim 25 \, \text{mV}$ ) <sup>163</sup>, and also independent of the number of molecules in the contact region and the lead geometry <sup>159</sup>.

If we consider now the respective resistances after the *OPE*-exchange, we observe a similar general trend for  $C_{12}$ - and  $C_{16}$ -arrays as for  $C_{8}$ arrays, that is to say, the resistance dropped down by several orders of magnitude. However, whereas the  $C_8$ -arrays resistance decreases by one to three orders of magnitude,  $C_{12}$ - and  $C_{16}$ -arrays decrease by four orders of magnitudes. In other words, if we compare the final resistances,  $R_{\Box OPE(C_8)} \approx 1.1 \cdot 10^8 \,\Omega, \, R_{\Box OPE(C_{12})} \approx 2.7 \cdot 10^8 \,\Omega \text{ and } R_{\Box OPE(C_{16})} \approx 4.3 \cdot 10^8 \,\Omega$  $10^9 \,\Omega$ , we observe that the  $C_{12}$ -arrays final resistance is of the same order of magnitude as  $C_8$ -arrays final resistance, whereas the  $C_{16}$ -arrays final resistance is one order larger. Since exchange rates for  $C_{8}$ -,  $C_{12}$ - and  $C_{16}$ functionalised nanoparticles are expected to be similar <sup>122</sup>, we consider that there is, on average, the same number of OPE molecules inside the three types of array. Hence, we base our analysis on the inter-particle spacing difference only. First note that in the three cases, the average inter-particle distance ( $d_{C_8}=2.6\,\mathrm{nm},\ d_{C_{12}}=2.8\,\mathrm{nm}$  and  $d_{C_{16}}=3.0\,\mathrm{nm}$ ) is larger than the OPE molecule ( $l_{OPE} = 2.0 \,\mathrm{nm}$ ). Furthermore, this spacing is not constant, but varies from one site to another, as given by

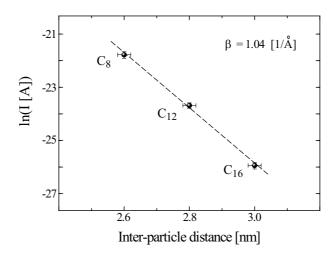


**Figure 6.4:** Natural logarithm of the current passing through the array ln(I) as a function of the inter-particle distance ( $d_{C_8} = 2.6$ ,  $d_{C_{12}} = 2.8$  and  $d_{C_{16}} = 3.0 \pm 0.02 \,\mathrm{nm}$ , from TEM). The slope (opposite) gives directly the value of the tunnelling decay coefficient  $\beta$ .

the standard deviation\*. Hence, in most sites, the molecules may not inter-connect neighbouring particles, and various transport mechanisms may take place (see review of Salomon  $et\ al^{161}$ ).

We consider different paths for the current to flow from one nanoparticle to the other. In Figure 6.5A, different paths are proposed: in (i), the inter-particle distance is such that the molecule binds on both sides. As the molecule is fully conjugated, it constitutes a current path (direct) of relatively low resistance. In the case of a slightly larger gap (ii), the current flows in two steps, combining the flow through the molecule and the tunneling through air on the remaining distance <sup>164</sup>. This implies a larger resistance of the overall path (indirect) between one nanoparticle to the next one. If the inter-particle distance is even larger (iii), facing molecules attached on both particles may undergo a  $\pi$ - $\pi$  stacking, thus opening a new current path (direct), much more favourable than tunneling. Indeed, it has been demonstrated that in the case of a proper  $\pi$ - $\pi$ stacking, the  $\pi$ -orbitals overlap, resulting in a resistance corresponding to a fully conjugated equivalent system <sup>165,166</sup>. Although these different paths exist in the three cases,  $C_8$ ,  $C_{12}$  and  $C_{16}$ , their proportions may strongly vary. Figure 6.5B shows the spacing distribution in the case of a

 $<sup>^{*}</sup>$  The determination of the spacings and standard deviations is presented in Appendix B.3.2.

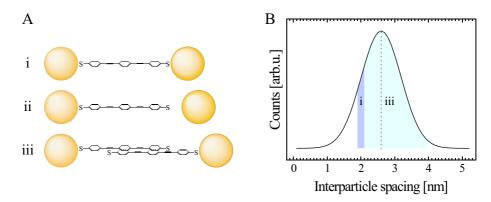


**Figure 6.5:** A. Schematics of the hypothetical molecule position with respect to the particles within the arrays: i. The molecule binds on both sides; ii. The spacing is slightly larger than the molecule; iii. The spacing is much larger, and allows  $\pi$ - $\pi$  stacking of facing molecules. B. Representation of the inter-particle spacing distribution for a  $C_8$ -array ( $d_{C_8} = 2.6 \pm 1.4 \,\mathrm{nm}$ ). The small region around 2 nm corresponds to case (i); the large region corresponds to both cases (ii) and (iii).

 $C_8$ -array. The delimitated zones corresponding to the different paths are schematically represented. Whereas the gaussian curve moves to the right (larger spacing) for  $C_{12}$  and  $C_{16}$ , these zones remain at the same position, yielding in a decrease of the total paths number. In a percolation view, as described in Section 5.3, less paths for the current to flow yield a larger final resistance. Moreover, the indirect paths involve tunneling over larger distances, yielding in an exponential decay of the current. Typically, this could explain the non-exponential increase of the OPE-exchanged array resistance versus the spacing increase, going from  $C_8$ - to  $C_{12}$ - and  $C_{16}$ -case. However, the determination of the exact contributions of the paths (i), (ii) and (iii) in the three cases  $C_8$ ,  $C_{12}$  and  $C_{16}$  is hardly achievable with only three different spacings, and thus is beyond the scope of this chapter.

#### 6.3 How about Another Molecular Wire?

In the Section 6.1, we proposed two reasons for the resistance drop occurring after the molecular exchange with OPE: first the nanoparticle array gets interlinked thanks to the two thiol groups, and second the insulating alkanes are replaced by conjugated molecules. Furthermore, we discussed in Chapter 2 about the strong influence of the metal/molecule

contacts on the junction's resistance. Depending on the quality of the coupling between the lead and the molecule, the resistance of the system may mainly issue from the contacts' resistance. Hence, the question one might ask is: "In our geometry, is there any influence of the molecule core on the final resistance?". To answer this question, we propose to study a slightly different molecule, OPV, in the same way as for OPE. This molecule also has S- binding groups, has approximately the same length\* ( $l_{OPV} = 1.98 \, \text{nm}$ ,  $l_{OPE} = 2.02 \, \text{nm}^{\dagger}$ ), and has, in contrast, double bonds instead of triple bonds in between the aromatic rings (see ball & stick schematics in Appendix A.3).

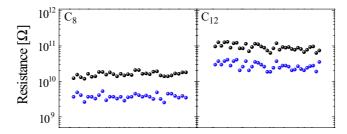


**Figure 6.6:** Resistance of several junctions of  $C_8$ - and  $C_{12}$ -arrays, asprepared (black) and after OPV-exchange (blue). See also Table E.3.

Figure 6.6 presents resistance measurements of arrays, as-prepared and after OPV-exchange, in the same fashion as for the OPE-exchanges presented above. One notices immediately that the behaviour is comparable, suggesting that the molecular exchange is possible with different molecular wires. However, the resistance drop is much less than with OPE: whereas the drop was of 1-3 orders of magnitude for OPE, it is only a factor of 3-4 for OPV, both in  $C_8$ - and  $C_{12}$ -arrays. This suggests that OPVs are less conducting than OPEs. Indeed, the resistance of OPV in a  $C_8$ -nanoparticle array was found to be  $\sim 10^9 \,\Omega$ , and  $\sim 10^{10} \,\Omega$  in  $C_{12}$ -arrays. This result is about one order of magnitude larger than observed with crossed-wire junctions  $^{146}$  or STM  $^{148}$ . Furthermore, the OPV was claimed in the recent years to be a better conductor than  $OPE^{146,148,149,167}$ . Indeed, in the relaxed state (coplanar), it presents a better coupling in between its aromatic and double bond units, as compared to OPE between its aromatic rings and triple bond units. This

<sup>\*</sup> We assume here that a difference of 0.02 nm between the two molecules' lengths is negligible as compared to the inter-particle spacing ( $d_{C_8} = 2.6 \pm 1.4 \,\mathrm{nm}$ ), and that it has no effect on the contacting behaviour.

<sup>&</sup>lt;sup>†</sup> These lengths were calculated via a mm2 procedure.

makes OPV's overall conjugation better than OPE's, and in consequence, OPV's HOMO-LUMO gap is smaller relative to OPE's  $^{167}$ .

However, this is only true when assuming that both molecules are relaxed and keep their coplanarity. This assumption does not always hold in the reality. Indeed, it was theoretically demonstrated that whereas at low temperature (typically below 30 K), the rings show very little tendency to rotate, above 30 K, the rings are able to freely rotate with respect to each other  $^{168}$ . Note that at room temperature, OPE molecules attached to gold can rotate at a frequency as high as  $390\,\mathrm{GHz}^{169}$ . The rotational barrier for the aromatic rings is known to be of about  $18\,\mathrm{meV}$  for a  $45^\circ$  rotation and about  $37\,\mathrm{meV}$  for  $90^\circ$   $^{168}$ .

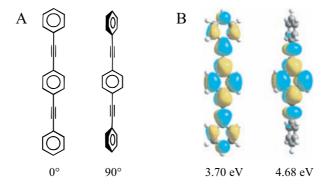


**Figure 6.7:** Conformation study of the OPE molecule <sup>170</sup>. A. Schematics of planar OPE (0°) and with a 90° torsion angle. B. Corresponding charge density plots (LUMO) for the optimised geometries at the B3PW91/6- 31G\* level of theory. The HOMO-LUMO gap are 3.70 eV (0°) and 4.68 eV (90°).

A good conjugation is generally observed when the  $\pi$ -orbitals of the molecule overlap. In the case of OPE, this is the case when the three aromatic rings remain in a planar configuration. The conjugation is (partially) broken when a ring makes a non-zero angle with respect to the following ring <sup>41</sup>. Figure 6.7 presents a study of possible conformal states of  $OPE^{170}$ . Charge density plots\* are presented for two cases: planar (0°) and with a torsion angle between the central rings and the other rings of 90°. One can see that the HOMO-LUMO gap for the 90°-rotated case (4.68 eV) is larger than the planar case (3.70 eV). Indeed, whereas the orbitals are well delocalised on the full molecule for the planar case, they are localised on the centre ring for the 90°-rotated, due to the broken

 $<sup>^{\</sup>ast}$  LUMO, optimised geometries at the B3PW91/6-  $31G^{\ast}$  level of theory.

conjugation, thus providing bad coupling to the leads. However, at sufficient temperature the molecule spontaneously rotate, thus undergoing all possible conformations. Hence, its conductance is an average over all conformal states.

In the case of a SAM, molecules interact with each other. It was demonstrated that two neighbouring aromatic ring-based molecules are likely to have their rings standing perpendicular to each other <sup>168</sup>. At high temperature, the rings are able to rotate, thereby allowing them to frequently approach the planar geometry.

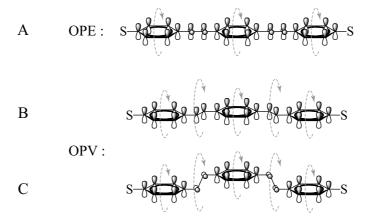


**Figure 6.8:** 3D schematics of the *OPE* (A) and *OPV* (B & C) molecules, including their electronic orbitals. *OPE* keeps its linearity upon rotation of the rings. *OPV* is non-linear and can have a broken conjugation even with all rings parallel (C).

Regarding this, let us compare the OPE and OPV cases. It is known that the packing of the molecule SAM strongly affects the rotation frequency  $^{169}$ . In our arrays, the packing is supposed to be similar for OPE and OPV. However, whereas OPE, upon rotation, keeps its backbone's linearity (Figure 6.8A), OPV undergoes non-linear backbone configurations (Figure 6.8B & C). Thus, the rotation of OPV needs more room in the direct vicinity, as compared to OPE. Furthermore, changes in the OPV configurations might induce length variations of the molecule (Figure 6.9A & B). This can also limit the rotation of the molecule. In consequence, it is likely that in certain circumstances, OPVs may have a reduced ability to properly rotate, thus seldom reaching coplanarity. Our respective resistance observations for OPE and OPV could be explained by such a partial freezing of the conformal state of the OPV molecules,

reducing their chance to undergo  $\pi - \pi$  interactions. In contrast, OPEs can rotate freely, ensuring frequent coplanarity.

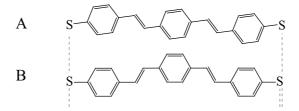


**Figure 6.9:** Schematics of the two possible planar configurations of the OPV: A. long  $l_{OPV}=1.98\,\mathrm{nm}$ , B. short  $l_{OPV}=1.97$  (from mm2 calculations).

To conclude, in a complex system with environmental constraints such as our nanoparticle arrays, OPV molecules are likely to rotate with more difficulty and thus to appear more insulating than OPEs. Although there is no compelling evidence in favour of the this hypothesis yet, it would explain the relative high resistance observed in the OPV-exchanged arrays, as compared to OPE-arrays. In any case, this result also confirms that the molecules themselves, not only their contacts with the nanoparticles, play an important role on the electron transport in our nanoparticle array geometry.

#### 6.4 Concluding Remarks

The reversibility and flexibility of molecularly connected or disconnected nanoparticle networks makes them a valuable platform for electrical transport studies and development of molecular electronic circuits.

The electrical transport of a specific molecule was investigated within different types of arrays, namely  $C_{8}$ -  $C_{12}$ - and  $C_{16}$ -arrays, as well as the electrical transport of different molecules within the same types of arrays, namely oligo(phenylene-ethynylene) (OPE) and oligo(phenylene-vynylene) (OPV). Those two molecular wires have proven the feasibility of such a method of investigation. More complex molecules, such as photochromic molecules, are currently under investigation.

Ultimately, this system provides us with the possibility to sequentially exchange and measure different molecules within the same nanoparticle array. In a more technological fashion, it enables us to envision the realisation of more complex networks, for instance by inserting different functional molecules at specific sites.



# OPTICAL CHARACTERISATION OF 2D NANOPARTICLE ASSEMBLIES

As introduced in Chapter 2, organic molecules as well as noble metal nanoparticles interact with light, resulting in specific absorptions. While molecules can have their vibrational states excited in the IR region, or experience electronic excitations in the visible, UV and X-ray regions, nanoparticles exhibit localised surface plasmon resonances at visible wavelengths. Optical investigations can thus lead to the detection of specific components in a heterogeneous sample  $^{171}$ , in our case alkanes and OPEs in the nanoparticle arrays. They also give information on the physical properties of the investigated structures. In this chapter, we develop the investigation of the nanoparticle arrays, molecularly connected or not, via visible spectroscopy, infrared spectroscopy and X-ray photoelectron spectroscopy\*.

## 7.1 Surface Plasmon Resonance : An indicator for Molecular Exchange

Whereas the absorption of OPE in the UV-visible range is situated around  $300-400\,\mathrm{nm}^\dagger$ , gold nanoparticles typically have their surface plasmon resonance (SPR) around  $500\,\mathrm{nm}^{172}$ . However, the former being much weaker than the latter, we only detect the SPR of the nanoparticles when considering the nanoparticle arrays. This does not mean that the molecules do not contribute to the optical response. Indeed, as introduced in Section 2.2.2, the SPR is influenced by several parameters  $^{173}$ :

<sup>\*</sup> Both visible and IR measurements have been carried out in collaboration with Y. Kamdzhilov, Chemistry Department, University of Basel. XPS measurements were carried out by P. Morf at the Paul Scherrer Institute, Villigen.

 $<sup>^\</sup>dagger$  See Figure A.6B in the Appendices. Note that the alkanes do not exhibit absorption in the UV-visible range.

the particle size  $^{174,175}$ , shape  $^{176}$  and spacing  $^{175}$ , but also by the surrounding medium permittivity  $^{177,178}$ . In particular, a surrounding medium of larger permittivity is expected to lead to a shift of the SPR towards the larger wavelengths. The aim of this study is to elucidate the exchange process by investigating the position of the surface plasmon resonance peak for the three stages: as-prepared, after OPE-exchange and after  $C_n$ -back-exchange.

Initially, we performed an analysis on the particle-particle interaction. The nanoparticles, when near to each other, interact and influence the surface plasmon, shifting the resonance to longer wavelengths (red shift). In order to evaluate this interaction in the geometry concerned, namely the nanoparticle arrays, we investigated the optical absorption of  $C_{16}$ -capped nanoparticles, dispersed in diluted chloroform solution on the one hand, and self-assembled into a monolayer array on the other\*. Figure 7.1A shows the comparison of the two systems, where absorbance spectra have been recorded between 200 nm and 1000 nm.

On the spectrum of the particles in solution (blue curve), we observe an SPR at 528 nm, in good agreement with the red colour of the solution (Figure 5.3A) and with Mie theory expectations. However, the array system (black curve) experienced a dramatic red shift of the SPR, arising at 583 nm. This is the manifestation of what was observed, in term of colours, during the self-assembly (Section 5.1). Indeed, the colour was found to change while the particles were packing, ultimately reaching a shiny golden colour (Figure 5.3B). The red shift of the SPR observed here, induced by increasing particle-particle interaction<sup>†</sup>, is responsible for this colour change. The general Mie solution (Relations (2.15)), as well as the dipolar approximation (Equation (2.16)), only hold as long as there is no interaction between the particles, the total extinction being the sum of each particle's contribution. This is the reason why the solution response is in agreement with this theory<sup>‡</sup>, whereas the array response is not (red shift).

Figure 7.1B displays fits of these spectra according to Equation  $(2.16)^{\S}$ ,

<sup>\*</sup> Note that the arrays fabricated for this study were not patterned as for electrical measurements, but were simple continuous films of about  $1\,\mathrm{cm}^2$  deposited on  $CaF_2$  crystal, chosen for its transparency in the visible range of light.

<sup>&</sup>lt;sup>†</sup> The general effect of particle-particle interaction on the SPR is displayed in Figure 7.2.

<sup>&</sup>lt;sup>‡</sup> In the case of our nanoparticle solutions, control experiments at different concentrations have been performed to ensure that no interaction between the nanoparticles was taking place, as shown in Appendix D.5.

<sup>§</sup> Note that the absorbance is proportional to the absorption cross-section  $\sigma_{abs}$ , but

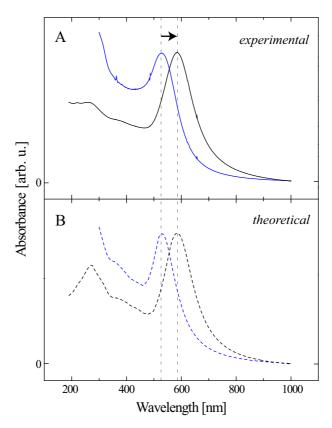


Figure 7.1: A.  $C_{16}$ -capped nanoparticles in chloroform solution (blue) and forming an array (black). A red shift of the surface plasmon resonance is observed between the two systems, from 528 nm to 583 nm. B. Fits corresponding to the two SPR experimental positions, calculated from (2.16).

where the relationships (2.20) were used to determine  $\varepsilon_{Au}(\omega)$ . These fits were made for the two wavelength positions observed in the experimental curves, and the medium permittivities  $\varepsilon_m$  corresponding to these SPR positions were extracted. In the first case (blue), we deduce from the fit curve a value of  $\varepsilon_m \approx 1.8$ , which is comparable to the reported permittivity of the alkane chains <sup>67,179</sup>. This suggests that only the alkane shell influences the nanoparticle SPR, rather than the shell and the solvent ( $\varepsilon_{Chloroform} = 4.8$  at RT). To verify this point, a shell model, taking into account composite particles with core ( $\varepsilon_{core}$ ) and shell ( $\varepsilon_{shell}$ ) in a medium

not equal. Thus the respective intensities are not considered here.

 $(\varepsilon_m)$ , has been investigated\*, and it resulted in similar conclusions. Moreover, a control experiment performed with solvents of different permittivities revealed no variation of the SPR position (see Appendix D.6). In the second case however (black), we obtained a much larger value of the medium permittivity  $\varepsilon_m \approx 3.6$ , suggesting that another effect influences strongly the SPR of the nanoparticles. This effect is, without any ambiguity, the particle-particle interaction, rather strong in the close-packed geometry of the arrays, and possibly combined with substrate influence. Note however that, as there is no contribution of the solvent in the diluted case, there should be a low or no contribution of the substrate in the case of the array.

A possible way to take into account the strong particle-particle interactions in the calculation of the resonance is to consider an effective  $medium^{62}$ . In such a theory<sup>†</sup>, the particle in a medium surrounded by other particles is virtually replaced by a particle in a homogeneous effective medium taking into account the medium itself and the contribution of the other particles. This contribution depends on the averaged volume fraction of particles, which is described by the so-called *filling factor*  $f = V_{clusters}/V_{sample}$ . The effective medium is described by an effective permittivity  $\varepsilon_{eff}(\omega) = \varepsilon_{1,eff}(\omega) + i\varepsilon_{2,eff}(\omega)$ . As already mentioned, the effect on the absorption peak is a shift to the larger wavelength. The closer to each other the nanoparticles are, the higher the particle-particle interactions contribution is, the larger the red shift of the resonance is. Although different effective medium theories have been reported for several situations  $^{173,180}$ , the most popular is the theory proposed by Maxwell  $Garnett^{181}$ . His derivation, given by Equation (7.1), is based on the assumption of homogeneous fields within and outside the nanoparticles, and is limited to small filling factors  $f^{137}$ .

$$\varepsilon_{eff}(\omega) = \varepsilon_m \frac{1 + 2f\Lambda}{1 - f\Lambda}, \qquad \Lambda = \frac{1}{\varepsilon_m} \frac{\varepsilon(\omega) - \varepsilon_m}{\varepsilon(\omega) + 2\varepsilon_m}$$
(7.1)

The condition for the resonance, which is  $\varepsilon_1(\omega) = -2\varepsilon_m$  in the non-

$$\sigma_{abs} \propto \frac{1}{\lambda} \cdot Im \quad \frac{(\varepsilon_{shell} - \varepsilon_m)(\varepsilon_{core} - 2\varepsilon_{shell}) + (1-g)(\varepsilon_{core} - \varepsilon_{shell})(2\varepsilon_{shell} + \varepsilon_m)}{(\varepsilon_{shell} + 2\varepsilon_m)(\varepsilon_{core} + 2\varepsilon_{shell}) + (1-g)(\varepsilon_{core} - \varepsilon_{shell})(2\varepsilon_{shell} - 2\varepsilon_m)}$$

where g is the volume fraction of the shell.

<sup>\*</sup> In this model, the perturbation provoked by a thin shell on the nanoparticle is directly introduced in the absorption cross section, which is then given by :

<sup>&</sup>lt;sup>†</sup> Note that this theory is only valid if the *quasi-static approximation* is fulfilled, namely, when the irradiation light wavelength is much larger than the particles typical length scale, as introduced in the Section 2.2.2.

interacting case, is then  $^{137,175}$ :

$$\varepsilon_1(\omega_{sp})(1-f) + \varepsilon_m(2+f) = 0 \tag{7.2}$$

By implementing this into the main expression for the absorption (2.16), it is possible to find the SPR position as a function of the filling factor  $f^{114,137}$ . Figure 7.2 shows this dependence, for gold nanoparticle in a medium of permittivity  $\varepsilon_m = 2.5$ . The main graph displays absorption curves for different f values from 0 (non-interacting) to 0.7\*, with the inset showing the evolution of the red shift  $\Delta\lambda$  as a function of f. The effect of the particle-particle interactions is clearly demonstrated here, as a red shift and a broadening of the SPR peak.

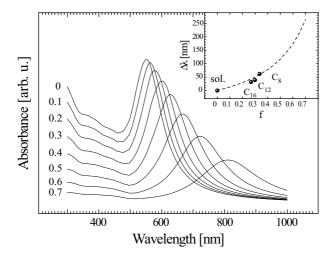


**Figure 7.2:** Theoretical curves calculated for gold nanoparticles within a medium of permittivity  $\varepsilon_m=2.5$  for different filling factors f. The inset shows the evolution of the red shift as a function of f. The dots represent the measured values for the four cases: solution,  $C_{8}$ -,  $C_{12}$ - and  $C_{16}$ -arrays.

In our case, the respective filling factors for  $C_8$ -,  $C_{12}$ - and  $C_{16}$ -arrays have been estimated to  $f_{C_8} = 0.34$ ,  $f_{C_{12}} = 0.30$  and  $f_{C_{16}} = 0.27$ , according to the different inter-particle spacings of those arrays<sup>†</sup>. As shown in the inset, the measured red shifts in the three cases  $C_8$ ,  $C_{12}$  and  $C_{16}$ 

<sup>\*</sup> The larger interaction is observed for hexagonal packing (without inter-particle space), where f=0.74.

<sup>&</sup>lt;sup>†</sup> The filling factors were calculated as  $f = V_{cluster}/V_{box}$  with  $V_{box}$  being the volume of a fictive box of base  $0.74 \cdot (\text{diameter} + \text{inter-particle spacing})^2$  and height (diameter + 2·molecule length), where  $d_{C8} = 2.6$ ,  $d_{C_{12}} = 2.8$  and  $d_{C_{16}} = 3.0 \pm 0.02 \, \text{nm}$ .

match well with the prediction. Note that from this theoretical study, we deduce an expected shift of the SPR of  $9 \pm 2$  nm for a spacing difference of 2 Å in the arrays. This means that small variations in the inter-particle spacing, typically  $\geq 2 \text{ Å}$ , are detectable with this method. The experimental spectra corresponding to the dots in the inset of Figure 7.2 are shown in Figure 7.3. The observed shift from  $C_{16}$  to  $C_{12}$ ,  $\approx 7$  nm, is in full agreement with the theoretical predictions, whereas the shift from  $C_{12}$  to  $C_8$ ,  $\approx 23$  nm, is larger than expected. This may be due to an additional effect occurring only with short alkanes, such as the substrate interaction\* ( $\varepsilon_{CaF_2} = 6.8$ ). Although  $C_{16}$ -arrays was demonstrated to have no interaction with the substrate, shorter capping chains arrays might have some. Despite this small variation to the theoretical predictions, this

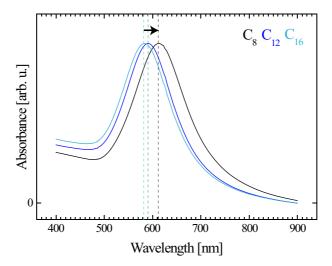


Figure 7.3: Visible absorption spectra of  $C_8$ -,  $C_{12}$ - and  $C_{16}$ -capped nanoparticle arrays (black, blue and cyan curves, respectively). A red shift of the surface plasmon resonance is observed between the three systems, from 583 nm for the  $C_{16}$  to 590 nm for the  $C_{12}$  and to 613 nm for the  $C_8$  system.

study makes us confident as to the ability to detect small inter-particle spacing variations down to 2 Å. Ultimately, it gives us the opportunity to check, with subsequent experiments, whether or not the arrays are distorted by the procedure of molecular exchange.

<sup>\*</sup> The nanoparticle-substrate interaction can be introduced by considering the nanoparticles with medium permittivity  $\varepsilon_m$  on the substrate of permittivity  $\varepsilon_{substrate}$  as if they were in a homogeneous fictive medium of permittivity  $\varepsilon_m^* = \frac{1}{2}(\varepsilon_m + \varepsilon_{substrate})$ .

Secondly, we investigated the optical absorption of  $C_n$ -capped nanoparticle arrays at the three stages of exchange, namely, as-prepared, after OPE-exchange and after  $C_n$ -back-exchange. Figure 7.4A shows this study on a  $C_8$ -array, with the corresponding black (as-prepared), blue (after OPE-exchange) and black dashed (after back-exchange) spectra, respectively\*.

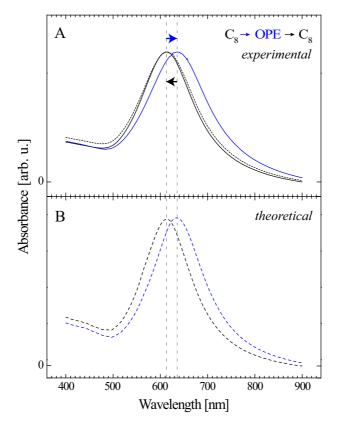


Figure 7.4: A. Visible absorption spectra of  $C_8$ -capped nanoparticle array as prepared (black solid curve), after OPE exchange (blue curve) and after back exchange to  $C_8$  (black dashed curve). A red shift of the surface plasmon resonance is observed after OPE-exchange, from 613 nm to 635 nm. An equivalent blue shift is observed after back-exchange. B. Fits (from (2.16)) corresponding to the two SPR experimental positions.

This measurement firstly reveals that a large red shift of  $\approx 22\,\mathrm{nm}$ 

<sup>\*</sup> This experiment has been performed with  $C_{8}$ -,  $C_{12}$ - and  $C_{16}$ -arrays and demonstrated similar behaviours.

occurs going from  $C_8$  to OPE, and secondly that the SPR goes back to its initial position while back-exchanging the molecules of the array. Since the three measurements were performed on a single array, the red shift observed after the OPE-exchange is not produced by a change of particle-particle interaction, but by a change in the surrounding medium of the particles. As a matter of fact, while only  $C_8$  molecules fill the inter-particle space in the initial state, a certain percentage of these  $C_8$ are exchanged with OPEs. Since OPEs are assumed to have a larger permittivity than  $C_8$ , a red shift of the SPR should be observed according to Mie theory. Hence, the experimental data are in good qualitative agreement with the theory. More remarkably, the SPR back-shift, superposing perfectly with the initial peak, indicates, as the electrical measurements do, that the OPEs are fully removed by the back-exchange procedure. Moreover, the fact that the SPR fully recovers its initial position reinforces the observation that the nanoparticle arrays are stable\*, that is to say the particles do not significantly move away from their initial positions, even after several exchanges.

Figure 7.4B displays the corresponding fits, according to Equation (2.16) and using  $f_{C_8} = 0.34$ , for the two wavelength positions observed in the experimental curves, similarly to Figure 7.1. From these fits, we deduced that the observed red shift was induced by an increase of 0.5 in the permittivity of the surrounding medium. According to the respective permittivities of alkanes  $(\varepsilon_{alkane} = 1.9 - 2.2)^{67,179}$  and OPEs  $(\varepsilon_{OPE} = 3.1 - 3.9)^{182,183}$ , this result is lower than expected<sup>†</sup>. This observation suggests a non-full exchange of the  $C_n$  by the OPE molecules. Indeed, in such a case, the medium permittivity is averaged and depends on the respective concentrations:  $\varepsilon_m = n \cdot \varepsilon_{OPE} + (1 - n) \cdot \varepsilon_{alkane}$ , with n the exchange percentage. This would also explains the variations of the shift observed within different samples<sup>‡</sup>. Infrared studies presented in the following section demonstrate that both types of molecules are indeed present in the array after OPE-exchange.

Let us finally point out that  $1\,\mathrm{cm}^2$  arrays do not have a perfect close packing over the whole surface. By SEM characterisation one observes grain boundaries and vacancies, as well as cracks. To see the influence of these discrepancies, we performed a similar study on selected  $10\times10\,\mu\mathrm{m}^2$  areas presenting a defect-less packing (see Appendix D.7). A sample over

<sup>\*</sup> This assumption was based on SEM observations prior and after exchange.

<sup>&</sup>lt;sup>†</sup> As large variations of the permittivity values are found in the literature, we restrict ourselves to the study of the relative permittivity difference  $\Delta \varepsilon = \varepsilon_{OPE} - \varepsilon_{alkane}$ .

<sup>&</sup>lt;sup>‡</sup> All measurements are reported in Appendix E.2, Table E.4 and Figure E.1.

8 areas taken at specific positions showed reproducible shifts from initial and after OPE-exchange stages. The observed shifts are similar to those observed on large surfaces. However, the initial SPR was found to occur at a larger wavelength (634 nm instead of 613 nm for  $C_8$ -arrays). This may be explained by the better ordering of the array on the considered surface. As no such holes are present in the small selected areas, the array might behave as a more densely packed array, thus exhibiting a SPR at higher wavelength.

To conclude this section, despite slight variations with the theoretical expectations, this study enabled the understanding of the main contributions to the optical absorption of the array as a backbone. This is useful in the prospective characterisation of optically active molecules. The visible spectroscopy enabled us to elucidate several aspects of the molecular exchange: as with electrical characterisation, it demonstrated the ability to perform molecular place-exchange, and to fully remove the inserted molecules after back-exchange. Moreover, it suggested that the exchange is less than 100%. On another hand, as the molecular permittivity is related to the conductivity\*, visible spectroscopy could be an elegant method to predict the ac conductivity of the device, by a simple observation of the SPR position.

## 7.2 Molecular Detection by Infrared Spectroscopy

Vibrational states of organic molecules can be excited by irradiation in the IR region, as shown in the Section 2.1.4. As these states are very specific to each molecule, an IR spectrum of the considered molecule may be seen as its "fingerprint", thus making IR spectroscopy appear an elegant tool for the detection of specific molecules within a heterogeneous sample. In our case, we would like to take advantage of such a method to investigate the composition of the arrays in the three stages: as-prepared, after OPE-exchange and after  $C_n$ -back-exchange, in particular regarding alkanes and OPEs.

Initially, we separately investigated both types of molecules. The alkanes, liquid at RT, were measured pure and diluted in tetrachloride with the help of a semi-demountable KBr liquid cell, whereas the OPEs

<sup>\*</sup> This is exposed in Section 2.3.

were measured in the solid phase, pure or mixed with  $KBr^*$ . The measurements, performed in vacuum with Fourier-transform IR equipment (FTIR)<sup>†</sup>, consisted of the detection of the transmitted IR light passing through the samples. We report in Figure 7.5 the IR spectra of  $C_8$  (pure) and OPE (imbedded in KBr, which is IR transparent) in the range  $k \equiv \frac{1}{\lambda} \in [1000 - 3200] \,\mathrm{cm}^{-1}$ . Those two spectra are the fingerprints for these two molecules and specific characteristics can be observed. Spectral comparisons with reported experimental data <sup>55,184</sup> and DFT calculations using the program  $Gaussian 3^{\odot 185}$  have been done to assign the most important peaks. In the latter case, shown by the blue bars in Figure 7.5, we performed geometry optimisation, and computed harmonic vibrational frequencies and IR intensities at the "B3LYP/6-31G\*" level of theory assuming gas phase of the respective molecules. In order to correct for the systematic errors due to finite basis sets and neglect of anharmonicity we have scaled the computed frequencies by 0.9614 as recommended by Scott and Radom <sup>186</sup>. Note that a shift with respect to the experimental values remains, likely due to the environmental differences (liquid/solid phases  $\leftrightarrow$  gas).

In the  $C_8$  spectrum, one can clearly recognise the  $CH_3$  and  $CH_2$ asymmetric and symmetric stretching vibration resonances in the range  $\nu \in [2800 - 3000] \,\mathrm{cm}^{-1}$ , as well as their deformation vibration resonances  $\delta \in [1300-1500] \,\mathrm{cm}^{-1}$ . These features are very specific to alkanes in general and only the ratio between  $CH_3$  and  $CH_2$  peaks changes for different length of alkanes (see Appendix D.8). These vibrations are sketched in Figure 7.6A. The *OPE* spectrum is much more complicated, since the molecule itself is much larger and more complex. However, this molecular wire is composed of specific main elements: aromatic rings,  $C \equiv C$ triple bonds, S groups at both extremities playing the role of anchors for subsequent immobilisation on gold, and acetyl groups acting as protection of the sulfurs (see Appendix A.2). Although the vibrational peaks of such a "non-trivial" molecule cannot all be assigned, the features corresponding to some specific elements were identified. The large peak around  $1700\,\mathrm{cm}^{-1}$  is typical for the carbonyl C=O vibration from the protecting group. The nearby peaks at 1500 cm<sup>-1</sup> and 1600 cm<sup>-1</sup> are the signatures of the C = C aromatic bonds, as illustrated in Figure 7.6B.

<sup>\*</sup> See the schematics of the liquid cell and KBr-pellet pressing tool in Appendix C.2.2.

<sup>&</sup>lt;sup>†</sup> See the setup details in Appendix C.2.2.

<sup>&</sup>lt;sup>‡</sup> "B3LYP/6-31G\*" stands for Beckes three parameter hybrid functional combined with Lee-Yang-Parr correlation functional methods combined with "6-31G\*" basis set.

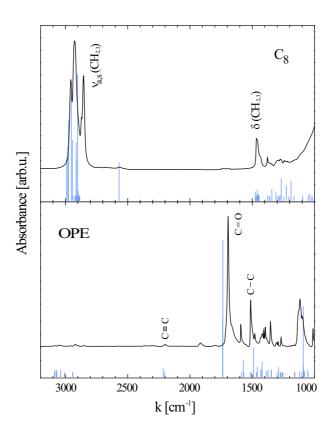


**Figure 7.5:** Measured infrared spectra of  $C_8$  (top) and OPE (down) molecules. The blue bars correspond to a DFT calculation of the molecular vibrations for those two molecules, in the gas phase.

Finally, a weak but very specific peak in the region of  $2200\,\mathrm{cm^{-1}}$  is observed, corresponding to the  $C\equiv C$  triple bonds. Note that the weakness of this vibration, also predicted by the DFT calculations, is due to the large strength of the triple bond, allowing only small spacial variations of the carbon atoms.

In a second step,  $C_n$ -arrays have been investigated with the same method, for the three stages of exchange. The arrays were prepared and deposited on  $CaF_2$  substrates, known to be transparent for IR light. A series of spectra\* corresponding to these three stages, (1), (2), (3) respectively, is presented in Figure 7.7, in the case of a  $C_8$ -array<sup>†</sup>. The pure  $C_8$  and OPE spectra are also shown in the figure to facilitate the comparison.

<sup>\*</sup> The spectra have been y-shifted for clarity.

<sup>&</sup>lt;sup>†</sup> The  $C_{12}$ - and  $C_{16}$ -arrays exhibited exactly the same behaviour.

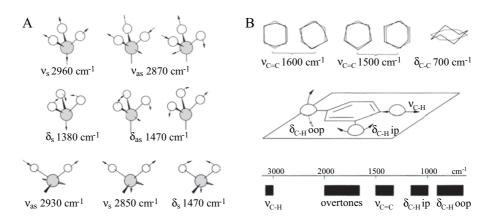


**Figure 7.6:** IR vibrations (stretching  $\nu$  and deformation  $\delta$ ) of two types of compound: A. Alkanes, composed by one methyl and several methylene groups; B. Aromatics, composed by C = C and C - H bonds, vibrating in plane (ip) and out of plane (oop) <sup>55</sup>.

In the as-prepared stage (curve 1), the optical response of the array exhibits the typical features of alkane chains, concretely the  $\nu$  and  $\delta$  methyl and methylene vibrations. Let us mention that the strong S - Au vibration, presumably around 700-900 cm<sup>-1</sup>, is not visible in the investigated range. After *OPE*-exchange (curve 2), the spectrum clearly reveals the coexistence of both the  $C_8$  and the OPE ( $C \equiv C$  at  $\approx 2200 \, \mathrm{cm}^{-1}$  and C = C at 1500 cm<sup>-1</sup>) molecules within the nanoparticle array. However, we note from the relative intensities between (1) and (2) that  $C_8$  was only partially suppressed, so that the exchange percentage is n = 31%. Hence, the place-exchange indeed proceeded to the insertion of OPEs inside the array, but left unchanged some of the initial alkanes. This observation reinforces the hypothesis made after consideration of the visible absorption behaviour\*, which suggested that a certain fraction of the alkanes remains on the nanoparticles during the place-exchange procedure, ensuring a remarkable stability of the array. Further evidence demonstrated by this spectrum is the absence of the very intense C=Ovibration at  $\approx 1700 \, \text{cm}^{-1}$ . This proves that the *OPE*s are well deprotected, and thus strongly suggests that the sulfurs are indeed bound to the gold atoms of the nanoparticles. Let us further remark that the S-Hbonds from the one-side bound OPEs are not observed ( $\approx 2600 \, \mathrm{cm}^{-1}$ ), probably due to their very weak intensity. Finally, after back-exchange

<sup>\*</sup> See Section 7.1.

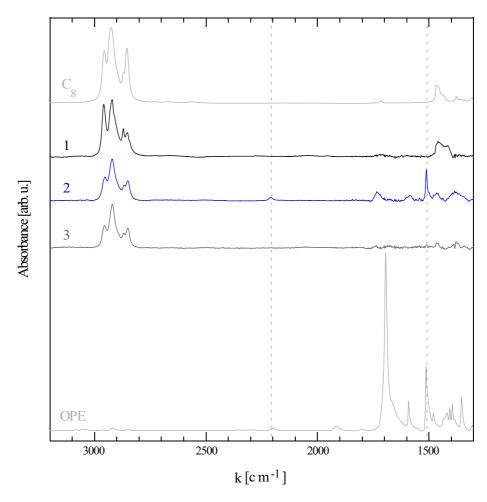


Figure 7.7: Measured IR spectra, from top to bottom: pure  $C_8$  (liquid), 1. as-prepared  $C_8$ -array (on  $CaF_2$  substrate), 2. same array after OPE-exchange, 3. same array after  $C_8$  back-exchange, OPE imbedded in KBr (solid).

(curve 3), the OPE signature is no longer observed, suggesting the total removal of OPEs, whereas the  $C_8$  features remain. Surprisingly, the intensity of  $C_8$  does not re-increase fully to the initial value (1) and remains at an intermediate value (71% of the initial coverage). Hence during the back-exchange, OPEs fully leave but only few  $C_8$  molecules replace them. This difference between the initial and final coverage of the nanoparticles might be due to a reorganisation of the particles surface during the first exchange. Indeed, the initial functionalisation of the particles by  $C_8$  mole-

cules could have induced the formation of holes  $^{187,188,189}$ , increasing the surface of the nanoparticles. The following place-exchanges, being much slower and smoother, might have then aided for a defect-free reorganisation of the nanoparticle surface, thus minimising the energy and the total area. The difference can also be attributed to the different solvents used in both cases (ethanol for the first functionalisation, THF for the back-exchange). On considering all IR measurements performed (listed in Appendix E.2, Table E.6 and displayed in Figure E.2), we can say that the exchange percentage is  $n = 35 \pm 4\%$ , and that the final alkane coverage is  $72 \pm 4\%$  of the initial coverage. Note that these yields are smaller than what was predicted by Murray et al<sup>122</sup> for nanoparticles in solution, likely due to the more complex insertion of molecules into a 2D nanoparticle network. This is also clearly expectable, as we exchange alkanes with much larger molecules (OPE) than in their case.

Note finally that a close examination of the vibration positions gives information on the ordering of the molecules around the nanoparticles. Indeed, in the case of  $C_8$  for instance, whereas the symmetric stretching  $CH_2$  vibration stands at  $2920\,\mathrm{cm}^{-1}$  in a well ordered alkane SAM <sup>141</sup>, it is found to be at  $2926\,\mathrm{cm}^{-1}$  in solution <sup>190</sup> (most disordered). Moreover, it was reported that place-exchange could affect the average conformational ordering of the ligand on nanoparticles <sup>191</sup>. Within the nanoparticle arrays, we note that this peak occurs at  $2923.6\,\mathrm{cm}^{-1}$  in the as-prepared state (1), an evidence for relative disorder of the alkanes. After subsequent OPE-exchange and  $C_n$ -back-exchange, a shift to  $2922.6\,\mathrm{cm}^{-1}$  is observed, suggesting that the molecular exchange ordered the molecules capping the nanoparticles. This effect, if present, could be due to an "annealing" effect of the Au nanoparticles to more spherical surface by successive place-exchanges <sup>122</sup>, in agreement with the low coverage observations. However, there is no compelling proof for it yet.

In summary, IR spectroscopy provided supplementary evidence that deprotected OPEs are inserted inside the nanoparticle arrays after exchange, and can be fully removed by the back-exchange procedure. Based upon intensities and peak positions, we argue that a partial exchange rather than a full exchange of the alkanes by the OPEs takes place. Finally, the confirmed absence of protecting groups evidences the high probability to form Au-S covalent bonds. Although the latter bonds could not be observed in this study, it can be investigated by other techniques, such as XPS for instance, as presented in the next section.

#### 7.3 X-ray Photoelectron Spectroscopy

X-ray Photoelectron Spectroscopy (XPS) allows the identification of the atoms on a surface via the detection of core electrons. X-ray photons\* are used to irradiate the sample's surface, provoking the excitation of the core electrons of the surface's atoms. The outgoing electrons are then detected and counted as a function of their energy. Comparing this energy with well known energy core levels of elements, one can distinguish which elements the surface comprises of and their relative quantity. Although the core electron energy levels have specific positions, these positions are slightly affected by the surrounding atoms. Because such small differences can be resolved, XPS is also able to differentiate atoms bound to various other atoms. In the framework of our investigations<sup>†</sup>, XPS was used to identify the sulfur species, S-H being the signature of OPE molecules in the arrays, and to provide an approximation of the OPE coverage after exchange with respect to the alkanes<sup>‡</sup>.

The experiment has been carried out on three different samples for the three stages: (1) as prepared, (2) after OPE-exchange and (3) after  $C_8$ -back-exchange§. The XPS spectra between 0 and 1100 eV exhibited binding energies of the Si 2s, S 2p, C 1s and O 1s electrons, from low to high energy¶. The identification was performed by comparing the signal with table values  $^{192}$ . As the arrays were deposited on  $SiO_2$ , it is not surprising to detect the electrons of silicon and oxygen, as well as those from carbon contamination. However, we are only interested here in the sulfur signal: in the initial stage, one should see only the S-Au signal from the alkanemonothiols bonded to the gold nanoparticles. Whereas after OPE-exchange, one would expect to see both S-Au and S-H species, the latter corresponding to the free extremity of the OPE which could not bind on both side to the particles.

The spectra at the three stages are shown in Figure 7.8 (1, 2 and 3 respectively). Basing the analysis on gaussian-lorentzian multipeak fits, and taking into account the constraints related to the sulfur two bands

<sup>\*</sup> We used an aluminium source, with an energy of  $K_{\alpha} = 1486.6 \,\text{eV}$ .

 $<sup>^\</sup>dagger$  These measurements have been carried out by P. Morf, Paul Scherrer Institute, Villigen.

<sup>&</sup>lt;sup>‡</sup> The alkane coverage of one nanoparticle has been estimated to be  $\sim 10^3$  molecules (see Appendix B.1.3).

<sup>§</sup> It is delicate to make a comparison of the three different stages on three different samples, since the arrays might show slight differences. However, as all three issued from the same colloidal solution, we assumed that they were globally similar.

<sup>¶</sup> See the full range spectra in Appendix E.2, Figure E.3.

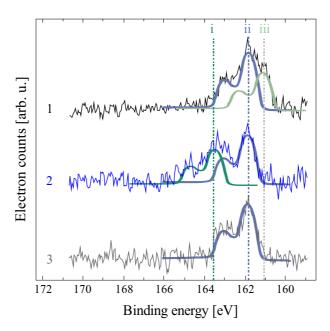


Figure 7.8: XPS spectra of a  $C_8$ -array in the region of the sulfur energies  $(2p\frac{3}{2} \text{ and } 2p\frac{1}{2} \text{ from low to high energy})$ : (1) as prepared, (2) after OPE exchange and (3) after  $C_8$  back exchange. Multipeak fits are shown (thick curves). The energies under i, ii and iii correspond to sulfur signatures of the groups S - H, S - Au and S respectively.

 $(S 2p\frac{1}{2} \text{ and } S 2p\frac{3}{2})^*$ , one can make the distinction between the different sulfur species<sup>†</sup>: the S-Au (ii), present in all 3 stages, the S-H (i), only visible after OPE insertion, as expected, and the S (iii), only present at the initial stage and probably due to accidental decomposition of some alkanes. The presence of S-H groups at the second stage indicates that the OPE indeed was inserted in the array, also suggesting that ultimately, some OPEs were bound on both sides to the nanoparticles. The disappearance of the S-H signal at the third stage shows that the OPE molecules were fully removed, fortifying the evidence of a clean reversible molecular exchange.

In principle, quantitative information can be extracted from the fitted

<sup>\*</sup> The  $S\,2p$  band contains 6 electrons : 2 of them have the spin  $\frac{1}{2}$ , whereas the 4 others have the spin  $\frac{3}{2}$ . Hence, two peaks are expected, with respective area ratio 1:2. Their separation is known to be 1.18 eV.

<sup>&</sup>lt;sup>†</sup> As shown in similar analysis <sup>44</sup>, XPS allows for the identification of different bound and unbound sulfur species.

areas, in particular the relative  $OPE/C_8$  ratio. Although the signal/noise ratio is poor in these measurements, very approximative quantitative contents\* of the three arrays could be determined, as presented in Table 7.1. Note that to allow the comparison, the signals were adjusted in two ways: first, the samples were charged during the X-ray irradiation process. Hence, the measured binding energy shifted by a constant value during the time interval. The relative shifts between the measurements were determined by the observation of the valence spectra and corrected as following: (1) reference, (2) -0.2 eV and (3) -0.9 eV<sup>†</sup>. Second, the three stages were measured on three different samples, meaning that the samples had to be loaded one after the other in the setup and positioned separately. Hence, the signal intensity could vary from one measurement to the other. Each spectrum has been normalised according to the Au signals to enable the comparison between all three samples.

	<b>i</b> (S-H) 161 eV	ii (S-Au) $\approx 162 \mathrm{eV}$	iii (S) $\approx 163.5 \mathrm{eV}$
1 (as prepared $C_8$ )		0.103	0.023
<b>2</b> (after $OPE$ -exchange)	0.046	0.055	
3 (after $C_8$ -back-exchange)		0.055	

**Table 7.1:** Contents of the sulfur atoms S in the three forms (i) S - H, (ii) S - Au and (iii) S, and for the three stages of the exchange (1) as prepared, (2) after OPE-exchange and (3) after  $C_8$ -back-exchange.

Due to the discussed reasons of inaccuracy of the data, the intensities reported in Table 7.1 were interpreted in terms of general tendencies only. We elaborated already on the fact that, after OPE-exchange (2) and only then, S-H bonds are present, saying firstly that no unbound alkane lie in the array at first stage, and secondly that no bound or unbound OPE is present in the third stage. In the second stage, the relative contents between (i) and (ii) species suggest that a substantial fraction of the alkanes were replaced by OPEs. However, these results are too inaccurate and too few to estimate the  $OPE/C_8$  ratio<sup>‡</sup>. In addition, one might note

<sup>\*</sup> The contents is representative of the amount of the specific specie present on the surface.

<sup>&</sup>lt;sup>†</sup> See Appendix D.9 for details on this correction.

<sup>&</sup>lt;sup> $\dagger$ </sup> Note that even with high resolution reproducible measurements, the extraction of the  $OPE/C_8$  ratio would be very delicate, since XPS has a decreasing sensitivity for increasing depth, and that there is surely no evidence that OPEs are homogeneously dispersed around the nanoparticles.

that the initial as-prepared stage exhibits a much larger sulfur density (0.103) on the nanoparticles than the following stages (0.055). Moreover, even after back exchange, the total amount of molecules do not increase back to the initial value, remaining at the lower coverage of the second stage. This behaviour is very similar to what was observed in the IR study, reinforcing the hypothesis of a reorganisation and minimisation of the nanoparticles surface induced by the place-exchange process.

In brief, XPS measurements provided a complementary investigation on the S-Au and S-H bonds, which could not be accessed by IR spectroscopy. The general trends were found to be similar to those observed along the IR study, bringing us confidence on the correct interpretation of the mechanisms involved.

#### 7.4 Concluding Remarks

The tunability of the optical properties of nanoparticle arrays makes optical and photoelectron spectroscopies attractive methods to investigate the mechanism underlying the place-exchange, as well as to bring more insights on the overall structure's and molecules' physical properties <sup>193</sup>.

Since the optical response is dependent on relative permittivities, inter-particle spacing or molecular conformational ordering, it enables us to use such methods as sensors for the composition and conformation of the considered structures. Series of experiments were performed on the arrays, as-prepared, after OPE-exchange and after back-exchange. Visible, IR and photoelectron spectroscopies confirmed different aspects of the molecular exchange, already suggested by electrical measurements. The ability to perform molecular place-exchange with incoming molecules replacing leaving alkanes was demonstrated, by showing the undeniable presence of OPE in the arrays after exchange, combined with the partial loss of the alkanes. Their probable covalent bonding to gold nanoparticles and their reversible removability has also been demonstrated. These techniques gave supplementary insights on the molecular exchange, for example by proving the partial stay of the alkanes, which is a necessary condition for the arrays' robustness.

Ultimately, combining these three approaches, quantitative considerations should lead to the accurate characterisation of the exchanged components, providing important insights regarding the electrical transport through such structures. Moreover, since the structures' permittivity is

strongly related to their conductivity\*, this lets us envision the use of visible spectroscopy as a molecular sensor, or even as an electrical conductivity indicator.

 $<sup>^{\</sup>ast}$  This is highlighted in Section 2.3.

# 8

### Conclusions

#### 8.1 En Route to Molecule/Nanoparticle Hybrid-Systems

To realise the concept of *Molecular Electronics* appears to be technically a great challenge. Although several studies have focused on contacting and measuring the electrical properties of "single molecules", the contacts' influence on the conductance of molecular junctions <sup>194</sup> in "0-dimensional" approaches remains a central issue. This causes large variations in results obtained with different methods of investigation. Hence, there is a need for complementary approaches. The approach of rather considering "contact-molecule-contact" building blocks, such as molecule/nanoparticle hybrid-systems, is likely to circumvent this issue. The challenge then comes down to enabling the easy integration of those blocks into large molecular circuits. In this dissertation, we elaborated on two novel approaches based on this concept, and using a bottom-up fabrication philosophy. Indeed, the assembly of metallic nanoparticles, molecularly functionalised or not, was considered for the preparation of one- and two-dimensional systems. Whereas 1D nanoparticle chains were produced by field-driven assembly of non-functionalised particles, 2D nanoparticle arrays could be achieved by self-assembling functionalised particles at the water/air interface.

We demonstrated in  $Part\ I$  the technique enabling the controlled formation of metallic chains and nanowires of desired length and diameter. We elaborated on the different processes involved, the dielectrophoresis and the anchoring of the particles. The final resistance and appearance of a junction was shown to result from field-driven atomic surface diffusion, facilitated by Joule heating. Such nano-structures can be used to contact nanometre-size objects, possibly in combination with dc electro-

104 Conclusions

migration. We also showed a fast way to establish robust devices based on a few molecules by assembling functionalised nanoparticles.

In Part II, we demonstrated the reversible formation of molecular junction networks using a molecular exchange technique in two-dimensional metallic nanoparticle arrays. Electrical transport measurements, supported by optical characterisation, enabled the investigation of the mechanism underlying the place-exchange. The latter was shown to be a complex mechanism, involving a percolation process. Moreover, it provided information on the network's physical properties, such as electrical resistance, tunnelling decay coefficient and optical permittivity. The reversibility and flexibility of molecularly connected or disconnected nanoparticle networks makes them a valuable platform for the electrical transport study of various organic molecules. Their defect-tolerant character and highly parallel fabrication also makes them good candidate for future circuit implementation.

To elucidate the molecular contacts, we proposed two parallel methods of investigation. We demonstrated their feasibility and robustness. In both 1D and 2D systems, a circuit architecture can be envisioned, consisting of a proper positioning of the micro-fabricated contact electrodes. The good stability, high yield and reproducibility of both methods shall establish these two types of device as promising platforms for the development of molecular circuits.

# 8.2 Prospects: The Vast Possibilities offered by Hybrid-Systems

In terms of molecular properties, although the needs of *Molecular Electronics* are clearly defined, the way to implement them in real circuit is not straight forward. One usually begins by designing a molecule with specific properties, and then characterises it. Upon observation of the real behaviour of the molecule, it might have to be re-designed accordingly. Hence, one has to constantly re-consider those interlinked aspects: "design of molecule  $\rightleftharpoons$  characterisation", until reaching the desired effect. This implies in particular a permanent "physicist/chemist" feed back.

Keeping this in mind, the contribution of the contacts to the transport properties could be further investigated in our systems by using different nanoparticle materials, such as platinum or palladium, or choosing different anchor groups of the molecules, like dithiol groups or selenium groups. Concerning the signature of the molecule itself, we would like to implement more complex molecules in our systems, typically functional molecules such as optical switches or redox-active molecules. By using magnetic nanoparticles (typically cobalt particles), one can even think of investigating the spin transport through specific molecules. Whereas nanoparticle chains would be suitable for "single/few molecules" electric transport investigations, 2D nanoparticle arrays would give the "ensemble electrical properties", possibly different due to collective effects. In addition, one might take advantage of environmental effects to use nanoparticle arrays as molecular sensors. In particular, optical inspection might lead to an independent determination of the electrical conductivity of the molecule/nanoparticle hybrid-system. In a more technological direction, an interesting challenge would be to perform local incorporation of functional molecules at specific sites, separately addressable. This would let one envision the realisation of complex circuits based on molecular networks.

## APPENDIX

# A

# TECHNICAL DATA ON INVESTIGATED MOLECULES

#### A.1 Alkanethiol Chains: $C_8$ , $C_{12}$ , $C_{16}$

Alkanethiol molecules have been used in this work as functionalisation for the nanoparticles. We can differentiate these "spacer molecules" referring to the initial state of the arrays, with the "active molecules", referring to the molecules under study that we insert in a second step.

These molecules are suitable for our experiments, since they are not conjugated, thus very low conductive, and they bind easily to gold, thanks to their thiol group. Note that they are non-reactive on their other side  $(CH_3 \text{ group})$ . We used alkane molecules of 3 different lengths in order to vary the spacing between the nanoparticles in the self-assembly experiments. Those three molecules have been acquired commercially (Fluka).

#### A.1.1 Octanethiol

Octanethiol has been used as the reference "spacer molecule". Its length is such that an assembly of  $C_8$ -capped nanoparticles is suitable to contact "active molecules" of about 2 nm. The inter-particle distance in the array yield with  $C_8$  is  $d_{C_8} = 2.6 \pm 1.4$  nm (see Appendix B.3.2).

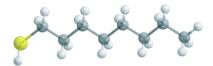


Figure A.1: Ball & stick model of the octanethiol molecule.

For use as reference data for the IR measurements, IR spectra have been performed on octanethiol in liquid phase (in diluted solution and pure), as shown in Figure A.2. Note that the IR response is similar for

Molecule formula	$C_8H_{18}S$
Molecular weight	$146.3\mathrm{g/mol}$
End group	-SH
Length (incl. end groups)	$1.3\mathrm{nm}$
Homo-Lumo gap	$8{\rm eV}^{195}$
Dielectric constant	$2.25^{179}$

Table A.1: Technical data of octanethiol molecules.

all alkanes excepted the respective intensities of  $CH_2$  vibrations, which are proportional to the number of  $CH_2$  groups, hence to the number of C atoms. A comparison is shown in Appendix D.8.

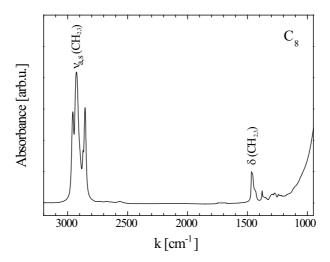


Figure A.2: Infrared spectrum of  $C_8$ . The  $CH_3$  and  $CH_2$  showing the typical stretching vibration resonances (around  $2900 \,\mathrm{cm}^{-1}$ ) and deformation vibration resonances (around  $1400 \,\mathrm{cm}^{-1}$ ) are visible.

#### A.1.2 Dodecanethiol

This molecule has been used to obtain a larger inter-particle spacing. The latter was found to be  $d_{C_{12}} = 2.8 \pm 1.4 \,\mathrm{nm}$  (see Appendix B.3.2). In our experiments,  $C_{12}$  is the second most used spacer molecule, and was mostly used for comparison purpose with octanethiol. Typically, in the past few

years, this molecule has been extensively electrically investigated, as a comparison molecule for different systems <sup>146,148,149</sup>.

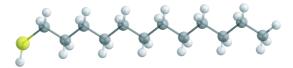


Figure A.3: Ball & stick model of the dodecanethiol molecule.

M. L L. C L.	C $H$ $C$
Molecule formula	$C_{12}H_{26}S$
Molecular weight	$202.4\mathrm{g/mol}$
End group	-SH
Length (incl. end groups)	$1.8\mathrm{nm}$
Homo-Lumo gap	$8{ m eV}^{195}$
Dielectric constant	$2.25^{179}$

**Table A.2:** Technical data of dodecanethiol molecules.

#### A.1.3 Hexadecanethiol

Hexadecanethiols have been used in order to get an even larger interparticle spacing, and ultimately investigate longer "active molecules". The inter-particle distance with these molecules is  $d_{C_{16}} = 3.0 \pm 1.4 \,\mathrm{nm}$  (see Appendix B.3.2). Although they are longer than  $C_8$  and  $C_{12}$ ,  $C_{16}$  are also more flexible and some care has to be taken to ensure that they stay straight during the self-assembly manipulation.

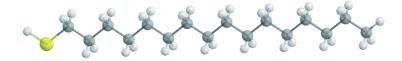


Figure A.4: Ball & stick model of the hexadecanethiol molecule.

These molecules present the disadvantage to be solid at room temperature, which implies a heating procedure, making manipulations delicate. We performed the self-assembly both at room temperature and at higher

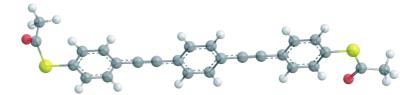
Molecule formula	$C_{16}H_{34}S$
Molecular weight	$258.5\mathrm{g/mol}$
End group	-SH
Length (incl. end groups)	$2.3\mathrm{nm}$
Homo-Lumo gap	$8{\rm eV}^{195}$
Dielectric constant	$2.25^{179}$

Table A.3: Technical data of hexadecanethiol molecules.

temperature (30°, 40°) to investigate possible changes in the inter-particle distance, but no substantial difference was reproducibly demonstrated. Nevertheless, because they interdigitate better than  $C_8$  and  $C_{12}$  irrespective to the temperature, they enable to form better ordered arrays.

#### A.2 OLIGO(PHENYLENE ETHYNYLENE)

The first "active molecule" under investigation has been the Oligo(phenylene ethynylene) (*OPE*). It is a simple molecular wire, conjugated, thus conducting, and having two thiol anchor groups to create covalent bonds with gold. Furthermore, this molecule has been widely investigated experimentally <sup>146,147,148,149,150,151</sup> as well as theoretically and is thus a good "test molecule" to probe our experimental design. Its length was calculated with a mm2 procedure, after energy optimistion. This molecule was synthesised by M. Langer, Prof. A. Pfalz, Chemistry Department, University of Basel.



**Figure A.5:** Ball & stick model of the *OPE* molecule, including acetyl protecting groups.

IR and visible spectra have been measured in KBr/OPE mixture bullet (placed in a vacuum chamber) and in chloroform solution respectively (Figure A.6). These data have been used to interpret the IR and

Molecule formula	$C_{24}H_{18}O_2S_2$
Molecular weight	$426.55\mathrm{g/mol}$
End groups (symmetric)	$-SCOCH_3$
Length (incl. end groups)	$2.02\mathrm{nm}$
Homo-Lumo gap	$3.51\mathrm{eV}^{146},3.70\mathrm{eV}^{170}$
Dielectric constant	$3.1^{182}$

Table A.4: Technical data of *OPE* molecules.

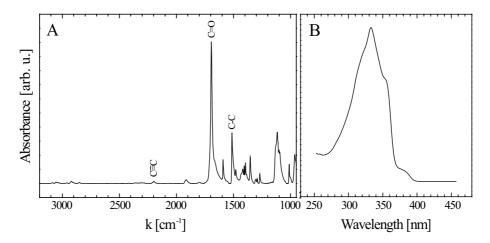


**Figure A.6:** A. Infrared absorption of OPE molecules, imbedded in a KBr matrix. The fingerprint reveals the  $C \equiv C$ , C = O (protecting group) and the C = C (aromatic rings) vibrations. B. visible absorption of OPE.

visible spectra of the arrays.

#### A.3 OLIGO(PHENYLENE VINYLENE)

As second "active molecule" under investigation, we chose a very similar molecule, Oligo(phenylene vinylene) (OPV), were the only difference as compared to OPE resides in the double bonds inter-linking the aromatic groups, replacing the triple bonds of OPE. The aim was to investigate the effect on the electrical transport properties of such an internal difference. This molecule was also previously extensively investigated  $^{146,148,149,167}$ . It was synthesised by V. Horhoiu, Prof. M. Mayor, Chemistry Department, University of Basel.

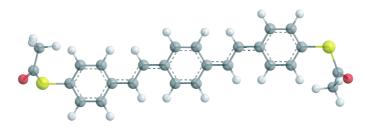


**Figure A.7:** Ball & stick model of the *OPV* molecule in its 'long' conformation, including acetyl protecting groups.

Molecule formula	$C_{26}H_{22}O_2S_2$
Molecular weight	$430.58\mathrm{g/mol}$
End groups (symmetric)	$-SCOCH_3$
Length (incl. end groups)	$1.98\mathrm{nm}$
Homo-Lumo gap	$3.12\mathrm{eV}^{146}$
Dielectric constant	$3.1^{182}$

**Table A.5:** Technical data of *OPV* molecules.



## FABRICATION PARAMETERS

#### B.1 COLLOIDAL SOLUTIONS

The different colloidal solutions needed for the presented experiments were produced in our laboratories. We focused on the preparation of charge-stabilised nanoparticles, as this simple procedure allows the preparation of large nanoparticle (typically > 5 nm). Note that another method, the growth by ligand capping <sup>196</sup>, is also possible, but yield in much smaller particles (typically 1-3 nm). Unless mentioned, all reagents were purchased from Fluka and used as received.

#### B.1.1 Charged-Stabilised Au Colloidal Solution

The two following recipes have been used to fabricate gold nanoparticles. The first recipe was used in the framework of the 1D-system and is based on the method of Turkevich  $et~al^{197}$ . The second one, based on the method of Slot  $et~al^{198}$ , provided colloids designed for the 2D-systems.

Fabrication	Heat up to	boiling point	with const.	stirring
-------------	------------	---------------	-------------	----------

 $1ml\ HAuCl_4\ (10\,\mathrm{mM}) + 19\,\mathrm{ml}\ H_2O \to 0.5\,\mathrm{mM}$  Add fast  $0.4\,\mathrm{ml}\ \mathrm{citric\ acid}(0.2\,\mathrm{M}) \to 4\,\mathrm{mM}$ 

Keep boiling and stirring 10 min

Cool down to RT keeping stirring and refill with  $H_2O$ 

**Properties** Red transparent solution

Colloids between 20 and 100 nm, as a funct. of  $c_{acid}$ 

Standard deviation: 10%

Concentration:  $\sim 10^{12} \, \text{particles/ml}$ Stability:  $> 2 \, \text{months}$  (in the fridge)

**Table B.1:** Recipe for the charge-stabilised gold nanoparticle synthesis based on the method of Turkevich <sup>197</sup>.

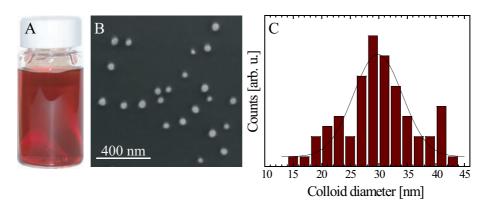


**Figure B.1:** A. Picture of gold colloidal solution. B. SEM image of the nanoparticles. C. Size distribution (Turkevich's method).

An aqueous solution of  $HAuCl_4$  is brought to boiling temperature while stirring constantly. Aqueous acidic solution is then quickly added. Gold atoms are reduced from  $Au^{3+}$  to  $Au^0$ , and thus can pack, forming neutral colloids surrounded by  $Cl^-$  shells. The solution exhibits then an intense red colour without losing its transparency (Figure B.1A). The colloidal solution is kept at boiling temperature for 10 minutes and then slowly cooled down to room temperature with a constant stirring.

Fabrication	Gold solution: $1 \text{ ml } HAuCl_4 \ (1\%) + 79 \text{ ml } H_2O$ Reducing solution: $4 \text{ ml } \text{trisodium } \text{acid } (1\%) + 80 \mu\text{l } \text{tannic } \text{acid } (1\%) + 16 \text{ml } H_2O$ Heat up both solutions separately to $\approx 60^{\circ}\text{C}$ Mix them and heat up to boiling point while stirring Keep boiling and stirring $10 \text{ min}$ Cool down to RT keeping stirring and refill with $H_2O$
Properties	Red transparent solution Colloids between 5 and 20 nm, as a funct. of $c_{tan.ac.}$ Concentration: $\sim 10^{13}  \mathrm{particles/ml}$ Standard deviation: $8  \%$ Stability: $\sim 1  \mathrm{month}$ (at RT)

**Table B.2:** Recipe for the charge-stabilised gold nanoparticle synthesis based on the method of Slot <sup>198</sup>.

The two methods result in nearly monodispersed neutral Au nanoparticles, as shown in Figure B.1C and Figure B.2. The  $(Cl^{-})$  negative shells play the role of stabilising agent, preventing the nanoparticles to aggregate. The particle diameter is tuned by the concentration of the reducing agent. The concentrations proposed in the two recipes lead to particle diameter of 20 nm and 10 nm respectively.

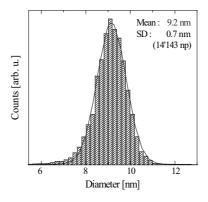


**Figure B.2:** Size distribution of the gold nanoparticles synthesised by Slot et al's method <sup>198</sup>:  $\emptyset = 9.2 \pm 0.7$  nm (statistic on 14'000 part.).

#### B.1.2 Charged-Stabilised Pd Colloidal Solution

Palladium nanoparticles have also been considered. Their fabrication is very similar to gold (Figure B.3), as Pd is also a noble metal and has similar atomic properties. First,  $H_2PdCl_4$  has to be prepared using  $PdCl_2$  and HCl in aqueous solution. Then, similarly to gold, we proceed to the reduction of  $H_2PdCl_4$  by an acid.

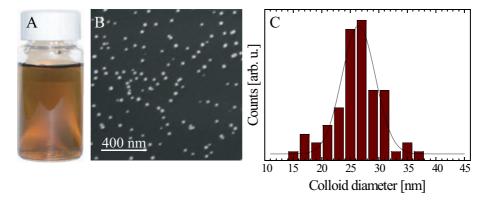


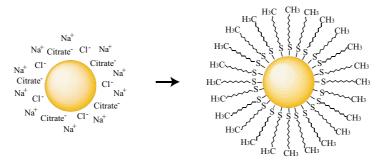
**Figure B.3:** A. Picture of palladium colloidal solution. B. SEM image of the nanoparticles. C. Size distribution.

 $\begin{array}{lll} \textbf{Fabrication} & \textbf{Stock solution of } H_2PdCl_4: \textbf{Sonicate} \approx 40\,\text{min} \\ & 100\,\text{ml } HCl\ (3\,\text{mM}) + PdCl_2\ (1\,\text{mM})\ \text{powder} \\ & \textbf{Heat up to boiling point with const. stirring} \\ & 10\,\text{ml } H_2PdCl_4\ (1\,\text{mM}) + 10\,\text{ml } H_2O \rightarrow 0.5\,\text{mM} \\ & \textbf{Add (fast) } 0.4\,\text{ml phosphorous acid}(0.2\,\text{M}) \rightarrow 4\,\text{mM} \\ & \textbf{Keep boiling and stirring } 10\,\text{min} \\ & \textbf{Cool down to RT keeping stirring and refill with } H_2O \\ \textbf{Properties} & \textbf{Brown transparent solution} \\ & \textbf{Colloids between 20 and 30\,\text{nm, as a funct. of } c_{phosph.ac.} \\ & \textbf{Standard deviation : } 11\,\% \\ & \textbf{Concentration : } \sim 10^{14}\,\text{particles/ml} \\ & \textbf{Stability : } > 2\,\text{months (in the fridge)} \\ \end{array}$ 

**Table B.3:** Recipe for the charge-stabilised palladium nanoparticle synthesis.

#### B.1.3 Functionalisation of Charged-Stabilised Au Colloids

Gold nanoparticles encapsulated in alkanethiol chains ( $C_8$ ,  $C_{12}$  and  $C_{16}$ ), as shown in Figure B.4, were produced using the colloids obtained with the second recipe, following the procedure described by Huang *et al* <sup>124</sup>. Then, they were used for subsequent self-assembly experiments.



Charge stabilised nanoparticle

Ligand stabilised nanoparticle

**Figure B.4:** Schematic of the nanoparticle stabilisation: from charge-stabilised nanoparticles (in aqueous solution) to alkane-functionalised nanoparticles (in non-polar solvent).

Alkanethiols being not miscible in water, the nanoparticles are first transferred from water to ethanol with help of centrifugation. Then, colloidal solution ( $10^{13}$  particles/ml) and alkane solution ( $30\,\mathrm{mM}$ ) can be mixed. After the immobilisation of the alkane chains on the nanoparticles, the latter are rinsed in order to remove the molecules in excess. We estimate the number of alkanethiols covering one nanoparticle to  $\sim 10^{3*}$ . Finally, the functionalised particles are infused in a suitable medium for self-assembly, typically hexane/dichloromethane or chloroform.

#### Preparation

Centrifuge 10 ml of colloidal solution @ 13'000 turns/min for 45 min Remove fully the supernatant

Infuse ethanol  $(C_2H_6O)$  and shake vigorously

Perform an ultrasonic treatment (10 min @ medium power) and degas Dissolve 96  $\mu$ l pure alkane in 4 ml ethanol; add to the colloidal solution Wait 1-2 days in a light-proof place (capped nanoparticles precipitate) Remove the supernatant and reinfuse ethanol; wait  $\approx 30 \, \text{min}$ 

Remove fully the supernatant and infuse  $4 \,\mathrm{ml}$  chloroform  $(CHCl_3)$ 

**Properties**: Red transparent solution; Stability:  $\sim 1$  week (at RT)

# B.2 Electrodes' Preparation for 1-Dimensional Systems

We summarise here the main steps of fabrication of the micro-electrodes used for the 1D systems. Figure B.5 shows the three levels of contacts which enable to address such structures.

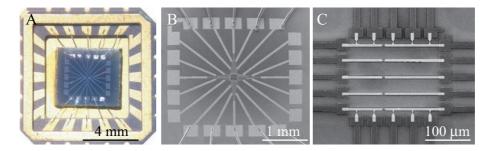


**Figure B.5:** A. Picture of the bonded sample (inside a socket). B. UV-lithographied external pads. C. Internal central pads and electrodes, e-beam lithographied.

<sup>\*</sup> We find  $\approx 1500$  considering a particle with external surface of  $300\,\mathrm{nm}^2$  and alkanes apparent cross section of  $0.21\,\mathrm{nm}^2$ , and  $\approx 5000$  via IR measurements.

Preparation of the substrate UV Lithography*	cut/clean $SiO_2$ wafer, $21 \times 21 \mathrm{mm}^2$ $N_2$ blow - US in acetone, then in isopropanol, $N_2$ blow - 5 min Ozon spin-coat photoresist ma-N415 $40 \mathrm{s}$ @ $4000 \mathrm{t/s}$ plate bake $90 \mathrm{s}$ @ $100 \mathrm{^{\circ}C}$ align sample and pre-cleaned mask illuminate with UV light for $25 \mathrm{s}$
	develop (ma-D $332S$ ) $23-25s$
Normal Evaporation <sup>†</sup>	$30\mathrm{s}$ Ozone heat chamber $30\mathrm{min}$ ( $P\sim 10^{-6}\mathrm{mbar}$ ) cool chamber/sample $1\mathrm{h}$ ( $P\sim 10^{-7}\mathrm{mbar}$ ) evaporate $5\mathrm{nm}$ $Ti$ / $45\mathrm{nm}$ $Au/Pt$ @ RT lift off in acetone @ $50-70\mathrm{^{\circ}C}$ rinse in isopropanol - $N_2$ blow
e-Beam Lithography <sup>‡</sup>	spin-coat $PMMA - MA(33\%)$ 40 s @ 6000 t/s bake in oven 30 min @ 175°C spin-coat $PMMA$ : $Chlorobenzene1:3$ 40 s @ ,, bake in oven 30 min @ 175°C adjust the electron beam parameters: current 40 pA, focus/stigm., magn. 300'000 wait 30 min (stabilisation); select/design mask irradiate: dose 40%, step 2, dwell time $6.4 \mu s$
Angle Evaporation	put $Ag$ paste/vacuum grease under the sample heat chamber 1 h $(P \sim 10^{-6} \text{ mbar})$ cool down 2 h $(N_2 \text{ cooling})$ $(P \sim 10^{-7}, T \approx 0^{\circ})$ evaporate 5 nm $Ti @\pm \alpha$ ; $20 \text{ nm } Au/Pt @\pm \alpha, 0^{\circ}$ lift off @ $50 - 70^{\circ}$ C rinse in isopropanol - $N_2$ blow
SEM	adjust focus, stigmatism and wobbling
Observation <sup>§</sup>	accel. voltage: 15 kV(Philips)/0.5 kV(LEO)
Bonding ¶	paste sample in socket adjust level of the tip set parameters (both shots) : power, time

<sup>\*</sup> Karl Süss

† Balzers-Pfeiffe PLS500

‡ Jeol JSM-IC848

§ Philips XL30 / LEO supra
¶ Kulicke & Soffa 4523a digital

#### B.3 2-DIMENSIONAL SYSTEMS

Here, we focus on the stamp preparation, the parameters of fabrication of the nanoparticle arrays, and the parameters of the molecular exchange.

Preparation of PDMS stamp	mix prepolymer gel and curing agent (Sylgard 184, Corning) cast it on a molt having the desired patterns degas 30 min @ RT bake @ 60°C for 1-2 hours peal off and cut
Self- Assembly	prepare subsequent water convex surface cast $400\mu l$ of colloidal solution @ water/air interface evaporate the solvent under hood (5 min @ 100 ft/s) transfer SAM on a stamp by touching the interface withdraw slowly the stamp away from water transfer the SAM on a substrate by soft contact
Pad Shadow	align SAM stripes with a TEM grid
Evaporation	heat chamber $30  \text{min} \ (P \sim 10^{-6}  \text{mbar})$ cool down chamber $1  \text{h} \ (P \sim 10^{-7}  \text{mbar})$ evaporate $5  \text{nm} \ Ti \ / \ 65  \text{nm} \ Au \ @ \ RT$
Exchange	prepare $2 \text{ ml}$ of $1 \text{ mM}$ $OPE$ in $THF$ under $Ar$ flow insert the sample in the vial, face down add deprotection agent $NH_3$ under $Ar$ flow wait $5 \text{ min}$ and seal (under $Ar$ ); wait $24 \text{ hours}$ rinse the sample in pure $THF$ for $10 \text{ min}$ - $N_2 \text{ blow}$

#### B.3.1 PDMS stamp

The PDMS stamp is produced following a method described elsewhere  $^{199}$ : cured Polydimethylsiloxane is casted on a UV-lithographied molt, baked, and then pealed away from the molt (see Figure B.6). Finally, it is cut along the pattern structures.

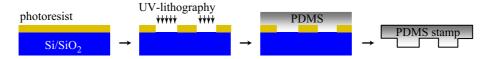
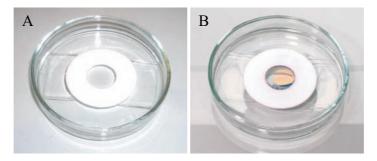


Figure B.6: Schematics of the PDMS stamp fabrication.

The patterning performed in our case was composed by long parallel stripes of  $20\text{-}25\,\mu\mathrm{m}$  wide and spaced by  $20\,\mu\mathrm{m}$ . One such fabrication procedure allowed the production of about 32 stamps.

#### B.3.2 Self-assembly

The self-assembly of the nanoparticles into an array takes place at the moment when the solvent of the colloidal solution evaporates. A picture of the SAM of nanoparticle at the water/air interface is shown in Figure B.7B. Whereas the colloidal solution is ruby red (in transmission), due to an intense absorption of green light (surface plasmon resonance), the colour changes while particles pack because of a red shift of the SPR and broadening of the band, induced by increasing particle-particle interaction (see Section 7.1). Green and red absorptions induce also green and red reflections, which are responsible for the gold colour of the film, as observed in Figure B.7B.



**Figure B.7:** Pictures of the self-assembly setup: a hollowed teflon disk determines the water convex surface. A. The red colloidal solution is slowly poured. B. During solvent evaporation, the particles self-assemble, forming a golden film of about 1 cm<sup>2</sup>.

As-prepared arrays have well spaced particles, with their spacing controlled by the capping alkanes' length. On Figure B.8, a complete study, based on TEM images, is presented, where one can see the centre-to-centre spacing dependance as a function of the alkanes' length. From the measurements of the nanoparticles diameter (see Figure B.2), one can deduce the respective inter-particle separation length:  $d_{C_8} = 2.6 \pm 0.02 \,\mathrm{nm}$ ,  $d_{C_{12}} = 2.8 \pm 0.02 \,\mathrm{nm}$  and  $d_{C_{16}} = 3.0 \pm 0.02 \,\mathrm{nm}$ . Note that this error is an error on the average value of the inter-particle distance of the array and do not consider variations between different sites. Calculated from the

FWHMs of the particle size (Figure B.2) and the centre-to-centre Figure B.8 respective standard deviations, this variation amounts to 1.4 nm.

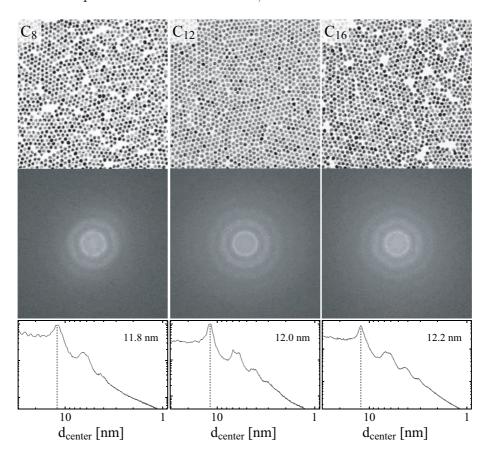


**Figure B.8:** Full comparison of TEM images of  $C_8$ -,  $C_{12}$ - and  $C_{16}$ -arrays from left to right  $(400 \times 400 \, \mathrm{nm}^2)$ . Below, the corresponding FFT  $(8 \times 8 \, \mathrm{nm}^{-2})$  are represented, and the spectra circular average. These graphs display the centre-centre distance. In combination with Figure B.2, they inform about the inter-particle spacing in each case:  $d_{C_8} = 2.6 \, \mathrm{nm}, \, d_{C_{12}} = 2.8 \, \mathrm{nm}$  and  $d_{C_{16}} = 3.0 \, \mathrm{nm}$ , with 1.4 nm standard deviation and 0.02 nm error.

#### B.3.3 Shadow Evaporation

The contact pads (5 nm Ti + 65 nm Au thick) were evaporate on the top of the printed monolayer stripes through a TEM grid, used as a shadow mask (as schematically shown in Figure B.9). Indeed, UV-lithography

was avoided for two reasons. First, the resist might pollute the SAM, and secondly, the heating procedure included in the UV-lithography process can induce the coalescence of the nanoparticles (see Section B.3.5).

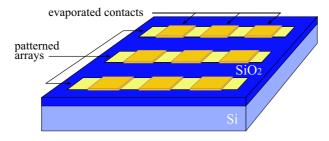


**Figure B.9:** Concept of the shadow evaporation through TEM grid, on the top of the array stripes.

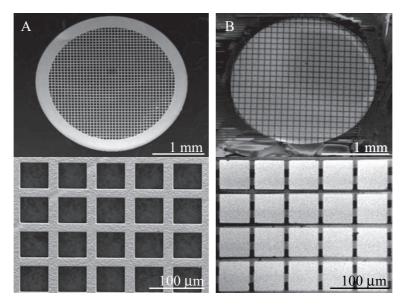


**Figure B.10:** Shadow evaporation of the contact pads (top: whole structure; down: zoom in): A. SEM images of a TEM grid used as shadow mask; B. SEM images of the corresponding pads on the nanoparticle array, after evaporation through the TEM grid.

With such a soft procedure, the stripes of nanoparticle arrays get partially covered by square Au contact pads, corresponding to the holes of the grid. Figure B.10 shows SEM images of the TEM grid (A) and of the subsequent gold evaporated through it on a sample (B). The effective

array between two consecutive pads is generally composed of one or two stripes, of length  $l=10\,\mu\mathrm{m}$  and total width  $w=20-40\,\mu\mathrm{m}$ . According to SEM inspection, the arrays are kept intact, with no noticeable change of the structure after evaporation of the contact pads.

#### B.3.4 Molecular Exchange

Concerning the molecular exchange, and as mentioned in Appendix A, OPE and OPV molecules have protecting groups on both ends. Prior to the exchange, these groups have to be removed properly, to enable the binding of the molecules in the network. To do so, we used ammonium hydroxide  $(H_3N)$  as deprotecting agent. Typically the concentration of this agent and the temperature strongly influence the rate and speed of deprotection. Whereas we have been working without temperature regulation (RT), we optimised the concentration to obtain a slow and only partial deprotection of the molecules after 24 hours.

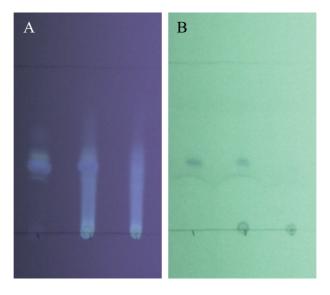


**Figure B.11:** TLC test of OPE molecules: A. 365 nm, B. 254 nm illumination. The three traces correspond from left to right to pure protected molecules, mixing of protected and deprotected molecules, and pure deprotected molecules.

To check the efficiency of the deprotection, we performed thin layer chromatography (TLC), which consists on inducing a migration of the molecules on a silica gel substrate. This test is performed by first making

a spot with the molecules in solution (here THF), drying it, and letting it migrate vertically with a solvent (here hexane/dichloromethane 1:3). Since the molecules fluoresce, it is possible to see their trace under UV light. Figure B.11 shows a typical TLC test of OPE molecules, illuminated with wavelengths of 365 nm (A) and 254 nm (B). From left to right, the three traces correspond to pure protected molecules, mixing of protected and deprotected molecules, and pure deprotected molecules. When the molecules are protected, they don't interact with the substrate, thus the whole spot migrates with the solvent. That's what one can observe on the left trace. On the other hand, when the molecules are deprotected, the sulfur atoms bind to the silica gel and thus the molecules expend into a "tail" on the whole way of the migration. This tail is clearly observed on the right trace. Quite remarkably, one can detect the two compounds in the middle trace, composed of both protected molecules and deprotected molecules. One notices that the tails are strongly visible on Figure B.11A, whereas the spots are better distinguishable on Figure B.11B. As final remark, one sees as well a residual spot were deprotected molecules were deposited (clear on Figure B.11B). This is an aggregation of polymerised molecules, which does not migrate with the solvent. This polymerisation results from a reaction with oxygen during the deprotection process, forming disulfide bonds. During our exchange experiment, care was taken to work under argon atmosphere, so as to avoid such a polymerisation.

#### B.3.5 Damaged Arrays

Although there is no doubt about the high stability of the arrays, after several months, or after bad treatment (strong light exposure, high temperature exposure, extensive SEM observation), the nanoparticles of the array may coalesce, destroying thus the hexagonal-ordered array. Indeed, under such conditions, the alkanethiols, playing the role of spacer and stabiliser between the particles, can undergo a desorption process. When their number gets insufficient to keep the stability of the particles, the latter begin to move. When they meet each other, they (partially) coalesce, so as to minimise their surface energy <sup>200</sup>, as demonstrated by Figure B.12A & B.

This phenomena can easily be detected in our arrays, with SEM characterisation, but also via electrical or optical measurements, as exposed in Figure B.12C and D respectively. We observe on Figure B.12B the initial formation of random paths, typical for nanoparticle coalescence. Those metallic paths, when long enough, make the resistance of the junction

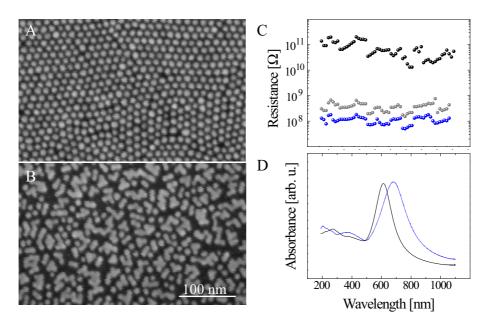


Figure B.12: SEM images of an as-prepared  $C_8$ -array before (A) and after coalescence (B). C. Electrical evidence of coalescence: as prepared  $C_8$ -array (black), after OPE exchange (blue) and after back exchange and coalescence (grey). D. Optical evidence of coalescence: as prepared  $C_8$ -array (black), coalesced  $C_8$ -array (dashed blue). One observe a 67 nm red shift in the surface plasmon vibration resonance going from well separated nanoparticles and coalesced nanoparticles.

smaller (percolation), and independent of the type of molecules present in the array (see Figure B.12C). Moreover, those much larger structures exhibit an optical absorption at dramatically longer wavelengths, easily detectable by optical spectroscopy, as shown by Figure B.12D.



## MEASUREMENT SETUPS

#### C.1 1-DIMENSIONAL SYSTEMS

#### C.1.1 Trapping

An electronic broad-band setup has been designed specifically for the ac trapping experiments. Indeed, as the experiments were done at a relatively high frequency (f = 1 MHz), connectors and cabling had to be minimised in order to avoid large circuit capacity and impedance. This setup was designed to perform alternatively two kinds of measurements: the  $trapping\ experiment$ , allowing large currents through the junction, and the  $resistance\ measurement$  of formed junctions, limiting the current to avoid any further change of the resistance. In Figure C.1, the electronics

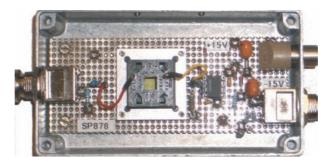


Figure C.1: Broadband electronics, designed to perform both trapping experiment and resistance measurement at room temperature. From left to right: input connector, series capacitor, sample holder, series resistor (interchangeable) and output connector. In the configuration of resistance measurement, the series capacitor is replaced by a  $1 \text{ M}\Omega$  resistor, and the series resistance by an I-V convertor with gain  $10^5$ .

is set in the *trapping* configuration. One can recognise, from left to right, the input connector, the series capacitor, the sample holder, the series

resistor (interchangeable) and the output connector. The corresponding schematic is shown in Figure C.2. In this setup, the voltage V and the series resistance  $R_s$  are tunable. The measurement of the impedance of the junction as a function of time is performed two folds: with an oscilloscope (Tektronix TDS 2012), and a lock-in amplifier (EG&G 5302 Amplifier) placed after a voltage divider 1:100, directly in parallel with the series resistor.

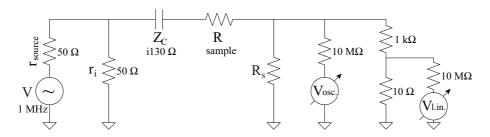
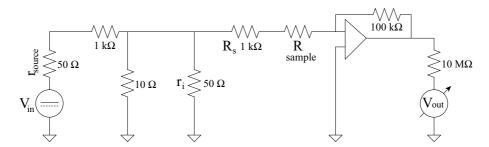


Figure C.2: Passive circuit for broadband trapping electronics.

#### C.1.2 RT Electrical Measurements

As mentioned above, the same broadband electronics has been used for the resistance measurement of the junctions at room temperature (Figure C.1). In the resistance measurement configuration, we have from left to right, the input connector, a series resistor of  $1 \,\mathrm{k}\Omega$ , the sample holder, an I-V convertor with gain  $10^5$  and the output connector. As the trapping configuration is designed to allow large currents, the resistance measurement configuration, on the contrary, limits the current via the high ohmic series resistor, to avoid any damaging of the junction. The



**Figure C.3:** Active circuit for room temperature resistance measurement.

corresponding schematic is drawn on Figure C.3. A voltage divider 1:100 is placed, in this configuration, directly after the input in order to allow only very small voltage. Then, assuming that 1 V is applied, the maximum current through the junction is  $10\,\mathrm{nA}$ . The I-V converter is used to increase the signal, in order to facilitate its measurement. A data acquisition program (LabView) was written to control the input (a voltage ramp) and record the output signal.

#### C.1.3 LT Electrical Measurements

The low temperature (LT) measurements were done at 4.2 K in liquid helium. The sample was mounted on a stick and plunged directly into liquid helium. Figure C.4 shows the electronic box at the top of the stick (A) and the sample holder with the electrical connections at the bottom (B). The electronic box is an interface between the measurement apparatus and the sample. It allows two lines for the excitation signal, two lines for the measurement signal and three lines for the temperature reading (a thermometer is fixed on the sample holder).

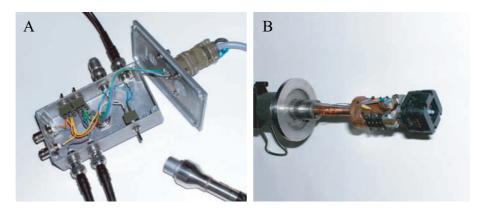


**Figure C.4:** A. Electronic box plugged on the top of the measurement stick. B. Sample holder connected at the bottom of the stick.

In this setup, the dynamic conductance  $(\frac{dI}{dV})$  was recorded. The excitation signal was composed by a ramping dc component and a small fixed ac component. This was achieved by using a 1:4 transformer, as shown in Figure C.5. The other parts of the circuit are similar to the RT circuit. A data acquisition program (LabView) was written to control the input (voltage ramp) and record the output signal and the temperature.

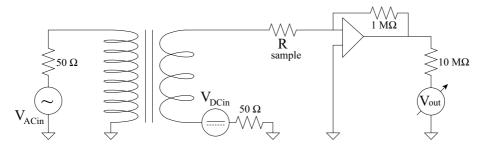
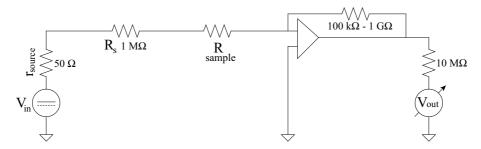


Figure C.5: Active circuit for low temperature resistance measurement, including a 4:1 transformer and an IV converter amplifier (gain  $10^6$ ).

### C.2 2-Dimensional Systems

#### C.2.1 Electrical Measurements

In contrast to 1D system measurements, the samples of the 2D system were not mounted on chip carriers. A needle-prober was used to contact the electrodes corresponding to the considered array (see the electrode configuration on Figure 5.8). Since the resistance of arrays is large and does change dramatically upon exchange manipulations, an I-V converter (DL Instruments, 1212 Current Amplifier) with variable gain  $(10^5-10^9)$  was used to increase the output signal. The corresponding schematic is drawn on Figure C.6. A  $1\,\mathrm{M}\Omega$  series resistor was used for safety. Both input and output signals were processed by a data acquisition (DAC) board (NI BNC-2120). The DAC used could generate up to  $10\,\mathrm{V}$ . A LabView program was used to ramp up and down the input voltage and record the output signal.



**Figure C.6:** Active circuit for array resistance measurement, including an IV converter with variable gain  $(10^5 - 10^9)$ .

In the cases of  $C_{12}$ - and  $C_{16}$ -arrays, however, the maximum gain of

the converter and the DAC sensitivity were not sufficient to measure the current ( $\sim$  pA). An analogue electrometre (HP 4329A high resistance metre) was used to record directly the resistance, via an excitation of 25 V.

#### C.2.2 Optical Measurements

Both types of optical measurements (visible and IR spectroscopies) were performed with setups mainly composed as described in the Figure C.8. A radiation source (UV/vis or IR), via a spectrometre, illuminates the sample, placed perpendicular to the beam. A detector measures the transmitted light, as the wavelength is scanned. The signal is then processed by appropriate electronics. The whole manipulation is interfaced by a computer. In both setups, the measured signal is normalised by the background signal.

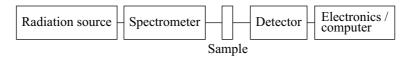


Figure C.7: Typical setup for optical spectroscopy.

As the measurements in the visible were performed in air, the IR measurement were leaded in vacuum  $(2 \,\text{mbar})$ , with a FTIR spectrometre (Bruker IFS  $66 \,\text{v/s}$ ).

For the array measurements (on both setups), a  $CaF_2$  crystal was used as substrate, as it is transparent to UV, visible and IR light. It was then simply placed in the trajectory of the beam\*. In the case of alkane and nanoparticle solutions measurements, a semi-demountable liquid cell was used (see Figure C.9A). The windows used were  $CaF_2$  and the spacing was of  $6\,\mu\text{m}$ . The IR measurement of the OPE molecules was done in a KBr matrix (solid phase). The production of a KBr/OPE pellet was achieved using a manual pressing tool (see Figure C.9B).

<sup>\*</sup> Note that in the case of IR measurements, the beam ( $\sim 0.5\,\mathrm{cm}^2$ ) can be larger than the size of the array ( $\sim 0.4-0.9\,\mathrm{cm}^2$ ).

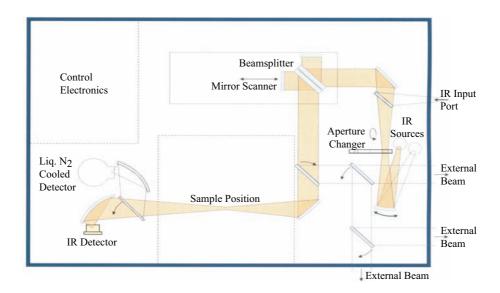


Figure C.8: Schematic of the FTIR spectrometre Bruker IFS 66v/s.

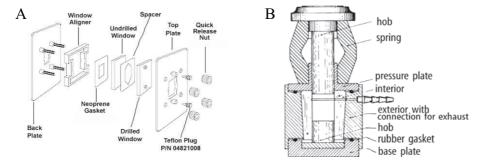


Figure C.9: A. Diagram of an IR semi-demountable liquid cell. B. Diagram of a KBr pressing tool for producing pellets for IR spectroscopy.



### Complementary Experiments

#### D.1 NANOMETRE-SCALE GAP FABRICATION

In a very first approach to the molecule contacting issue, the fabrication of nanometre-scale gap separation in between metallic electrodes has been investigated. This fabrication was based on a two-resist-layers ebeam lithography, providing a 200 nm wide suspended resist bridge by performing an appropriate undercut on the lower resist layer (see Figure D.1). This was followed by a normal evaporation, creating 200 nm-spaced metallic electrodes, as well as two angle evaporations, taking the advantage of the undercut to reduce the gap size.

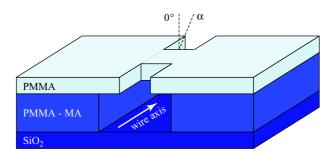


**Figure D.1:** Schematic of the processed 2-resist-layers, ready for angle evaporation. The suspended 200 nm wide resist bridge plays the role of a shadow mask to perform a gap in between the electrodes.

As-prepared electrodes exhibited a separation gap of  $10-20\,\mathrm{nm}$ , as shown in Figure D.2, but with a rather small yield. In very limited cases, gaps with size below  $10\,\mathrm{nm}$  were achieved.

Although this technique allows the fabrication of 20 nm to sub-10 nm gaps in between metallic electrodes, it is rather delicate, time consuming, and does not allow the production of many devices at a time. It is

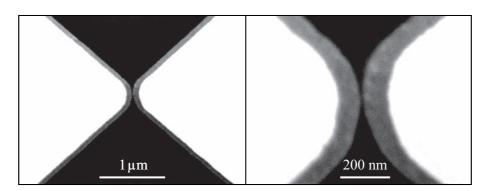


**Figure D.2:** SEM images of a typical gap of 12 nm. The gold electrodes (bright parts) were delimited by the 200 nm resist bridge and prolongated (grey parts) by angle evaporation below the suspended resist bridge.

the reason for finding alternatives, typically the use of nanoparticles, to reduce the size of larger micro-fabricated gaps.

## D.2 ELECTROMIGRATION ON 1D NANOPARTICLE CHAIN

One possibility to use nanoparticle wires for *Molecular Electronics* is to combine them with electromigration, in order to produce nanometre-scale gaps. We briefly investigated this combination, as a possible route to contact single building blocks, or even single molecules.

A nanoparticle chain junction of resistance  $R = 200 \,\Omega$  was used for this experiment. A ramp of current  $I_{EM}$  was applied, from  $25 \,\mu\text{A}$  to  $2.7 \,\text{mA}$ , the point where the junction opened. The conductance was approximately constant up to that point, and then droped rapidly to zero as a gap opened. Figure D.3 presents this process, showing SEM images of the junction before (A) and after (B) the electromigration, and the conductance value versus the increasing current  $I_{EM}$  (C). Remarkably, we observe that the nanoparticles of the chain got strongly fused during the process, which is in good agreement with the trapping experiments at such high currents (see Figure 4.5).

The I-V characteristic of this junction has been taken before and after the electromigration. Figure D.4 reports both measurements: the linear dependence in the initial state (solid line) turns to a highly non-linear dependence after the opening of the junction (dashed line), accompanied

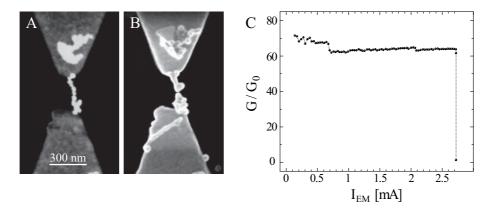
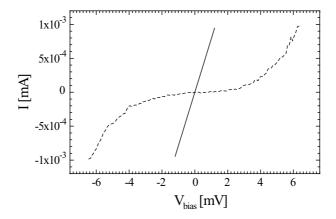


Figure D.3: Electromigration experiment on a nanoparticle chain of initial resistance  $R=200\,\Omega$ . SEM images of the junction before (A) and after (B) the electromigration. C. relative conductance as a function of the applied current  $I_{EM}$  (with  $G_0=2e^2/h$  the quantum conductance). The process stopped as  $I_{EM}$  reached 2.7 mA.



**Figure D.4:** I-V characteristics of the junction at room temperature, before (solid line) and after (dashed line) electromigration.

by a large increase of the resistance. The tunnelling-like shape of this I-V characteristic suggests that a very tiny gap formed, typically of 1-2 nm. Hence, this combined method appears to be a possible way to form nanometre-sized gaps, suitable for small objets contacting.

## D.3 EFFECT OF THF BATH ON AS-PREPARED ARRAYS

As a control experiment for the molecular place-exchange, we performed an immersion of  $C_8$ -arrays in THF at RT for 24 hours, i.e. in the same condition as for a real molecular exchange, but without any *active molecules* in the solvent. The goal was to check that without incoming molecules, the alkanes immobilised on the nanoparticles would not spontaneously desorb into the solvent.

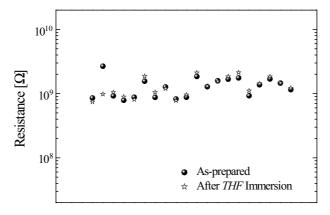


**Figure D.5:** Resistance of several  $C_8$ -arrays, as-prepared and after immersing in THF without *active molecules* and under same conditions as for molecular place-exchange.

Figure D.5 shows the resistance of several  $C_8$ -arrays measured before (dots) and after immersion (stars). Clearly, no change in the average resistance value occurred, suggesting that immersion in the solvent alone does not perturb the arrays. This is an evidence of the good stability of the arrays. Indeed, in the case of desorption of the alkanes, we would have observed a decrease of resistance due to the aggregation of the nanoparticles, free to move with poor alkane coverage (see typical aggregation in Appendix B.3.5). Furthermore, it confirms the associative character of the place-exchange, as depicted by Murray  $et\ al^{130}$ , saying that the infiltration of incoming molecules in the alkane SAM is needed to induce the desorption of the immobilised alkanes.

## D.4 EFFECT OF MOLECULAR EXCHANGE ON THE NANOPARTICLES

As a control experiment, we performed successive molecular exchanges of  $C_8$ -arrays with  $C_8$  active molecules, at RT for 24 hours each (see Figure D.6). The aim was to identify wether leaving molecules from the nanoparticle etch gold from the nanoparticles or not.

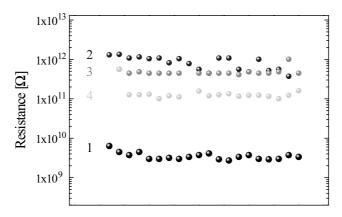


Figure D.6: Resistance of several  $C_8$ -arrays on one chip, (1) as-prepared, (2) after first  $C_8$ -exchange, (3) after second  $C_8$ -exchange and (4) after third  $C_8$ -exchange.

After the first exchange (2), we observe a large increase of the resistance. This can be attributed to the reorganisation of the surface into regular sphere (see discussion in Section 7.2). Then random fluctuations are observed for the following exchanges. Because the resistance does not keep increasing with further exchange procedures, we conclude that there is no gold etching of the nanoparticles.

## D.5 VISIBLE ABSORPTION OF COLLOIDAL SOLUTIONS

To ensure that the colloidal solutions used for the visible absorption study are diluted enough to prevent from particle-particle interaction, we performed measurements for different concentrations of the colloidal solutions (listed in Appendix E.2, Table E.7).  $C_8$ ,  $C_{12}$  and  $C_{16}$ -capped nanoparticle solutions exhibited the same behaviour: no relevant shift of the SPR was observed between the as-prepared solution, the 1:1 di-

lution in chloroform and the 1:3 dilution in chloroform (see Figure D.7). Indeed, if any particle-particle interaction would take place, a shift of the SPR would be visible, according to the effective medium theory (see Section 7.1).

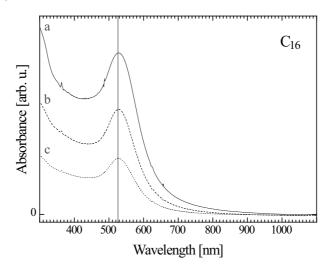


**Figure D.7:** Visible absorption spectra of  $C_{16}$ -capped nanoparticle solution at different concentrations. a. As prepared; b. 1:1 dilution in chloroform; c. 1:3 dilution in chloroform. The surface plasmon resonance is at 526 nm for all concentrations.

### D.6 ESTIMATION OF THE SOLVENT/SUBSTRATE INFLUENCE ON THE SPR

To solve the question of the substrate influence on the SPR in the arrays, visible spectroscopy measurements were led on various nanoparticle solutions (listed in Appendix E.2, Table E.7). In principle, the influence of the particle surrounding can be demonstrated by comparing the SPR positions of solutions containing similar nanoparticles in different solvent\*. Here, we chose to compare nanoparticles in ethanol and in chloroform, as these solvents have a large difference in their respective permittivities ( $\varepsilon_{ethanol} = 24.3$ ,  $\varepsilon_{chloroform} = 4.8$ ).

Figure D.8 displays the spectra of two  $C_8$ -capped nanoparticle solutions, diluted in ethanol (a) and in chloroform (b). One sees that the

<sup>\*</sup> We consider here the nanoparticles in a shell model, i.e. made of a core (Au) and a shell  $(C_n)$ .

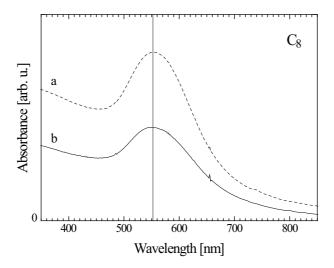


Figure D.8: Visible absorption spectra of  $C_8$ -capped nanoparticles in two different solvents (solution): a. ethanol ( $\varepsilon_{ethanol} = 24.3$ ); b. chloroform ( $\varepsilon_{chloroform} = 4.8$ ). The surface plasmon resonance is in both cases at 553 nm.

SPR does not undergo any shift, despite the large difference in the solvent permittivity. This strongly suggests that the influence of the solvent, for nanoparticles in solution, is negligible. We can speculate from this observation that, in the 2D array geometry, the substrate also has little or no influence.

## D.7 VISIBLE ABSORPTION ON SMALL SELECTED AREAS OF ARRAY

In order to check the effect of the defects present in the large area arrays (1 cm<sup>2</sup>), we performed a similar study on selected  $10 \times 10 \,\mu\text{m}^2$  areas presenting a defect-less packing (selected after SEM observation)\*†. The Figure D.9 reports our observations. On the left, one can see typical transmission spectra taken at a specific selected area of  $C_8$ -capped nanoparticle array as prepared (black), after OPE-exchange (blue), after  $C_8$  back-exchange (grey) and after second OPE-exchange (light blue). A 10 nm-red shift of the surface plasmon resonance is observed after OPE-

<sup>\*</sup> These measurements have been done in collaboration with P. Müschlegen and J. Farahani, Physics Institute, University of Basel.

<sup>&</sup>lt;sup>†</sup> All measurements are reported in Appendix E.2, Table E.5.

exchanges. After  $C_8$  back-exchanges, the SPR recovers its initial position. After 6 consecutive exchanges, one could still observe a good superposition of the  $C_8$  spectra, as well as the OPE spectra, evidence for a good reversibility. On the right, a small statistic on 8 selected areas is presented. They all exhibit the same behaviour, confirming the reproducibility of the exchange. The shifts observed with this experiment are similar to those observed on larger areas. However, the initial SPR was found to occur at a larger wavelength (634 nm instead of 613 nm). This can be the result of the better ordering and defect-free character of the arrays within the small selected areas. Further independent measurements with a different optical setup led to the same observation.

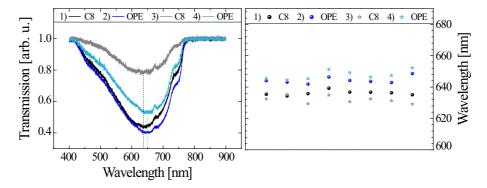
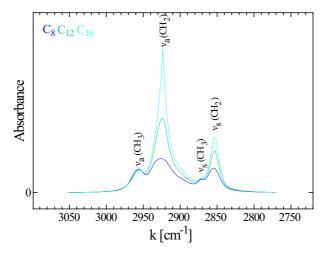


Figure D.9: Left: Visible transmission spectra of a selected area of  $C_8$ -capped nanoparticle array: as prepared (black), after OPE exchange (blue), after  $C_8$  back exchange (grey) and after second OPE exchange (cyan). A red shift of the surface plasmon resonance is observed after both OPE exchanges, from 634 nm to 644 nm. Right: Statistic on 8 selected areas, all exhibiting the same behaviour.

Note that the features and the intensities of the spectra are irrelevant here, since they come from irregularities of the light source. Indeed, these measurements have been performed with a different setup than the "large area" measurements, because of the need to illuminate only a well defined small area. Note finally that the areas selected for this study were also investigated electrically and correspond to 8 of the junctions presented in Figure 6.1.

### D.8 IR Absorption of Alkane Chains

The IR spectra of pure  $C_8$ ,  $C_{12}$  and  $C_{16}$  have been measured, in order to allow the comparison with the spectra of the arrays. However, one can also compare the three alkane spectra to check the assessment that the intensity proportion between  $CH_3$  and  $CH_2$  should depend on the length of the alkane. Indeed, the three of those molecules are very similar and differ only in the number of methylene groups  $(CH_2)$ . Apart from these groups, they only contain one thiol group (S) and one methyl group  $(CH_3)$ . Hence, the ratio  $CH_3/CH_2$  should be 1/7 for  $C_8$ , 1/11 for  $C_{12}$  and 1/15 for  $C_{16}$ .



**Figure D.10:** Infrared spectra of  $C_8$ ,  $C_{12}$  and  $C_{16}$  in the region of the  $CH_3$  and  $CH_2$  stretching vibration resonances. a and s denote the asymmetric and symmetric resonances, respectively.

Inspecting Figure D.10, one can see that the ratios of the respective intensities follow this trend: as the three alkanes exhibit the same  $CH_3$  intensity, the  $CH_2$  intensities strongly differ with the number of  $CH_2$  groups. From a multi-peaks fitting, we could extract the surface area of each peak. We found 49.6/72.3/90.0 for the  $CH_2(\nu_a)$  of  $C_8$ ,  $C_{12}$  and  $C_{16}$ , respectively, what is very similar to the expected ratios 7/11/15. Note that for evident reason of accuracy, only the well defined asymmetric stretching vibrations peaks were taken into account to perform this comparison.

#### D.9 ENERGY SHIFT CORRECTION IN XPS ANALYSIS

To allow the comparison of various sample spectra, the signals were adjusted in two ways: an energy shift and a normalisation. First, the samples were charged during the X-ray irradiation process. Hence, the measured binding energy shifted by a constant value during the time interval. The relative shifts between the measurements were determined by the observation of the valence spectra and corrected as following: (1) reference, (2)  $-0.2\,\mathrm{eV}$  and (3)  $-0.9\,\mathrm{eV}$ , as shown in Figure D.11. Second, the three stages of exchange were measured on three different samples, and the samples had to be loaded one after the other in the setup and positioned separately. The signal intensity could vary from one measurement to the other. Each spectrum has been normalised according to the Au feature, which is not supposed to change upon exchange. Then both adjustments were performed on the full spectra (see Appendix E.2).

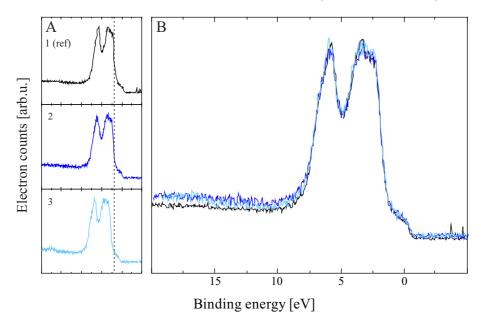


**Figure D.11:** A. Valence electrons peak for the three stages: as prepared (1), after OPE exchange (2) and after  $C_8$  back exchange (3). B. Relative corrections of the sample charging: 1. reference, 2. -0.2 eV and 3. -0.9 eV. Note that the intensities were also normalised.



# CATALOGUE OF SAMPLES

### E.1 1-DIMENSIONAL SYSTEMS

The Table E.1 reports all the measurements related to the formation of a nanoparticle bridge between prefabricated electrodes (Chapter 3 & 4). The trapping parameters V and  $R_s$  are reported, as well as the characteristic times  $t_1$  and  $t_2$ , the maximum power  $P_{max}$  and the final junction resistance R.

Sample	$d[\mathrm{nm}]$	$V\left[ \mathrm{V}\right]$	$R_s\left[\Omega\right]$	$P_{max} [\mathrm{mW}]$	$t_1[s]$	$t_2 \left[ \mu \mathrm{s} \right]$	$R\left[\Omega\right]$
lae3.3 12 .2	80	1.8	820	3.43		3	1.9e3
lae 3.3 12 .10	30	1.8	820	3.43		15	4.8e3
lae 3.3 12 .12	100	2	300	7.04		1	319
lae 3.3 12 .13	100	2	300	6.75		1	86
lae 3.3 12 .14	110	2	820	4.24		1	3.1e3
laeP3.2 4.7	40	1.8	100	8.40			142
$lae 3.3 \ 13 \ .9$	100	2	470				$> 1\mathrm{G}$
$lae 3.3 \ 13 \ .10$	100	2	820				$> 1\mathrm{G}$
lae $3.3\ 13\ .11$ b	10	1	100				$> 1\mathrm{G}$
lae $3.3\ 13\ .13$ b	25	1	470				$> 1\mathrm{G}$
laeP3.2 3.9	50	1	470				2.0e8
$laeP3.2\ 3.10$	35	1	820				$> 1\mathrm{G}$
laeP3.2 3.2b	40	1	300				2.6e3
laeP3.2 3.3b	40	1	470				1.8e3
laeP3.2 3.15d	100	3.5	100				470
lae 3.4 23 .2	40	1	100	2.61	0.5	1	152
lae 3.4 23 .11	40	1	470	1.38	32	6	790
				(	Continu	ed on ne	xt page

Sample	$d[\mathrm{nm}]$	$V\left[ \mathbf{V}\right]$	$R_s\left[\Omega\right]$	$P_{max} [\mathrm{mW}]$	$t_1[s]$	$t_{2}\left[\mu\mathrm{s}\right]$	$R\left[\Omega\right]$	
lae3.4 23 .12	20	1	100	10.0			2.0e8	
lae3.4 23 .13	20	1	470	5.41	0		269	
lae3.4 23 .14	20	1	820		0		245	
lae3.4 24 .6	80	2	100		1		52	
lae3.4 24 .7	70	2	470	1.34	0.1	1	166	
lae3.4 24 .9	15	1	100	2.73	2		1.5e3	
lae3.4 24 .10	15	1	470	0.70			4e3	
lae3.4 24 .11	50	1	470	4.52	3.5	1	304	
lae2.3 19 .6	50	1	100	2.64	1	2	250	
lae2.3 19 .8	20	0.5	100	2.71	24	1	345	
$laeP3.1 \ 13.2$	60	1.3	100	2.71	45		195	
laeP3.1 13.3	80	1.6	820	0.52	4		1.6e3	
laeP3.1 13.4	90	1.6	820	4.90	13		7.8e3	
laeP3.1 13.9	70	1.3	100	6.58	2		1.3e3	
laeP3.1 13.10	80	1.6	100	1.03	8		81	
$laeP3.1\ 25.12$	80	1	820	1.03	9		813	
$laeP3.1\ 19.2$	50	1	820	1.03	6		862	
laeP3.1 19.8	40	1	820	9.25	26		769	
laeP3.1 19.11	200	3	820	9.25	1		412	
laeP3.1 19.12	160	3	820	1.03	0.2		534	
laeP3.1 22.6	120	1	820	1.03	11		614	
laeP3.1 22.7	90	1	820	4.11	5		640	
laeP3.1 22.12	200	1	820	1.03	3		730	
laeP3.1 22.13	180	1	820	1.03	2		730	
laeP3.1 22.14	160	2	820	4.11	0		701	
$laeP3.1\ 22.15$	160	1	820	1.02	6.5		682	
$laeP3.1\ 11.2$	200	1	820	1.02	1.7		309	
$laeP3.1 \ 11.3$	200	1.5	820	2.31	2	1	462	
$laeP3.1\ 11.4$	200	2	820	4.07	0.2	1	315	
$laeP3.1 \ 11.6$	270	2	100	10.0	0		146	
$laeP3.1\ 11.7$	270	2	100	10.6			174	
$laeP3.1 \ 11.8$	250	2	820	4.07	0.5		491	
laeP3.1 11.9	300	2	820	4.11	3		2.1e3	
laeP3.1 11.1b	200	1	820	1.03	24		606	
laeP3.1 11.7b	180	1.5	820	2.29	6.5	1	434	
laeP3.1 11.8b	190	1.5	100	6.27	1.5	2	375	
laeP3.1 11.9b	100	1.5	100	6.27	2		317	
$laeP3.1 \ 11.10b$	300	1.5	820	2.29			587	
laeP3.1 20.1	50	0.5	1000	0.23	9		340	
Continued on next page								

Sample	$d[\mathrm{nm}]$	V[V]	$R_s\left[\Omega\right]$	$P_{max} [\mathrm{mW}]$	$t_1[s]$	$t_2 \left[ \mu \mathrm{s} \right]$	$R\left[\Omega\right]$
$laeP3.1\ 20.6$	60	0.5	1000	0.23	7.5	1	266
$laeP3.1\ 20.7$	40	0.5	1000	0.23	8		432
$laeP3.1\ 20.8$	30	0.5	1000	0.23	69	1	592
$laeP3.1\ 20.11$	180	1	1000	0.93		1	228
$laeP3.1\ 20.12$	150	1	1000	0.93	2.5	1	209
$laeP3.1\ 20.13$	180	1	1000	0.93	1	1	442
$laeP3.1\ 20.14$	130	1	1000	0.93	3.5	1	360
$laeP3.1\ 20.15$	120	1	1000	0.93	5		992
laeP3.1 24.2	150	1	820	1.03	0.6		554
laeP3.1 24.3	200	1	820	1.02	6.5	1	550
laeP3.1 24.4	160	1	820	1.02	9	1	455
laeP3.1 24.6	140	1	820	1.06			1.2e4
laeP3.1 24.7	120	1	820	1.02	1.2	2	250
$laeP3.1\ 21.4$	150	1	820	1.03	4.5	1	569
$laeP3.1\ 21.5$	90	1	820	1.03	25	1	557
$laeP3.1\ 21.9$	140	1	820	1.03	15		365
laeP3.1 21.10	160	1	820	1.03	32	1	664

Table E.1: Measurements related to the trapping experiments: with d the electrodes' spacing, V the applied voltage,  $R_s$  the series resistance,  $P_{max}$  the maximum power through the junction,  $t_1$  the trapping time (first process),  $t_2$  the contacting time (second process) and R the final junction's resistance. The resistances noted as > 1G were to high to be measurement with the setup. The resistances in italic were taken after the trapping experiment when the record could not be done during the experiment.

#### E.2 2-DIMENSIONAL SYSTEMS

Here are listed all the measurements performed on 2D nanoparticle arrays, referring to Chapters 5, 6 and 7. While Tables E.2 and E.3 report the electrical measurements, Tables E.4, E.5, E.6, E.7 and Figures E.1, E.2 and E.3 summarise the optical measurements.

We distinguish, for the electrical measurements, the experiments done with OPE-exchanges (Table E.2) to those done with OPV-exchanges (Table E.3). In both cases, we reported for each chip-sample the number of junctions considered, the mean sheet resistance\* of the array as-

<sup>\*</sup> The sheet resistance is defined by  $R_{\square} = R \cdot \frac{w}{d}$ , with w and d the width and length of the array respectively.

prepared (mean value over all junctions), the mean sheet resistance after molecular exchange, and the ratio. We also separated the results into the categories  $C_8$ ,  $C_{12}$  and  $C_{16}$ , corresponding to the ligand-capping of the nanoparticles composing the arrays.

Sample	Number of	Alkane-state	OPE-state	Ratio
	junctions	resistance	resistance	
Ar 29.2	30	$2.5~\mathrm{G}\Omega$	$220~\mathrm{M}\Omega$	11
C Ar 33.1	17	$0.2~\mathrm{G}\Omega$	$16 M\Omega$	13
$C_8$ Ar 33.2	51	$4.6~\mathrm{G}\Omega$	$430~\mathrm{M}\Omega$	11
Ar 56.1	58	$73  \mathrm{G}\Omega$	$110~\mathrm{M}\Omega$	664
Ar 34.1	68	$850  \mathrm{G}\Omega$	$0.12\mathrm{G}\Omega$	7083
Ar 34.2	38	$870~\mathrm{G}\Omega$	$0.4~\mathrm{G}\Omega$	2175
Ar 38.1	57	$90 \text{ G}\Omega$	$47~\mathrm{G}\Omega$	2
$C_{12} \frac{\mathbf{Ar}}{\mathbf{Ar}} 52.4$	65	$1600\mathrm{G}\Omega$	$0.14\mathrm{G}\Omega$	11429
Ar 54.1	57	$1000\mathrm{G}\Omega$	$1.7~\mathrm{G}\Omega$	588
Ar 54.2	20	$580  \mathrm{G}\Omega$	$12 \text{ G}\Omega$	48
Ar 50.1	97	$7 \text{ T}\Omega$	$160  \mathrm{G}\Omega$	44
$C_{16} \mathbf{Ar} 50.2$	44	$36 \text{ T}\Omega$	-	-
Ar 62.1	100	$3 \text{ T}\Omega$	$4~\mathrm{G}\Omega$	750

**Table E.2:** Summary of electrical measurements performed on  $C_n$ -arrays for the OPE exchange. The substrate used was undoped  $Si/SiO_2$ , excepted for the sample Ar 29.2, which was deposited on thin glass. The resistances given here are the sheet resistances.

Sample	Number of junctions	Alkane-state resistance	OPV-state resistance	Ratio
$C_8$ <b>Ar 61.1</b>	58	$17  \mathrm{G}\Omega$	$4.2\mathrm{G}\Omega$	4.0
$C_{12} rac{{f Ar}}{{f Ar}} rac{{f 52.1}}{{f 60.1}}$	81	$100\mathrm{G}\Omega$	$30 \text{ G}\Omega$	3.3
$^{\mathrm{C}_{12}}$ Ar 60.1	90	$140\mathrm{G}\Omega$	$52~\mathrm{G}\Omega$	2.7

**Table E.3:** Summary of electrical measurements performed on  $C_n$ -arrays for the OPV exchanges. The substrate used was undoped  $Si/SiO_2$ . The resistances given here are the sheet resistances.

As for the optical measurements, both visible and IR spectroscopies have been performed with the same samples: large homogeneous arrays deposited on  $CaF_2$  substrates. Indeed, no prerequisite structure of the array was necessary for these measurements, since the absorption signal was taken through a large area ( $\sim$ mm<sup>2</sup>). Table E.4 lists these samples

and their surface plasmon resonance (SPR). The corresponding spectra are shown in Figure E.1. For the samples with which an OPE-exchange was performed, we reported as well the SPR after the exchange and the red shift with respect to the as-prepared SPR. The optical measurements on small selected areas have been performed on striped arrays (with gold pads) and are summarised in Table E.5.

Sample	SPR in alkane-state	SPR in $OPE$ -state	Shift
S1	$609.5\mathrm{nm}$		
S2	$605.1\mathrm{nm}$		
$C_8$ S3	$613.1\mathrm{nm}$	$635.4\mathrm{nm}$	$22.3\mathrm{nm}$
S4	$617.3\mathrm{nm}$		
S5	$593.5\mathrm{nm}$	$602.3\mathrm{nm}$	$8.8\mathrm{nm}$
S1	$590.7\mathrm{nm}$		
S2	$590.4\mathrm{nm}$		
$C_{12}$ <b>S3</b>	$595.4\mathrm{nm}$	$608.1\mathrm{nm}$	$12.7\mathrm{nm}$
S4	$587.6\mathrm{nm}$		
S5	$583.0\mathrm{nm}$	$585.4\mathrm{nm}$	$2.4\mathrm{nm}$
S2	$583.0\mathrm{nm}$		
$C_{16}$ <b>S4</b>	$584.2\mathrm{nm}$		
S5	$583.2\mathrm{nm}$	$589.3\mathrm{nm}$	$6.1\mathrm{nm}$

**Table E.4:** Summary of UV/vis measurements performed on  $C_n$ -arrays on  $CaF_2$  crystal for the OPE exchange. The average shift is 10.5 nm.

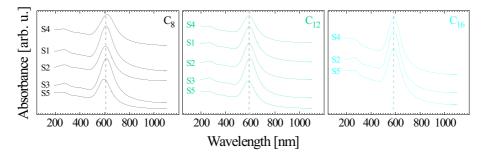


**Figure E.1:** Optical measurements performed On  $C_8$ ,  $C_{12}$ , and  $C_{16}$ -arrays (deposited on  $CaF_2$  crystal substrate). The curves were shifted for clarity.

Sample	SPR in alkane-state	SPR in $OPE$ -state	Shift
<b>Ar 29.2</b> 0814	$626.2\mathrm{nm}$	$647.3\mathrm{nm}$	$21.1\mathrm{nm}$
<b>Ar 29.2</b> 0817	$628.7\mathrm{nm}$	$650.2\mathrm{nm}$	$21.5\mathrm{nm}$
<b>Ar 29.2</b> 0818	$627.5\mathrm{nm}$	$644.5\mathrm{nm}$	$17.0\mathrm{nm}$
<b>Ar 29.2</b> 0915	$632.4\mathrm{nm}$	$644.1\mathrm{nm}$	$11.7\mathrm{nm}$
<b>Ar 29.2</b> 0916	$635.3\mathrm{nm}$	$643.1\mathrm{nm}$	$7.9\mathrm{nm}$
<b>Ar 29.2</b> 0917	$629.4\mathrm{nm}$	$641.9\mathrm{nm}$	$12.5\mathrm{nm}$
<b>Ar 29.2</b> 1009	$634.9\mathrm{nm}$	$646.4\mathrm{nm}$	$11.5\mathrm{nm}$
<b>Ar 29.2</b> 1012	$630.7\mathrm{nm}$	$644.2\mathrm{nm}$	$13.6\mathrm{nm}$
<b>Ar 29.2</b> 1015	$632.4\mathrm{nm}$	$643.6\mathrm{nm}$	$11.2\mathrm{nm}$
<b>Ar 29.2</b> 1016	$631.3\mathrm{nm}$	$642.9\mathrm{nm}$	$11.6\mathrm{nm}$
<b>Ar 29.2</b> 1017	$629.1\mathrm{nm}$	$648.6\mathrm{nm}$	$19.5\mathrm{nm}$
<b>Ar 29.2</b> 1208	$632.6\mathrm{nm}$	$644.8\mathrm{nm}$	$12.3\mathrm{nm}$
<b>Ar 29.2</b> 1210	$632.0\mathrm{nm}$	$641.9\mathrm{nm}$	$10.0\mathrm{nm}$
<b>Ar 29.2</b> 1212	$631.7\mathrm{nm}$	$641.5\mathrm{nm}$	$9.8\mathrm{nm}$

**Table E.5:** Summary of optical measurements performed on small areas  $C_8$ -arrays for the OPE exchange. Thin glass was used as substrate. The average shift is  $13.6\,\mathrm{nm}$ .

Sample	$1^{st}$ exchange % (1) to (2)	$2^{nd}$ exchange % (3) to (4)	$C_n(1)$ to $C_n(3)$ %
$_{C}$ S3	3.0%	39.0%	103.0%
$C_8$ S5	31.0%		71.6%
S2	54.8%		
$_{C}$ S3	22.9%	37.7%	70.0%
$C_{12}$ <b>S4</b>	40.4%		
S5	33.1%		78.5%
S2	34.6%		
$C_{16}$ <b>S4</b>	52.5%		
S5	39.3%		63.6%

**Table E.6:** Summary of IR measurements performed on  $C_n$ -arrays on  $CaF_2$  for the OPE exchange  $((1) \rightarrow (2), \rightarrow (3), \rightarrow (4))$ . The average exchange percentage from  $C_n$  to OPE is 35.3%.

IR spectra are shown in Figure E.2 and listed in Table E.6. This table reports the percentages of exchange of the different arrays, calculated via the comparison of the alkane  $CH_2(\nu_a)$  peak intensities before (1) and after exchange with OPE (2). When the back exchange could be performed (3), we also compared the  $C_n$  intensities versus the as-prepared state. Note that for a repeated exchange to OPE (4), the exchange percentage might change.

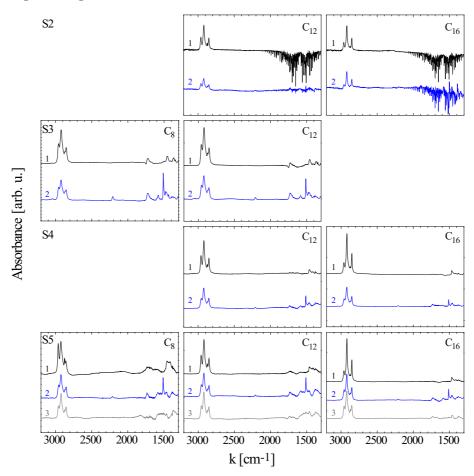


Figure E.2: IR measurements performed On  $C_8$ ,  $C_{12}$ , and  $C_{16}$ -arrays (on  $CaF_2$ ), for the three stages of exchange: (1) as-prepared, (2) after OPE-exchange and (3) after back-exchange. The curves were shifted for clarity (but not normalised).

Table E.7 lists the optical (visible) experiments done as control experiments on nanoparticle solutions, where water, ethanol and chloroform

have bee	n considered	and	. compared*	ķ •
----------	--------------	-----	-------------	--------

	Sample	$ ho_{rel}$	solvent	SPR
no	S6(1)	1	DI water	$517.1\mathrm{nm}$
no	S6(2)	1	ethanol	$523.6\mathrm{nm}$
	S5C83D1	1	$\operatorname{chloroform}$	$549.6\mathrm{nm}$
	S5C83D2	1/2	$\operatorname{chloroform}$	$548.7\mathrm{nm}$
$C_8$	S5C83D3	1/4	$\operatorname{chloroform}$	$550.0\mathrm{nm}$
	S6C8(4)	1	ethanol	$554.1\mathrm{nm}$
	S6C8(7)	1	$\operatorname{chloroform}$	$551.6\mathrm{nm}$
	S5C123D1	1	$\operatorname{chloroform}$	$521.9\mathrm{nm}$
	S5C123D2	1/2	$\operatorname{chloroform}$	$522.0\mathrm{nm}$
$C_{12}$	S5C123D3	1/4	$\operatorname{chloroform}$	$522.0\mathrm{nm}$
	S6C12(5)	1	ethanol	$549.4\mathrm{nm}$
	S6C12(8)	1	$\operatorname{chloroform}$	$537.3\mathrm{nm}$
	S5C163D1	1	$\operatorname{chloroform}$	$526.2\mathrm{nm}$
	S5C163D2	1/2	$\operatorname{chloroform}$	$526.0\mathrm{nm}$
$C_{16}$	S5C163D3	1/4	$\operatorname{chloroform}$	$525.8\mathrm{nm}$
	S6C16(6)	1	ethanol	$548.8\mathrm{nm}$
	S6C16(9)	1	chloroform	$525.7\mathrm{nm}$

**Table E.7:** Summary of optical measurements performed on  $C_n$ -capped nanoparticles in solution.

Two series of XPS measurements have been performed by P. Morf (PSI), on  $C_8$ -arrays, for the three stages : as-prepared, after OPE-exchange and after back-exchange. Figure E.3 displays the full spectra of the second series (used in Section 7.3). The relevant peaks (O1s, C1s, S2p $\frac{1}{2}$  and 2p $\frac{3}{2}$ , Si2s and valence) are zoomed in.

<sup>\*</sup> Note that the respective permittivities are :  $\varepsilon_{H_2O}=78.5,\ \varepsilon_{C_2H_6O}=24.3$  and  $\varepsilon_{CHCl_3}=4.8.$ 

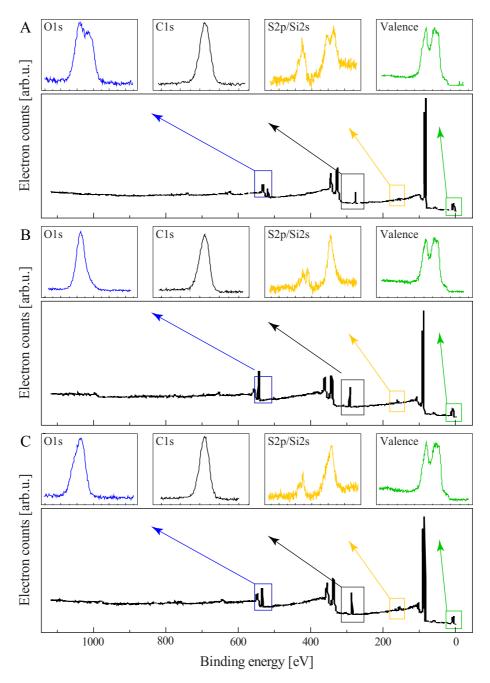


**Figure E.3:** Full XPS spectrum of a  $C_8$  array : A. as-prepared, B. after OPE-exchange, C. after back-exchange. The relevant signals, O1s, C1s, S2p, Si2s and valence are zoomed in.

- [1] J. Bardeen and W.H. Brattain, *The transistor, a semi-conductor triode*, Phys. Rev. **74** (1948), 230–231.
- [2] I.M. Ross, *The foundation of the silicon age*, Bell Labs Tech. J. **2** (1977), no. 4, 3–14.
- [3] B. Doyle, R. Arghavani, D. Barrage, S. Datta, M. Doczy, J. Kavalieros, A. Murthy, and R. Chau, *Transistor elements for 30nm physical gate lengths and beyond*, Intel Technol. J. **6** (2002), no. 2, 42–54.
- [4] S. Iijima, Helical microtubules of graphitic carbon, Nature **354** (1991), 56.
- [5] S.J. Wind, J. Appenzeller, R. Martel, V. Derycke, and Ph. Avouris, Vertical scaling of carbon nanotube field-effect transistors using top gate electrodes, Appl. Phys. Lett. 80 (2002), 3817–3819.
- [6] J.M. Tour, Molecular electronics. synthesis and testing of components, Acc. Chem. Res. **33** (2000), 791–804.
- [7] H. Kuhn and D. Möbius, Systems of monomolecular layers assembling and physico-chemical behavior, Angew. Chem. Int. Ed. 10 (1971), no. 9, 620–637.
- [8] A. Aviram and M.A. Ratner, *Molecular rectifiers*, Chem. Phys. Lett. **29** (1974), 277–283.
- [9] J.R. Heath and M.A. Ratner, *Molecular electronics*, Phys. Today **56** (2003), 43–49.
- [10] J. Chen, M.A. Reed, A.M. Rawlett, and J.M. Tour, Large on-off ratios and negative differential resistance in a molecular electronic device, Science 286 (1999), 1550–1552.

[11] C. Joachim, J.K. Gimzewski, and A. Ariram, Electronics using hybrid-molecular and mono-molecular devices, Nature 408 (2000), 541–548.

- [12] J.K. Gimzewski, E. Stoll, and R.R. Schlittler, Scanning tunneling microscopy of individual molecules of copper phthalocyanine adsorbed on polycrystalline silver surfaces, Surf. Sci. 181 (1987), 267–277.
- [13] P.S. Weiss, L.A. Bumm, T.D. Dunbar, T.P. Burgin, J.M. Tour, and D.L. Allara, Probing electronic properties of conjugated and saturated molecules in self-assembled monolayers, Ann. N.Y. Acad. Sci. 852 (1998), 145.
- [14] W. Haiss, C. Wang, I. Grace, A.S. Batsanov, D.J. Schiffrin, S.J. Higgins, M.R. Bryce, C.J. Lambert, and R.J. Nichols, *Precision control of single-molecule electrical junctions*, Nature Materials 5 (2006), 995–1002.
- [15] M.A. Reed, C. Zhou, C.J. Muller, T.P. Burgin, and J.M. Tour, Conductance of a molecular junction, Science 278 (1997), 252–254.
- [16] B.Q. Xu and N.J.J. Tao, Measurement of single-molecule resistance by repeated formation of molecular junctions, Science 301 (2003), no. 5637, 1221–1223.
- [17] J.R. Heath, P.J. Kuekes, G.S. Snider, and R.S. Williams, A defect-tolerant computer architecture: opportunities for nanotechnology, Science **280** (1998), no. 5370, 1716–1721.
- [18] J.G. Kushmerick, J. Naciri, J.C. Yang, and R. Shashidhar, Metal-molecule contacts and charge transport across monomolecular layers: measurement and theory, Phys. Rev. Lett. 89 (2002), 086802.
- [19] H.B. Akkerman, P.W.M. Blom, D.M. de Leeuw, and B. de Boer, Towards molecular electronics with large-area molecular junctions, Nature 441 (2006), 69–72.
- [20] W. Liang, M.P. Shores, M. Bockrath, J.R. Long, and H. Park, Kondo resonance in a single-molecule transistor, Nature 417 (2002), 725–729.

[21] J. Park, A. N. Pasupathy, J. I. Goldsmith, C. Chang, Y. Yaish, J. R. Petta, M. Rinkoski, J. P. Sethna, H. D. Abrua, P. L. McEuen, and D. C. Ralph, Coulomb blockade and the Kondo effect in single-atom transistors, Nature 417 (2002), 722–725.

- [22] R.E. Holmlin, R. Haag, M.L. Chabinyc, R.F Ismagilov, A.E. Cohen, A. Terfort, M.A. Rampi, and G.M. Whitesides, *Electron transport* through thin organic films in metal-insulator-metal junctions based on self-assembled monolayers, J. Am. Chem. Soc. 123 (2001), 5075– 5085.
- [23] R.L. McCreery, Molecular electronic junctions, Chem. Mater. 16 (2004), 4477–4496.
- [24] R.L. Carroll and C.B. Gorman, The genesis of molecular electronics, Angew. Chem. Int. Ed. 41 (2002), 4378–4400.
- [25] N.J. Tao, Electron transport in molecular junctions, Nature Nanotechnology 1 (2006), 173–181.
- [26] J.G. Kushmerick, A.S. Blum, and D.P. Long, *Metrology for molecular electronics*, Anal. Chimica Acta **568** (2006), 20–27.
- [27] A. Nitzan and M.A. Ratner, Electron transport in molecular wire junctions, Science **300** (2003), 1384–1389.
- [28] Y. Chen, G.Y. Jung, D.A.A. Ohlberg, X.M. Li, D.R. Stewart, J.O. Jeppesen, K.A. Nielsen, J.F. Stoddart, and R.S. Williams, Nanoscale molecular-switch crossbar circuits, Nanotechnology 14 (2003), 462–468.
- [29] D.L. Feldheim and C.D. Keating, Self-assembly of single electron transistors and related devices, Chem. Soc. Rev. 27 (1998), 1–12.
- [30] W.P. Mc Connell, J.P. Novak, L.C. Brousseau III, R.R. Fuierer, R.C. Tenent, and D.L. Feldheim, Electronic and optical properties of chemically modified metal nanoparticles and molecularly bridged nanoparticle arrays, J. Phys. Chem. B 104 (2000), 8925–8930.
- [31] I. Amlani, A.M. Rawlett, L.A. Nagahara, and R.K. Tsui, An approach to transport measurements of electronic molecules, Appl. Phys. Lett. 80 (2002), 2761–2763.

[32] AS.I. Khondaker and Z. Yao, Fabrication of nanometer-spaced electrodes using gold nanoparticles, Appl. Phys. Lett. 81 (2002), 4613–4615.

- [33] R.P. Andres, J.D. Bielefeld, J.I. Henderson, D.B. Janes, V.R. Kolagunta, C.P. Kubiak, W.J. Mahoney, and R.G. Osifchin, Self-assembly of a two-dimensional superlattice of molecularly linked metal clusters, Science 273 (1996), 1690–1693.
- [34] T. Dadosh, Measurement of the conductance of single conjugated molecules, Nature 436 (2005), 677–680.
- [35] C. Xu, H. van Zalinge, J.L. Pearson, A. Glidle, J.M. Cooper, D.R.S. Cumming, W. Haiss, J.L. Yao, D.J. Schiffrin, M. Proupín-Pérez, R. Cosstick, and R.J. Nichols, A combined top-down bottom-up approach for introducing nanoparticle networks into nanoelectrode gaps, Nanotechnology 17 (2006), 3333–3339.
- [36] B.J. van Wees, H. van Houten, C.W.J. Beenakker, J.G. Williamson, L.P. Kouwenhoven, and D. van der Marel, Quantized conductance of point contacts in a two-dimensional electron gas, Phys. Rev. Lett. 60 (1988), 848–850.
- [37] D.A. Wharam, T.J. Thornton, R. Newbury, M. Pepper, H. Ahmed, J.E.F. Frost, D.G. Hasko, D.C. Peacockt, D.A. Ritchie, and G.A.C. Jones, One-dimensional transport and the quantisation of the ballistic resistance, J. Phys. C 21 (1988), L209–L214.
- [38] R. Landauer, Conductance from transmission: common sense points, Phys. Scr. **T42** (1992), 110.
- [39] S. Datta, *Electrical resistance : an atomistic view*, Nanotechnology **15** (2004), S433–S451.
- [40] A. Troisi and M.A. Ratner, Molecular signatures in the transport properties of molecular wire junctions: what makes a junction "molecular"?, Small 2 (2006), 172–181.
- [41] J.M. Seminario and P.A. Derosa, *Molecular gain in a thiotolane system*, J. Am. Chem. Soc. **123** (2001), 12418–12419.
- [42] H. Fink, N.J. Long, A.J. Martin, G. Opromolla, A.J. P. White, D.J. Williams, and P. Zanello, Ethynylferrocene compounds of 1,3,5tribromobenzene, Organometallics 16 (1997), 2646–2650.

[43] L. Patrone, S. Palacin, J. Charlier, F. Armand, J. P. Bourgoin, H. Tang, and S. Gauthier, Evidence of the key role of metal-molecule bonding in metal-molecule-metal transport experiments, Phys. Rev. Lett. 91 (2003), 096802.

- [44] P. Morf, F. Raimondi, H.G. Nothofer, B. Schnyder, A. Yasuda, J. M. Wessels, and T. A. Jung, *Dithiocarbamates: functional and versatile linkers for the formation of self-assembled monolayers*, Langmuir **22** (2006), 658–663.
- [45] A. Bezryadin, C. Dekker, and G. Schmid, Electrostatic trapping of single conducting nanoparticles between nanoelectrodes, Appl. Phys. Lett. 71 (1997), 1273–1275.
- [46] Y.V. Kervennic, H.S.J. Van der Zant, A.F. Morpurgo, L. Gurevich, and L.P. Kouwenhoven, *Nanometer-spaced electrodes with calibrated* separation, Appl. Phys. Lett. 80 (2002), 321–323.
- [47] L. Wang, W. Chen, C. Huang, Z.-K. Chen, and A.T.S. Wee, *Ultrafast electron transfer from oligo(p-phenylene-ethynylene)thiol to gold*, J. Phys. Chem. B **110** (2006), 674–676.
- [48] J. Chen, L.C. Calvet, M.A. Reed, D.W. Carrand D.S. Grubisha, and D.W. Bennett, *Electronic transport through metal1,4-phenylene* diisocyanidemetal junctions, Chem. Phys. Lett. 313 (1999), 741– 748.
- [49] N.D. Lang and C.R. Kagan, The role of chemical contacts in molecular conductance, Nano Lett. 6 (2006), 2955–2958.
- [50] J.M. Seminario, C.E. De La Cruz, and P.A. Derosa, A theoretical analysis of metal-molecule contacts, J. Am. Chem. Soc. 123 (2001), 5616–5617.
- [51] Y. Xue and M.A. Ratner, End group effect on electrical transport through individual molecules: A microscopic study, Phys. Rev. B **69** (2004), 085403.
- [52] Z. Ning, J. Chen, S. Hou, J. Zhang, Z. Liang, J. Zhang, and R. Han, First-principles calculation of the properties of molecular wires between Au clusters under equilibrium, Phys. Rev. B 72 (2005), 155403.

[53] S.N. Yaliraki and M.A. Ratner, Molecule-interface coupling effects on electronic transport in molecular wires, J. Chem. Phys. 109 (1998), 5036–5043.

- [54] E.G. Emberly and G. Kirczenow, Landauer theory, inelastic scattering, and electron transport in molecular wires, Phys. Rev. B 61 (2000), 5740–5750.
- [55] H. Günzler and H.U. Gremlich, IR spectroscopy, Wiley-VCH, 2002.
- [56] P.R. Griffiths and J.A. de Haseth, Fourier transform infrared spectroscopy, John Wiley & Sons, 1986.
- [57] H.U. Gremlich, IR spectroscopy, Wiley-VCH, 2002.
- [58] C. Cohen-Tannoudji, B. Diu, and F. Laloë, *Mécanique quantique*, Hermann, 1996.
- [59] H. Hövel and I. Barke, Large noble metal clusters: electron confinement and band structure effects, New J. Phys. 5 (2003), 31.1–14.
- [60] N.W. Ashcroft and I. Mermin, Solid state physics, Brooks/Cole, 1976.
- [61] G. Schmid and L.F. Chi, Metal clusters and colloids, Adv. Mater. 10 (1998), 515–526.
- [62] U. Kreibig and M. Vollmer, Optical properties of metal clusters, Springer, 1993.
- [63] G. Mie, Beiträge zur optik trüber medien, speziell kolloidaler metallösungen, Ann. Phys. 25 (1908), 377–445.
- [64] C. F. Bohren and D. R. Huffman, Absorption and scattering of light by small particles, John Wiley & Sons, 1993.
- [65] L. Genzel and T.P. Martin, Infrared absorption in small ionic crystals, Phys. Stat. Sol. 51 (1972), 91–99.
- [66] U. Kreibig and P. Zacharias, Surface plasma resonances in small spherical silver and gold particles, Z. Physik **231** (1970), 128.
- [67] David R. Lide (ed.), Handbook of chemistry and physics 85<sup>th</sup> edition, CRC Press, 2004-2005.

[68] M. Quinten, Optical constants of gold and silver clusters in the spectral range between 1.5 ev and 4.5 ev, Z.Phys. B 101 (1996), 211– 217.

- [69] G. Schmid and U. Simon, Gold nanoparticles: assembly and electrical properties in 13 dimensions, Chem. Comm. (2005), 697–710.
- [70] A. Bezryadin, R.M. Westervelt, and M. Tinkham, Self-assembled chains of graphitized carbon nanoparticles, Appl. Phys. Lett. 74 (1999), 2699–2701.
- [71] T. Sawitowski, Y. Miquel, A. Heilmann, and G. Schmid, Optical properties of quasi one-dimensional chains of gold nanoparticles, Adv. Funct. Mater. 11 (2001), 435–440.
- [72] S.A. Maier, M.L. Brongersma, P.G. Kik, and H. A. Atwater, Observation of near-field coupling in metal nanoparticle chains using far-field polarization spectroscopy, Phys. Rev. B 65 (2002), 193408.
- [73] C. Petit, V. Russier, and M. P. Pileni, Effect of the structure of cobalt nanocrystal organization on the collective magnetic properties, J. Phys. Chem. B 107 (2003), 10333–10336.
- [74] S.A. Maier, M. L. Brongersma, P.G. Kik, S. Meltzer, A.A.G. Requicha, and H.A. Atwater, *Plasmonics route to nanoscale optical devices*, Adv. Mater. 13 (2001), 1501–1505.
- [75] Z. Tang and N.A. Kotov, One-dimensional assemblies of nano-particles: preparation, properties and promise, Adv. Mater. 17 (2005), 951–962.
- [76] J.Y. Chang, J.J. Chang, B. Lo, S.H. Tzing, and Y.C. Ling, Silver nanoparticles spontaneous organize into nanowires and nanobanners in supercritical water, Chem. Phys. Lett. **379** (2003), 261.
- [77] J.H. Liao, K.J. Chen, L.N. Xu, C.W. Ge, J. Wang, L. Huang, and N. Gu, Self-assembly of length-tunable gold nanoparticle chains in organic solvents, Appl. Phys. A 76 (2003), 541–543.
- [78] K.D. Hermanson, S.O. Lumsdon, J.P. Williams, E.W. Kaler, and O.D. Veley, *Dielectrophoretic assembly of electrically functional mi*crowires from nanoparticle suspensions, Science 294 (2001), 1081– 1086.

[79] M. Burghard, G. Philipp, S. Roth, and K. von Klitzing, Bridging of lateral nanoelectrodes with a metal particle chain, Appl. Phys. A 67 (1998), 591–593.

- [80] G. Wang and R.W. Murray, Controlled assembly of monolayerprotected gold clusters by dissolved DNA, Nano Lett. 4 (2004), 95– 101.
- [81] K.M. Chen, X. Jiang, L.C. Kimerling, and P.T. Hammond, Selective self-organization of colloids on patterned polyelectrolyte templates, Langmuir 16 (2000), 7825–7834.
- [82] L. Bernard, M. Calame, S.J. van der Molen, J. Liao, and Ch. Schönenberger, Controlled formation of metallic nanowires via au nanoparticle ac trapping, submitted (2007).
- [83] H.A. Pohl, *Dielectrophoresis*, Cambridge University Press, 1978.
- [84] T.B. Jones, *Electromechanics of particles*, Cambridge University Press, 1995.
- [85] H. Morgan and N.G.Green, *AC electrokintetics*, Research Studies Press, 2003.
- [86] M. Washizu, S. Suzuki, O. Kurosawa, T. Nishizaka, and T. Shinoara, Molecular dielectrophoresis of biopolymers, IEEE Trans. Ind. Appl. 30 (1994), no. 4, 835–843.
- [87] F. Dewarrat, M. Calame, and C. Schönenberger, Orientation and positioning of DNA molecules with an electric field technique, Single Mol. 3 (2002), 189–193.
- [88] R. Pethig and G.H. Markx, Applications of dielectrophoresis in biotechnology, Trends in Biotech. 15 (1997), no. 10, 426–432.
- [89] Y.J. Yuan, M.K. Andrews, and B.K. Marlow, Chaining and dendrite formation of gold particles, Appl. Phys. Lett. 85 (2004), 130– 132.
- [90] R. Kretschmer and W. Fritzsche, Pearl chain formation of nanoparticles in microelectrode gaps by dielectrophoresis, Langmuir 20 (2004), 11797–11801.

[91] S. O. Lumsdon and D. M. Scott, Assembly of colloidal particles into microwires using an alternating electric field, Langmuir 21 (2005), 4874–4880.

- [92] M.S.M Saifullah, T. Ondarçuhu, D.K. Koltsov, C. Joachim, and M.E. Welland, A reliable scheme for fabricating sub-5 nm coplanar junctions for single-molecule electronics, Nanotechnology 13 (2002), 659–662.
- [93] H. Park, A.K.L. Kim, A.P. Alivisatos, J. Park, and P. McEuen, Fabrication of metallic electrodes with nanometer separation by electromigration, Appl. Phys. Lett. 75 (1999), 301–303.
- [94] A.F. Morpurgo, C.M. Marcus, and D.B. Robinson, Controlled fabrication of metallic electrodes with atomic separation, Appl. Phys. Lett. 74 (1999), 2084–2086.
- [95] M.F. Lambert, M.F. Goffman, J.P. Bourgoin, and P. Hesto, Fabrication and characterization of sub-3 nm gaps for single-cluster and single-molecule experiments, Nanotechnology 14 (2003), 772–777.
- [96] P. Steinmann and J. M. R. Weaver, Nanometer-scale gaps between metallic electrodes fabricated using a statistical alignment technique, Appl. Phys. Lett. 86 (2005), 063104.
- [97] S. Liu, J.B.H. Tok, and Z. Bao, Nanowire lithography: fabricating controllable electrode gaps using Au-Ag-Au nanowires, Nano Lett. 5 (2005), 1071–1076.
- [98] M. Trau, D.A.Saville, and I.A. Aksay, Assembly of colloidal crystals at electrode interfaces, Langmuir 13 (1997), 6375–6381.
- [99] K.P. Rodbell, A.J. Castellano, and R.I Kaufman, *AC electromi-gration (10MHz-1MHz) in Al metallization*, AIP Conf. Proc. **418** (1998), 212–223.
- [100] M.L. Trouwborst, S.J. van der Molen, and B.J. van Wees, *The role of Joule heating in the formation of nanogaps by electromigration*, J. Appl. Phys. **99** (2006), no. 11, 114316 1–7.
- [101] T.T. Tsong, Effects of electric field in atomic manipulations, Phys. Rev. B 44 (1991), 13703–13710.

[102] J. Méndez, J. Gómez-Herrero, J.I. Pascual, J.J. Sáenz, J.M. Soler, and A.M. Baró, Diffusion of atoms on Au(111) by the electric field gradient in scanning tunneling microscopy, J. Vac. Sci. Technol. B 14 (1996), 1145–1148.

- [103] H.S.J. van der Zant, Y.-V. Kervennic, M. Poot, K. ONeill, Z. de Groot, J. M. Thijssen, H. B. Heersche, N. Stuhr-Hansen, T. Bjrnholm, D. Vanmaekelbergh, C. A. van Walreed, and L. W. Jenneskensd, *Molecular three-terminal devices: fabrication and measurements*, Faraday Discuss. 131 (2006), 347–356.
- [104] L.H. Yu and D. Natelson, Density of states and magnetoconductance of disordered Au point contacts, Phys. Rev. B 68 (2003), 113407.
- [105] R.J.P. Keijsers, O.I. Shklyarevskii, and H. van Kempen, Spectroscopic study of the tunnel-current reduction due to adsorbed helium, Phys. Rev. B 61 (2000), 7328–7331.
- [106] J.G. Simmons, Electric tunnel effect between dissimilar electrodes separated by a thin insulating film, J. Appl. Phys. 34 (1963), 2581– 2590.
- [107] I. Grigoriev and E. Meilikhov (eds.), Handbook of physical quantities, CRC Press, 1997.
- [108] O.Y. Kolesnychenko, O. I. Shklyarevskii, and H. van Kempen, Giant influence of adsorbed helium on field emission resonance measurements, Phys. Rev. Lett. 83 (1999), 2242–2245.
- [109] H. Graf, J. Vancea, and H. Hoffmann, Single-electron tunneling at room temperature in cobalt nanoparticles, Appl. Phys. Lett. 80 (2002), 1264–1266.
- [110] C. Dietrich, B. Koslowski, F. Weigl, and P. Ziemann, Preparation of arrays of metallic nanoparticles exhibiting Coulomb blockade at room temperature: an approach based on the self-organization of metal-loaded diblock-copolymers, Surf. Interface Anal. 38 (2006), 1034–1038.
- [111] S. Datta, D.B. Janes, R.P. Andres, C.P. Kubiak, and R.G. Reifenberger, *Molecular ribbons*, Semicond. Sci. Technol. 13 (1998), 1347–1353.

[112] Z.L. Wang, Structural analysis of self-assembling nanocrystal superlattices, Adv. Mater. 10 (1998), 13–30.

- [113] G. Markovich, D.V. Leff, S.-W. Chung, H.M. Soyez, B. Dunn, and J.R. Heath, Parallel fabrication and single-electron charging of devices based on ordered, two-dimensional phases of organically functionalized metal nanocrystals, Appl. Phys. Lett. 70 (1997), 3107– 3109.
- [114] J.J. Shiang, J.R. Heath, C.P. Collier, and R.J. Saykally, Cooperative phenomena in artificial solids made from silver quantum dots: the importance of classical coupling, J. Phys. Chem. B **102** (1998), 3425–3430.
- [115] S. Sun and C.B. Murray, Synthesis of monodisperse cobalt nanocrystals and their assembly into magnetic superlattices, J. Appl. Phys. 85 (1999), 4325–4330.
- [116] M.P. Pileni, Nanocrystal self-assemblies: fabrication and collective properties, J. Phys. Chem. B 105 (2001), 3358–3371.
- [117] D. P. Long, C. H. Patterson, M. H. Moore, D. S. Seferos, G. C. Bazan, and J. G. Kushmerick, Magnetic directed assembly of molecular junctions, Appl. Phys. Lett. 86 (2005), 153105.
- [118] A. van Blaaderen, Colloids under external control, MRS bulletin (2004), 85–90.
- [119] J. Liao, L. Bernard, M. Calame, and C. Schönenberger, Reversible formation of molecular junctions in twodimensional nanoparticle arrays, Adv. Mater. 18 (2006), 2444–2447.
- [120] G.M. Whitesides and B. Grzybowski, Self-assembly at all scales, Science 295 (2002), 2418–2421.
- [121] V. Santhanam and R.P. Andres, Microcontact printing of uniform nanoparticle arrays, Nano Lett. 4 (2004), 41–44.
- [122] M.J. Hostetler, A.C. Templeton, and R.W. Murray, *Dynamics of place-exchange reactions on monolayerprotected gold clusters molecules*, Langmuir **15** (1999), 3782–3789.

[123] V. Santhanam, J. Liu, R. Agarwal, and R.P. Andres, Self-assembly of uniform monolayer arrays of nanoparticles, Langmuir 19 (2003), 7881–7887.

- [124] S. Huang, G. Tsutsui, H. Sakaue, S. Shingubara, and T. Takahagi, Formation of a large-scale LangmuirBlodgett monolayer of alkanethiol-encapsulated gold particles, J. Vac. Sci. Technol. B 19 (2001), 115–120.
- [125] L.J. Guo, Nanoimprint lithography: Methods and material requirements, Adv. Mater. 19 (2007), 495–513.
- [126] R.G. Nuzzo and D.L. Allara, Adsorption of bifunctional organic disulfides on gold surfaces, J. Am. Chem. Soc. 105 (1983), 4481– 4483.
- [127] M. Giersig and P. Mulvaney, Preparation of ordered colloid monolayers by electrophoretic deposition, Langmuir 9 (1993), 3408–3413.
- [128] A. Ulman, Formation and structure of self-assembled monolayers, Chem. Rev. 96 (1996), 1533–1554.
- [129] W.D. Luedtke and U. Landman, Structure, dynamics, and thermodynamics of passivated gold nanocrystallites and their assemblies, J. Phys. Chem. **100** (1996), 13323–13329.
- [130] A.C. Templeton, W. P. Wuelfing, and R.W. Murray, *Monolayer-protected cluster molecules*, Acc. Chem. Res. **33** (2000), 27–36.
- [131] J.R. Heath, C.M. Knobler, and D.V. Leff, Pressure/temperature phase diagrams and superlattices of organically functionalized metal nanocrystal monolayers: the influence of particle size, size distribution, and surface passivant, J. Phys. Chem. B 101 (1997), 189–197.
- [132] X.M. Lin, H.M. Jaeger, C.M. Sorensen, and K.J. Klabunde, Formation of long-range-ordered nanocrystal superlattices on silicon nitride substrates, J. Phys. Chem. B 105 (2001), 3353–3357.
- [133] S. Chen, Langmuir-Blodgett fabrication of two-dimensional robust cross-linked nanoparticle assemblies, Langmuir 17 (2001), 2878–2884.

[134] R.H. Terrill, T.A. Postlethwaite, C. Chen, C.D. Poon, A. Terzis, A. Chen, J.E. Hutchison, M.R. Clark, G. Wignall, J.D. Londono, R. Superfine and M. Falvo, C.S. Johnson, E.T. Samulski, and R.W. Murray, Monolayers in three dimensions: NMR, SAXS, thermal and electron hopping studes of alkanethiol stabilised gold clusters, J. Am. Chem. Soc. 117 (1995), 12537–12548.

- [135] T.P. Bigioni, X.-M. Lin, T. T. Nuyen, E.I. Corwin, T.A. Witten, and H.M. Jaeger, Kinetically driven self assembly of highly ordered nanoparticle monolayers, Nature Mater. 5 (2006), 265–270.
- [136] B.M. Quinn, I. Prieto, S.K. Haram, and A.J. Bard, Electrochemical observation of a metal/insulator transition by scanning electrochemical microscopy, J. Phys. Chem. B **105** (2001), no. 31, 7474–7476.
- [137] T. Ung, L.M. Liz-Marzán, and P. Mulvaney, Gold nanoparticle thin films, Colloids Surf. A, Physicochem. Eng. Aspects 202 (2002), 119– 126.
- [138] Z. L. Wang, Transmission electron microscopy of shape-controlled nanocrystals and their assemblies, J. Phys. Chem. B 104 (2000), 1153–1175.
- [139] M.J. Hostetler, S.J. Green, J.J. Stokes, and R.W. Murray, Monolayers in three dimensions: Synthesis and electrochemistry of  $\omega$ -functionalised alkanethiolate-stabilised gold cluster compounds, J. Am. Chem. Soc. **118** (1996), 4212–4213.
- [140] C. Weeraman, A.K. Yatawara, A. N. Bordenyuk, and A.V. Benderskii, Effect of nanoscale geometry on molecular conformation: vibrational sum-frequency generation of alkanethiols on gold nanoparticles, J. Am. Chem. Soc. 128 (2006), 14244–14245.
- [141] C.E.D. Chidsey, C.R. Bertozzi, T.M. Putvinski, and A.M. Mujsce, Coadsorption of ferrocene-terminated and unsubstituted alkanethiols on gold: Electroactive self-assembled monolayers, J. Am. Chem. Soc. 112 (1990), 4301–4306.
- [142] A. Kassam, G. Bremner, B. Clark, G. Ulibarri, and R. B. Lennox, Place exchange reactions of alkyl thiols on gold nanoparticles, J. Am. Chem. Soc. 128 (2006), 3476–3477.

[143] A.K. Boal and V.M. Rotello, Fabrication and self-optimization of multivalent receptors on nanoparticle scaffolds, J. Am. Chem. Soc. 122 (2000), 734–735.

- [144] Y. Song and R.W. Murray, Dynamics and extent of ligand exchange depend on electrical charge of metal nanoparticles, J. Am. Chem. Soc. 124 (2002), 7096–7102.
- [145] R. Hong, J.M. Fernández, H. Nakade, R. Arvizo, T. Emrick, and V.M. Rotello, In situ observation of place exchange reactions of gold nanoparticles. correlation of monolayer structure and stability, Chem. Comm. (2006), 2347–2349.
- [146] J.G. Kushmerick, D.B. Holt, S.K. Pollack, M.A. Ratner, J.C. Yang, T.L. Schull, J. Naciri, Martin .H. Moore, and R. Shashidhar, Effect of bond-length alternation in molecular wires, J. Am. Chem. Soc. 124 (2002), 10654–10655.
- [147] A.M. Rawlett, T.J. Hopson, L.A. Nagahara, and R.K. Tsui, Electrical measurements of a dithiolated electronic molecule via conducting atomic force microscopy, Appl. Phys. Lett. 81 (2002), 3043–3045.
- [148] A.S. Blum, J.C. Yang, R. Shashidhar, and B. Ratna, Comparing the conductivity of molecular wires with the scanning tunneling microscope, Appl. Phys. Lett. 82 (2003), 3322–3324.
- [149] L.T. Cai, H. Skulason, J.G. Kushmerick, S.K. Pollack, J. Naciri, R. Shashidhar, D.L. Allara, T.E. Mallouk, and T.S. Mayer, Nanowire-based molecular monolayer junctions: synthesis, assembly, and electrical characterization, J. Phys. Chem. B 108 (2004), 2827–2832.
- [150] S.K. Pollack, J. Naciri, J. Mastrangelo, C.H. Patterson, J. Torres, M. Moore, R. Shashidhar, and J.G. Kushmerick, Sequential deprotection for control of orientation in the self-assembly of asymmetric molecules for molecular electronic devices, Langmuir 20 (2004), 1838–1842.
- [151] X. Xiao, L.A. Nagahara, A.M. Rawlett, and N.J. Tao, Electrochemical gate-controlled conductance of single oligo (phenylene ethynylene)s, J. Am. Chem. Soc. 127 (2005), 9235–9240.

[152] J. Liao, S.J. van der Molen, L. Bernard, C. Schönenberger, and M. Calame, *Exchange and percolation in 2d-nanoparticle arrays with single molecular junctions*, in preparation (2007).

- [153] S. Kirkpatrick, Percolation and conduction, Rev. Mod. Phys. 45 (1973), 574–588.
- [154] J.M. Wessels, H.-G. Nothofer, W.E. Ford, F. von Wrochem, F. Scholz, T. Vossmeyer, A. Schroedter, H. Weller, and A. Yasuda, Optical and electrical properties of three-dimensional interlinked gold nanoparticle assemblies, J. Am. Chem. Soc. 126 (2004), 3349–3356.
- [155] D.B. Janes, V.R. Kolagunta, R.G. Osifchin, J.D. Bielefeld, R.P. Andres, J.I. Henderson, and C.P. Kubiak, *Electronic conduction through 2D arrays of nanometer diameter metal clusters*, Superlattices Microstruct. 18 (1995), no. 4, 275–282.
- [156] J.F. Sampaio, DC transport in self-assembled 2D layers of Ag nanoparticles, J. Phys. Chem. B 105 (2001), 8797–8800.
- [157] R. Huber, Ph.D. thesis, Universität Basel.
- [158] M. Magoga and C. Joachim, Conductance of molecular wires connected or bonded in parallel, Phys. Rev. B 59 (1999), 16011–16021.
- [159] C.C. Kaun and H. Guo, Resistance of alkanethiol molecular wires, Nano Lett. 3 (2003), 1521–1525.
- [160] D. J. Wold, R. Haag, M.A. Rampi, and C.D. Frisbie, Distance dependence of electron tunneling through self-assembled monolayers measured by conducting probe atomic force microscopy: unsaturated versus saturated molecular junctions, J. Phys. Chem. B 106 (2002), 2813–2816.
- [161] A. Salomon, D. Cahen, S. Lindsay, J. Tomfohr, V.B. Engelkes, and C.D. Frisbie, Comparison of electronic transport measurements on organic molecules, Adv. Mater. 15 (2003), 1881–1890.
- [162] T. Lee, W. Wang, J. F. Klemic, J.J. Zhang, J. Su, and M.A. Reed, Comparison of electronic transport characterization methods for alkanethiol self-assembled monolayers, J. Phys. Chem. B 108 (2004), 8742–8750.

[163] W. Wang, T. Lee, and M. A. Reed, Electronic transport in molecular self-assembled monolayer devices, Proc. IEEE 93 (2005), 1815–1824.

- [164] T. Hassenkam, K. Moth-Poulsen, N. Stuhr-Hansen, K. Nørgaard, M.S. Kabir, and T. Bjørnholm, Self-assembly and conductive properties of molecularly linked gold nanowires, Nano Lett. 4 (2004), 19–22.
- [165] D.S. Seferos, S.A. Trammell, G.C. Bazan, and J.G. Kushmerick, Probing  $\pi$ -coupling in molecular junctions, Proceedings of the National Academy of Sciences of the United States of America **102** (2005), 8821–8825.
- [166] D.S. Seferos, A.S. Blum, J.G. Kushmerick, and G.C. Bazan, Single-molecule charge-transport measurements that reveal technique-dependent perturbations, J. Am. Chem. Soc. 128 (2006), 11260–11267.
- [167] M. Paulsson, T. Frederiksen, and M. Brandbyge, *Inelastic transport through molecules : comparing first-principles calculations to experiments*, Nano Lett. **6** (2006), 258–262.
- [168] J.M. Seminario, A.G. Zacarias, and J.M. Tour, Theoretical interpretation of conductivity measurements of a thiotolane sandwich. a molecular scale electronic controller, J. Am. Chem. Soc. 120 (1998), 3970–3974.
- [169] J.M. Seminario, P.A. Derosa, and J.L. Bastos, *Theoretical inter*pretation of switching in experiments with single molecules, J. Am. Chem. Soc. **124** (2002), 10266–10267.
- [170] J.M. Seminario, A.G. Zacarias, and J. M. Tour, *Theoretical study of a molecular resonant tunneling diode*, J. Am. Chem. Soc. **122** (2000), 3015–3020.
- [171] D. Roy and J. Fendler, Reflection and absorption techiques for optical characterization of chemically assembled nanomaterials, Adv. Mater. 16 (2004), 479–508.
- [172] R.H. Doremus, Optical properties of small gold particles, J. Chem. Phys. 40 (1964), 2389–2396.

[173] C.G. Granqvist and O. Hunderi, *Optical properties of gold particles*, Phys. Rev. B **16** (1977), 3513–3534.

- [174] L.B. Scaffardi, N. Pellegri, O. de Sanctis, and J.O. Tocho, Sizing gold nanoparticles by optical extinction spectroscopy, Nanotechnology 16 (2005), 158–163.
- [175] J. Wang, W.M. Lau, and Q. Li, Effects of particle size and spacing on the optical properties of gold nanocrystals in alumina, J. Appl. Phys. 97 (2005), 114303.
- [176] C. Wang, Z. Ma, and Z. Su, Synthesis and self-assembly of silica-coated anisotropic gold nanoparticle films, Nanotechnology 17 (2006), 1819–1824.
- [177] P. Mulvaney, Surface plasmon spectroscopy of nanosized metal particles, Langmuir 12 (1996), 788–800.
- [178] J. Schmitt, P. Mächtle, D. Eck, H. Möhwald, and C.A. Helm, Preparation and optical properties of colloidal gold monolayers, Langmuir 15 (1999), 3256–3266.
- [179] J. Israelachvili, *Intermolecular and surface forces*, Academic Press: New York, 1985.
- [180] S. Schelm, G.B. Smith, G. Wei, A. Vella, L. Wieczorek, K.-H. Müller, and B. Raguse, Double effective medium model for the optical properties of self-assembled gold nanoparticle films cross-linked with alkane dithiols, Nano Lett. 4 (2004), 335–339.
- [181] J.C. Maxwell Garnett, Colours in metal glasses and in metallic films, Philos. Trans. R. Soc. London 203 (1904), 385.
- [182] J.J. Stapleton, P. Harder, T.A. Daniel, M.D. Reinard, Y. Yao, D.W. Price, J.M. Tour, and D.L. Allara, Self-assembled oligo(phenylene-ethynylene) molecular electronic switch monolayers on gold: structures and chemical stability, Langmuir 2003 (2003), 8245–8255.
- [183] M. Tammer and A.P. Monkman, Measurement of the anisotropic refractive indices of spin cast thin poly(2-methoxy-5-(2'-ethyl-hexyloxy)-p-phenylenevinylene) (MEH-PPV) films, Adv. Mater. 14 (2002), 210.

[184] L.J. Bellamy, The infra-red spectra of complex molecules, L.J. Bellamy, 1975.

- [185] M.J. Frisch, G.W. Trucks, H.B. Schlegel, G.E. Scuseria, M.A. Robb, J.R. Cheeseman, J.A. Montgomery, T. Vreven, K.N. Kudin, J.C. Burant, J.M. Millam, S.S. Iyengar, J. Tomasi, V. Barone, B. Mennucci, M. Cossi, G. Scalmani, N. Rega, G.A. Petersson, H. Nakatsuji, M. Hada, M. Ehara, K. Toyota, R. Fukuda, J. Hasegawa, M. Ishida, T. Nakajima, Y. Honda, O. Kitao, H. Nakai, M. Klene, X. Li, J.E. Knox, H.P. Hratchian, J.B. Cross, V. Bakken, C. Adamo, J. Jaramillo, R. Gomperts, R.E. Stratmann, O. Yazyev, A.J. Austin, R. Cammi, C. Pomelli, J.W. Ochterski, P.Y. Ayala, K. Morokuma, G.A. Voth, P. Salvador, J.J. Dannenberg, V.G. Zakrzewski, S. Dapprich, A.D. Daniels, M.C. Strain, O. Farkas, D.K. Malick, A.D. Rabuck, K. Raghavachari, J.B. Foresman, J.V. Ortiz, Q. Cui, A.G. Baboul, S. Clifford, J. Cioslowski, B.B. Stefanov, G. Liu, A. Liashenko, P. Piskorz, I. Komaromi, R.L. Martin, D.J. Fox, T. Keith, M.A. Al-Laham, C.Y. Peng, A. Nanayakkara, M. Challacombe, P.M.W. Gill, B. Johnson, W. Chen, M.W. Wong, C. Gonzalez, and J.A. Pople, Gaussian 03, revision c.02, Tech. report, Gaussian Inc., Wallingford, CT, 2004.
- [186] A.P. Scott and L. Radom, Harmonic vibrational frequencies: an evaluation of Hartree-fock, Möller-Plesset, quadratic configuration interaction, density functional theory, and semiempirical scale factors, J. Phys. Chem. 100 (1996), 16502–16513.
- [187] K. Edinger, A. Gölzhäuser, K. Demota, Ch. Wöll, and M. Grunze, Formation of self-assembled monolayers of n-alkanethiols on gold: A scanning tunneling microscopy study on the modification of substrate morphology, Langmuir 9 (1993), 4–8.
- [188] C. Schönenberger, J.A.M. Sondag-Huethorst, J. Jorritsma, and L.G.J. Fokkink, What are the "hole" in self-assembled monolayers of alkanethiols on gold?, Langmuir 10 (1994), 611–614.
- [189] G.E. Poirier, Mechanism of formation of Au vacancy islands in alkanethiol monolayers on Au(111), Langmuir 13 (1997), 2019–2026.
- [190] R.G. Snyder, M. Maroncelli, H.L. Strauss, and V.M. Hallmark,

- Temperature and phase behavior of infrared intensities: the poly(methylene) chain, J. Phys. Chem. **90** (1986), 5623–5630.
- [191] M.J. Hostetler, J.E. Wingate, C.-J. Zhong, J.E. Harris, R.W. Vachet, M.R. Clark, J.D. Londono, S.J. Green, J.J. Stokes, G.D. Wignall, G.L. Glish, M.D. Porter, N.D. Evans, and R.W. Murray, Alkanethiolate gold cluster molecules with core diameters from 1.5 to 5.2 nm: core and monolayer properties as a function of core size, Langmuir 14 (1998), 17–30.
- [192] J.F. Moulder, W.F. Stickle, P.E. Sobol, and K.D. Bomben, *Hand-book of X-ray photoelectron spectroscopy*, Perkin-Elmer, 1992.
- [193] L. Bernard, Y. Kamdzhilov, S.J. van der Molen, M. Calame, J. Liao, and C. Schönenberger, Optical evidence for reversible formation of molecular junctions in 2d nanoparticle arrays, in preparation (2007).
- [194] K.W.Hipps, Its all about contacts, Science **294** (2001), 536–537.
- [195] W. Wang, T. Lee, and M. A. Reed, Mechanism of electron conduction in self-assembled alkanethiol monolayer devices, Phys. Rev. B 68 (2003), 035416.
- [196] M. Brust, M. Walker, D. Bethell, D.J. Schiffrin, and R. Why-man, Synthesis of thiol-derivatised gold nanoparticles in a two-phase liquid-liquid system, J. Chem. Soc., Chem. Commun. (1994), 801–802.
- [197] J. Turkevich, P.C. Stevenson, and J. Hillier, A study of the nucleation and growth processes in the synthesis of colloidal gold, Discuss. Faraday Soc. 11 (1951), 55–75.
- [198] J.W. Slot and H.J. Geuze, A new method for preparing gold probes for multiplelabeling cytochemistry, Eur. J. Cell Biol. 38 (1985), 87– 93.
- [199] J.L. Wilbur, A. Kumar, H.A. Biebuyck, E. Kim, and G.M. White-sides, *Microcontact printing of self-assembled monolayers: applications in microfabrication*, Nanotechnoloy **7** (1996), 452–457.
- [200] S. Hendy, S.A. Brown, and M. Hyslop, Coalescence of nanoscale metal clusters: molecular-dynamics study, Phys. Rev. B 68 (2003), 241403.



# **PUBLICATIONS**

## ARTICLES

- L. Bernard, A.N. Caruso, B. Xu, B. Doudin, P.A. Dowben, *The adsorption of orthocarborane on cobalt*, Thin Solid Films **428**, 253-256 (2003)
- A.N. Caruso, L. Bernard, B. Xu, P.A. Dowben, Comparison of adsorbed orthocarborane and metacarborane on metal surfaces, J. Phys. Chem. **107**, 9620-9623 (2003)
- L. Bernard, J. Monson, A. Sokolov, Z.Y. Liu, C.S. Yang, P.A. Dowben, B. Doudin, *Magnetoresistance in boron carbide junctions*, Appl. Phys. Lett. **83**, 3743-3745 (2003)
- L. Bernard, M. Calame, S.J. van der Molen, J. Liao and Ch. Schönenberger, Controlled formation of metallic nanowires via Au nanoparticle ac trapping, submitted
- J. Liao, L. Bernard, M. Langer, Ch. Schönenberger and M. Calame, Reversible formation of molecular junctions in two dimensional nanoparticle arrays, Adv. Mater. 18, 2444-2447 (2006)
- L. Bernard, Y. Kamdzhilov, S. J. van der Molen, M. Calame, J. Liao and C. Schönenberger, *Optical evidence for reversible formation of molecular junctions in 2D nanoparticle arrays*, in preparation
- J. Liao, Sense Jan van der Molen, L. Bernard, Ch. Schönenberger and M. Calame, Exchange and percolation in 2D-nanoparticle arrays with single molecular junctions, in preparation

## Oral Presentations

- Nanogaps: on the way to contact single molecules, NCCR Molecular Electronics Meeting, Zurzach (Switzerland), August 28, 2003
- Nanogaps and Colloids: on the way to contact single molecules, NCCR Molecular Electronics Meeting, Zürich (Switzerland), February 17, 2004
- Nanogaps and Colloids, NCCR Molecular Electronics Meeting, Basel (Switzerland), September 7, 2004
- Nanogaps and Colloids: for the electrical characterisation of molecules, Nano and Giga Challenges in Microelectronics, Cracow (Poland), September 13-17, 2004
- Molecular Electronics using colloids, SONS Meeting, Basel (Switzerland), November 12-13, 2004
- Working with nanoparticles, Mesoscopic Physics Seminar, Basel (Switzerland), November 29, 2004
- Application of nanoparticles in molecular electronics, Self-Organised Nanostructures Summer School, Cargese (France), July 17-23, 2005
- Optical Properties of Metal Clusters, Mesoscopic Physics Seminar, Basel (Switzerland), October 24, 2005
- Reversible networks of molecular junctions, NCCR Molecular Electronics Meeting, Basel (Switzerland), April 12, 2006
- Infrared spectroscopy, Mesoscopic Physics Seminar, Basel (Switzerland), May 15, 2006
- Two-dimensional networks of molecular junctions, From Solid States to Biophysics III, Cavtat (Croatia), June 26, 2006
- Reversible 2D networks of molecular junctions, ICN+T 2006, Basel (Switzerland), July 31, 2006
- Reversible Molecular Networking by Self-assembly, Invited talk, University of Bern (Switzerland), August 8, 2006
- Nanoparticle assemblies with a view to molecular electronics, Nanoelectronics Days 2006, Aachen (Germany), October 13, 2006

• Expanding the Horizon of Molecular Electronics via Nanoparticle Assemblies, Invited talk, University of Strasbourg (France), March 14, 2007

### POSTER PRESENTATIONS

- Growth of Boron Carbide on Cobalt from the Decomposition of Orthocarborane, E-MRS Spring Meeting, Symposium J, Strasbourg (France), June 18-21, 2002
- Break-junctions and nanogaps for molecular electronics, NCCR review panel, Basel (Switzerland), May 18-22, 2003
- Break-junctions and nanogaps for molecular electronics, 3rd SFB Workshop and Krupp Symposium, Konstanz (Germany), July 6-9, 2003
- Break-junctions and nanogaps for molecular electronics, 7th European Conference on Molecular Electronics ECME, Avignon (France), September 10-14, 2003
- Break-junctions and nanogaps for molecular electronics, Swiss/US Nanoforum, Basel (Switzerland), October 13-14, 2003
- Networks of molecular junctions, NCCR review panel, Gwatt (Switzerland), October 6-7, 2005
- Networks of molecular junctions, Swiss Physical Society (SPS) meeting, Lausanne (Switzerland), February 14-15, 2006



## CURRICULUM VITAE

#### **EDUCATION**

- 2006 **Ph.D. of Physics**, University of Basel, Switzerland. Thesis: Expanding the Horizon of Molecular Electronic via Nanoparticle Assemblies, Advisor: Prof. C. Schönenberger, Suma cum Laude.
- 2002 Master of Physics, carried out at University of NE-Lincoln, USA, awarded by EPFL, Switzerland. Thesis: Boron carbide barrier magnetic junctions and the buried Co/boron carbide interface, Advisors: Prof. B. Doudin and Prof. P. Dowben, best distinction.
- 2002 Bachelor of Physics and Engineering (Phys. Dipl. EPF), Federal Polytechnical School of Lausanne (EPFL), Switzerland. Thesis: Fabrication and study of Ni and multilayer Co-Cu nanowires and Study of thermoelectric effects in metallic nanowires under the influence of a magnetic field, Advisor: Prof. J.-P. Ansermet.
- 1996 **Degree of Mathematics and Sciences**, High School of Burier (CESSEV), Switzerland.

### RESEARCH EXPERIENCE

2003 – 2006 **Doctoral research**, Uni. Basel, Switzerland. Fabrication and study of the electrical transport properties of molecular nanojunctions within 1D- and 2D geometries. Developments on 1D and 2D assembly strategies, synthesis of nanoparticles, UV and electron-beam lithographies, imaging by SEM. Electrical transport measurements at low and room temperature, including the build-up of low temperature setup and Labview programming. Optical studies involving UV-vis, FTIR and X-ray spectroscopies.

2001 – 2002 Master research, UNL, USA. Fabrication and characterisation of spin-polarised electron transport in magnetic tunnel junctions. Fabrication of magnetic junctions, involving wafer processing, UV-lithography, metal sputtering and imaging by AFM. Interfaces study of the F/I/F junctions by XPS, UV-photoelectron spectroscopy (UPS), and angle-resolved inverse photoelectron spectroscopy (ARIPES). Electrical transport and magnetic measurement.

2000 – 2001 **Diploma research**, EPFL, Switzerland. Fabrication, simulation and study of heat and spin transport phenomena in metallic nanowires. Fabrication of magnetic nanowires (homogeneous, tri-layers and multi-layers) by metal electrodeposition in porous membranes. Magnetic characterisation at low temperature. Study of the thermoelectric effect and its influence on the magnetoresistance of the nanowires.

2000 Summer Student Program at the European Center for Nuclear Research, CERN, Switzerland. Thesis:

A new cryogenic beam tracker for the NA60 experiment.

Set-up and optimisation of temperature-controlled detector units based on the Lazarus Effect for the detection of dimuons. Study of dimuon production in heavy ion collisions.

Internship at the Institute of Applied Radiophysics, IRA Lausanne, Switzerland. Report: Evaluations dosimétriques en radiodianostic. Study of the impact on health of various radiologic diagnostics in Switzerland. Calculation of the radiation doses for each medical radiodiagnostic.

## TEACHING EXPERIENCE

2003 - 2006	General physics exercises teaching and practical classes for students from Physics and Nanosciences Sections.
2004 - 2005	Introduction and initiation to the lab techniques (UV and e-beam lithographies, evaporation, SEM observation, particle synthesis, basic transport measurements) of undergraduate students (3 weeks periods).
2002	Employment as "scientific collaborator" for a teaching program, physics department, EPFL: Realisation of a scientific file, accurately describing the experiments and demonstrations presented to the students during physics lectures, designed for students use, as well as professors use.
1999 - 2001	General physics and Optics exercises teaching for $1^{st}$ and $2^{nd}$ year EPFL students from Physics and Informatics Sections.
1993 - 2001	Diverse physics and mathematics private lessons for various educational levels (from school to $2^{nd}$ year university).

### Miscellaneous

- Referee at the conference "E-MRS", Strasbourg, France (2002)
- Chairlady at the conference "From Solid States to Biophysics III", Cavtat, Croatia (2006)
- Cited in the "News and Views" of NATURE 442, 994 (2006)
- Press releases : Neue Zürcher Zeitung, Basler Zeitung, Uni News, Chemische Rundschau (2006)



## ACKNOWLEDGMENTS

The discussions exposed in this dissertation are the fruit of a tremendous body of work, from the first concepts settlings to the technical realisations, characterisations and analyses. This involved a large number of competent persons, who gave me support in actively contributing to this work. Here, I would like to extend my warmest thanks to all these people.

Firstly, I address my sincere thanks to my thesis advisor, Prof. Christian Schönenberger for the unconditional trust he has placed in me. His contagious passion for physics, his great ideas, and the amazing technical working environment he provides in his labs were my driving forces.

Many thanks to the whole *Molecular Electronics* team, especially Lucia Grüter, who introduced me to all the fabrication techniques when I arrived, Michel Calame who guided me into the "wet world", Jianhui Liao, Teresa Gonzales, Zheng Ming Wu with her permanent good mood, Songmei Wu and Roman Huber. I have greatly benefited from the recent arrival of Sense Jan van der Molen, through his highly motivating support, his constant care and large knowledge. Thank you so much.

I would like to thank as well my friend and colleague Takis Kontos, for his interest and wise advice in this project, Peter Müschlegen and Javad Farahani for their involvement in the early optical study, Laurent Kreplak for the TEM imaging and particularly Peter Morf for the XPS measurements and analysis.

From the chemistry side, I am indebted to Prof. Marcel Mayor for providing me insights on organic chemistry and waking my interest throughout fruitful discussions. In particular, thank you for having given me help and assistance for simple chemical manipulations, whenever I needed some.

A specially warm thanks as well to my colleague and friend Yavor Kamdzhilov from the *Physikalische Chemie Department*, who gave me

a totally free access to his laboratory, helped my research in any circumstances throughout his wide knowledge on optical measurement techniques and his connections in the whole *Chemistry Department*. Thanks to Prof. H.J. Wirz who allowed such a fruitful collaboration.

Thanks to the synthetical chemists who provided me with the desired molecular wires: Michael Langer from Prof. A. Pfaltz's group (Anorganische Chemie Department) for the OPEs and Viviana Lorelei Horhoiu for the OPVs from Prof. M. Mayor's group (Organische Chemie Department). Thank you both as well for your comments and advices on synthesis and handling of organic molecules.

I am thankful to Prof. Marcel Mayor and Prof. Bernard Doudin for accepting to be referees for my PhD project.

I address a warm thanks to the four brave persons who read through the draft of this dissertation and improved it by numerous wise remarks, namely Timothey Ashworth, Michel Calame, Sense Jan van der Molen and Nicolas Pilet. Thank you for your great efforts on this final step.

Although staying behind the scenes, the staff of the electronics and mechanical workshops, as well as administrative persons provided me with efficient support. I am in particular grateful to Michael Steinacher (electronics workshop), Werner Roth (mechanical workshop) and Barbara Kammermann (secretary).

I would also like to mention the other current and former members of the *Mesoscopic Physics* group, for the warm and collegial atmosphere they provided in the daily life, in particular Sangeeta Sahoo with her unconditional friendship, Soufiane Ifadir, Dino Keller, Christian Hoffmann, Jürg Furer, Gunnar Gunnarsson, Matthias Gräber, Alex Eichler and Andreas Kleine, who all contribute to create a nice atmosphere within this rich cultural environment.

Thanks to my family, who, despite their completely different orientation, accepted and respected my choice of performing a PhD project. Thanks for the trust you placed in me.

With the warmth from my heart, I thank Nicolas for his love and his every day support through the sharing of this unique adventure. Just as we decided to begin physics study together ten years ago, we went on together with the project of making a PhD. Now, this project comes successfully to an end, and I ow it to you, fully.

This work has been financed by the Swiss National Science Foundation (SNF) and the National Centre of Competence in Research (NCCR). Financial support for the printing of this thesis was provided by the University of Basel and the Werenfels-Fonds der Freien Akademischen Gesellschaft (FAG).

